Spectroscopic study of transition metal compounds

Thesis

Presented to the Faculty of Physics

University of Osnabrück

by

Demeter Mihaela–Carmen

Thesis Advisor: apl. Prof. Dr. Manfred Neumann

January 30, 2001

Table of Contents

List of Figures

Introduction

In the last few years a renewed interest has reappeared in materials that were highly investigated in the $50s$–$70s$, like manganese perovskites, spinel chalcogenides and vanadium oxides.

The first two classes of materials are nowadays intensively studied due to the colossal magnetoresistance effect, which is the magnetoresistance associated with a ferromagnetic to paramagnetic transition [186, 79, 142].

Vanadium oxides are known to form many compounds, as V_2O_3, V_2O_5 and VO_2, VO, V_nO_{2n-1} (Magnéli phases) and $V_{2n}O_{5n-2}$ (Wadsley phases) and most of them undergo metal–to–insulator phase transitions (MIT), with a high increase in the electrical conductivity. For example, there is an abrupt conductivity increase of five orders of magnitude for VO_2 at 340 K and seven orders of magnitude for V_2O_3 at 160 K [123, 3, 23]. Many technological applications derive from the variation of the physical properties around the phase transition temperature. VO_2 appears to be a good candidate for the fabrication of many electrical and optical devices.

Although many efforts have been done in order to understand their electronic structures and to elucidate the MIT mechanisms, the vanadium oxides are still matter of debate in science.

This study has been performed in order to understand the electronic structure of these very intriguing materials. The role of the different dopants that induce strong changes in the electronic and magnetic properties has been investigated making use of two spectroscopic techniques, namely X–ray photoelectron and X–ray emission spectroscopy.

The work is structured as following:

⋆ Chapter 1 gives a description of the investigated transition metal compounds, their characteristics and some of the related actual topics.

⋆ In Chapter 2 a short presentation of the photoemission process, photoelectron spectral characteristics, experimental techniques and few theoretical approaches used to interpret the experimental data, is given.

⋆ In Chapters 3 and 4 a spectroscopic study of the CMR compounds: manganese perovskites, $La_{1-x}A_xMnO_3$ and Cr– spinels, $Fe_{1-x}Cu_xCr_2S_4$ ($x = 0.0; 0.5$) is presented. Their electronic structures and the role of the different dopants on the electronic structure and, implicitly, on the properties of the investigated systems, are studied.

In Chapter 3 several series of Mn–perovskites were studied: $La_{1-x}Sr_xMnO_3$, $La_{1-x}Ba_xMnO_3$, $La_{1-x}Ca_xMnO_3$ and $La_{1-x}Pb_xMnO_3$. New XPS results of the Sr–doped single crystals, $(La_{0.9}Sr_{0.1})_{0.9}MnO_3$, $La_{0.8}Sr_{0.2}MnO_3$ and $La_{0.7}Sr_{0.3}MnO_3$ are presented. They are interpreted making use of the available band structure calculations. We firstly perform an XPS investigation of the 'doubly'[1] doped manganites: $La_{0.76}Ba_{0.24}Mn_{0.86}Ni_{0.14}O_3$ and $La_{0.78}Ba_{0.22}Mn_{0.84}Co_{0.16}O_3$ – single crystals. The results are related to the magnetic study previously performed on the same samples [176].

A comprehensive study of the $Fe_{1-x}Cu_xCr_2S(Se)_4$ spinel system is then presented in Chapter 4. A special attention is paid to the $CuCr_2Se_4$ system, where the Cu valence is still a matter of controversy. Two models developed by Lotgering [106, 107] and Goodenough [62] suggest both monovalent and divalent character of the Cu ions. Several other crystals of Cr– spinel chalcogenides, $ACr_2S(Se)_4$ (A= Mn, Zn, Cd, Hg) are investigated by XPS. From a detailed study of the core level XPS spectra, the electronic configurations of the constituent ions are determined.

⋆ Chapter 5 deals with vanadium–oxides, mainly with mixed–valence systems: $V_{2-x}Mo_xO_5$ ($x = 0.1; 0.2; 0.4; 0.6; 0.8$), solid solutions and V_6O_{13}, V_4O_7, V_3O_5,

[1] 'doubly' doped manganites means that not only the rare–earth is partially substituted by an alkali–earth, but also the transition metal (Mn) by another transition metal ion.

single crystals. Some of them were investigated for the first time by XPS. The role of the Mo doping on the electronic structure of the widely used catalyst V_2O_5 is determined from a comparison between the XPS and XES data. The obtained results are in very good agreement with band structure calculations. For V_6O_{13}, V_4O_7 and V_3O_5, a spectroscopic investigation of the metal–insulator transition is performed.

$\star$ In Chapter 6 the electronic structure of the $Mg_{1-x}Cu_xO$ solid solutions ($x = 0.1; 0.15; 0.2$) is analyzed by X–ray photoelectron and X–ray emission spectroscopy. Due to the complementarity of the two methods, from a comparison between the XPS and XES results, the partial Cu $3d$ and O $2p$ states distribution in the valence band is determined. The XPS core level data provide us information about the degree of Cu $3d$–O $2p$ covalency.

$\star$ The conclusions and outlook of the present study are given in Chapter 7. At the end, a list containing the bibliographic references is presented.

Chapter 1

Why transition metal compounds?

Transition metal compounds exhibit a large variety of electronic and magnetic properties and, although they have been investigated over many decades, open questions related to their behaviour still exist. Only in the last few years a huge number of studies has been performed in order to understand their electronic structures and implicitly, to elucidate the origin of the related effects, as the metal–insulator transition and the colossal magnetoresistance.

The physics of the transition metal compounds is extremely rich. For the present purpose, few aspects associated with the vanadium, chromium and manganese systems will be reviewed.

As concerning vanadium oxides, many experimental and theoretical tools have been used to elucidate their interesting properties. Despite this huge effort, there is still an open question related to which extent the electron correlation effects play a role in determining their complicated behaviour. Besides the electron–electron interaction, the electron–phonon coupling appears to be an important key to explain the metal–insulator transition, which characterize most of the vanadium oxides.

A short description of some possible mechanisms of the metal–insulator transitions is presented below.

Metal–insulator transitions

Metal–insulator transitions are accompanied by huge changes in the electrical resistivity. In systems with weakly interacting electrons, one can classify metals and insulators on the basis of the band filling: if the highest band is partially or fully occupied, we talk about metals or insulators. In the first case, the Fermi level is situated inside a band, whereas for an insulator it lies in a band gap. In systems with strongly correlated electrons, this theory is not any more valid.

More than 60 years ago, it has been observed that there are systems with partially filled bands that, according to the above classification scheme, should be metals, but in fact they exhibit an insulating behaviour [39]. Mott explained this by electron–electron correlations [122]. The first theoretical description of the Mott transitions (transitions between a metal and a Mott insulator) was given in the Hubbard model [75, 5]. The electron correlation strength (U/t) and the band filling are two important parameters of this simple model that considers only the electrons in a single band. Depending on whether the transitions are controlled by the electron concentration (n) or by the ratio bandwidth/interaction, they can be classified as: (1) filling–control (FC) or (2) bandwidth–control (BC) transitions [76].

In case (1), the filling control can be realized:

– In ternary compounds, in which ions with different valences occupy ionic sites other than those related with the $3d$ and $2p$ electrons. A good example is the $La_{1-x}Sr_xMnO_3$ system, where the A–site of the perovskite structure (ABO_3) is occupied by La and Sr;

– In nonstoichiometric systems; for example, V_2O_{3-y} shows a transition for $y < 0.03$.

In case (2), several methods to control the one–electron bandwidth can be enumerated:

– By applying pressure; a typical system in which the pressure–induced Mott insulator to metal transition can occur is V_2O_3;

– By changing the chemical composition using the solid solution or mixed–crystal effect ($NiS_{2-x}Se_x$);

– By modifying the ionic radius of the A–site in perovkites (ABO_3). It is

known that, when the A–ionic radius varies, the tolerance factor also changes, according to eq. (1.1):

$$f = \frac{r_A + r_O}{\sqrt{2}(r_B + r_O)} \tag{1.1}$$

$f = 1$ corresponds to a cubic structure; when f decreases, the structure changes from cubic to rhombohedral and orthorhombic.

Among the transition–metal compounds, vanadium oxides are the ideal subjects for the investigation of the metallic and insulating states due to the large variety of electrical properties observed for similar materials. Over the last three decades intense experimental and theoretical investigations have been performed and some questions related to the MIT mechanisms could be completely or partially answered [123, 23, 76]. Several possible mechanisms responsible for the metal–insulator transitions observed in such materials were proposed since early $'70s$ [3]: the ordinary band overlap, crystalline symmetry changes, antiferromagnetism, electronic correlations (Mott transitions), electron–phonon interactions, etc. However, as concerning vanadium oxides, there is still controversy on many aspects, as: the surface characterization of the widely used catalyst V_2O_5, the phase transition nature in VO_2 and V_2O_3, as well as the influence of the antiferromagnetic ordering on the phase transition for V_2O_3.

V_2O_3 has been extensively studied as a canonical Mott–Hubbard system. The vanadium ions have a $3d^2$ configuration. Due to the trigonal distorsion of the lattice, the t_{2g} states are split into nondegenerate a_{1g} and doubly degenerate e_g levels. The vanadium–vanadium pairs, arranged along the c axis of the corundum structure, have a large overlap of the orbitals in the a_{1g} levels. Most of the existent theoretical models related to the electronic structure of V_2O_3 have considered one electron in a singlet bond a_{1g} level and the second in the doublet e_g levels.

Although the spectroscopic investigation of this system has suggested a typical Mott–Hubbard type electronic structure ($\Delta > U$) [157], the similar values of the charge–transfer and Coulomb electron–electron interactions energies, Δ and U[1], point out the strong hybridization between the V $3d$ and O $2p$ states [163].

[1] Δ and U are defined as shown in Fig. 1.1.

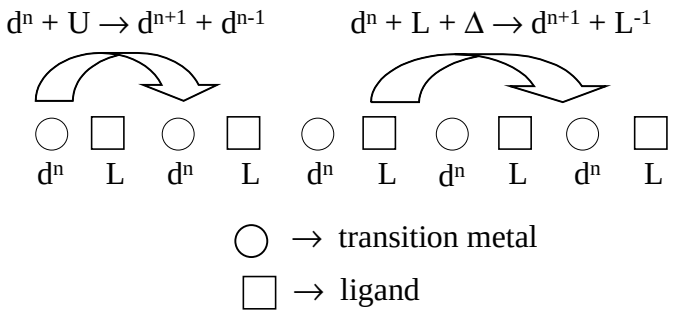

Figure 1.1: Simple sketch to define the Coulomb correlation and charge transfer energies (U, Δ) [71]

The spin–orbit coupling was proposed as an important factor to understand the ordered spin structure in the antiferromagnetic insulating phase of V_2O_3 [27]. More recently, the importance of the interaction between orbital and spin degrees of freedom to explain the first–order nature of the magnetic order transition was underlined by Rice *et al.* [143]. A new picture of the V_2O_3 electronic structure, different from the Mott–Hubbard description, in which two electrons occupy the e_g orbitals (S=1) was theoretically proposed and supported by absorption spectroscopy data [133]. It appears that even for the highly investigated V_2O_3 system, our present understanding is not exhaustive.

Moreover, subject of controversy are the less investigated mixed–valence vanadium oxides, as V_6O_{13}, V_4O_7, V_3O_5, etc. The amount of publications in this field is not so high and this is partially related to the difficulty in growing pure, stoichiometric single crystals.

Therefore, a spectroscopic study of the electronic structure of different vanadium oxides in both phases, metallic and insulating, appears to be appropriate.

Colossal magnetoresistance

The magnetoresistance (MR), the change in the electrical resistance of a conductor by an applied magnetic field (H), is defined by (1.2):

$$MR = -\frac{R(H) - R(0)}{R(0)} \tag{1.2}$$

In nonmagnetic conductors, the MR is relatively small and it is due to the Lorentz force that a magnetic field exerts on moving electrons. In magnetic materials the spin polarisation of the electrons gives rise to additional contributions and large magnetoresistance effects can be obtained, even in low magnetic fields.

At the end of the '80s, very high magnetoresistance was observed in Fe/Cr multilayers [12]. The resistance drops as the configuration of the magnetizations in neighbor Fe layers goes from antiparallel to parallel and the magnetoresistance ratio, given by eq. (1.3):

$$MR = -\frac{R(\uparrow\downarrow) - R(\uparrow\uparrow)}{R(\uparrow\uparrow)} \tag{1.3}$$

reaches 79% at 4.2 K for Cr layers of 9 Å thickness. Because of its high value, the observed effect was called *giant magnetoresistance* (GMR).

More recently, magnetoresistance of up to 40% at room temperature and 65% at 4.2 K was discovered in tunnel junctions, in which the two electrodes are ferromagnetic layers and the barrier consists of a thin insulating layer [120]. The effect, denoted as *tunneling magnetoresistance* (TMR), is based on the difference in the tunneling probability between the ferromagnetic electrodes for the spin up and spin down electrons (the tunnel resistance in the parallel and antiparallel configurations are different) [52].

A huge interest in the mixed–valence manganese perovskites was renewed after the discovery of the colossal magnetoresistance effect [141, 182], which is the magnetoresistance associated with a ferromagnetic to paramagnetic phase transition (Fig. 1.2).

The parent compound $LaMnO_3$ is an A–type[2] antiferromagnetic insulator and has a distorted cubic perovskite structure: the octahedra are elongated and tilted: the d–type Jahn–Teller distorsion (the elongated axes of the octahedra are parallel along the c axis) is accompanied by the $GdFeO_3$–type distorsion, caused by the tilting of the MnO_6 octahedra (Fig. 1.3) [119].

The electronic configuration of the Mn ions in this compound is a high spin $3d^4$ state. Due to the crystal–field, the $3d$ states are split into t_{2g} and e_g, as shown in Fig. 1.4. The e_g levels are further split by the Jahn–Teller effect, as shown in

[2]the ferromagnetic ab planes are antiferromagnetically coupled along the c axis.

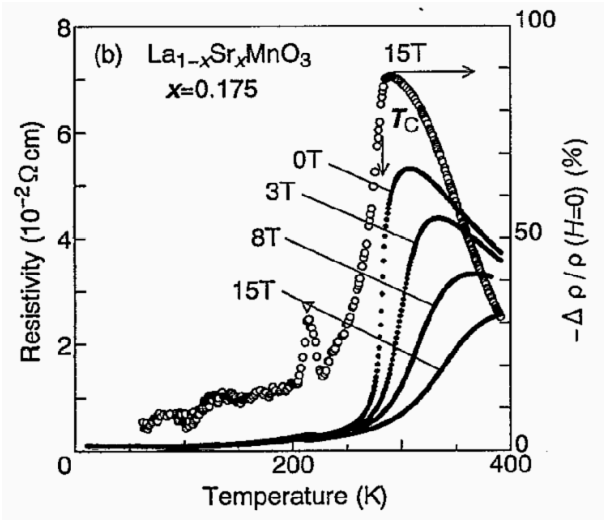

Figure 1.2: Temperature dependence of the resistivity and magnetoresistance for the single crystal $La_{0.825}Sr_{0.175}MnO_3$ [182]

Fig. 1.5. When $LaMnO_3$ is doped with divalent alkaline–earth cations (Sr, Ba, Ca), a charge redistribution from Mn^{3+} to Mn^{4+} takes place and for a doping range of $0.2 \div 0.5$, they exhibit colossal magnetoresistance effect.

Among the many reported CMR Mn–perovskites, $La_{1-x}Sr_xMnO_3$ has received a special attention. When La is substituted by Sr, the ordered spins are canted towards the c axis direction, a state that persist up to $x = 0.15$. Then the ferromagnetic phase appears; the Curie temperature increases with doping up to 30% and then saturates. For $x = 0.2$ an unusual metal–insulator transition has been observed, the resistivity in the metallic phase being four orders of magnitude larger than usually observed in metallic oxides. Also at higher doping, $x = 0.4$, the value of the resistivity is still too large.

In the last few years, new types of CMR materials have been reported [141]. A remarkable interest in magnetic chalcogenides has been renewed after the discovery of the colossal magnetoresistance effect in $Fe_{1-x}Cu_xCr_2S_4$ ($x = 0.0; 0.5$) close to room temperature (Fig. 1.6). $FeCr_2S_4$ and $Fe_{0.5}Cu_{0.5}Cr_2S_4$ are p– and n–type semiconducting ferrimagnets.

Unlike the manganese perovskites, the spinels are characterized by no mixed–valence, an A–site cation that can contribute to states near the Fermi level and

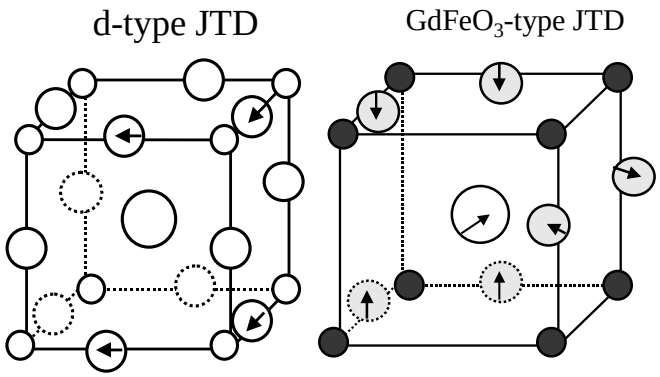

Figure 1.3: Simple representation of the d–type Jahn–Teller and $GdFeO_3$–type distorsions. The arrows indicate shifts of the O and La ions. For $GdFeO_3$–type distorsion, the six oxygen ions nearest to the La–site are shown [119].

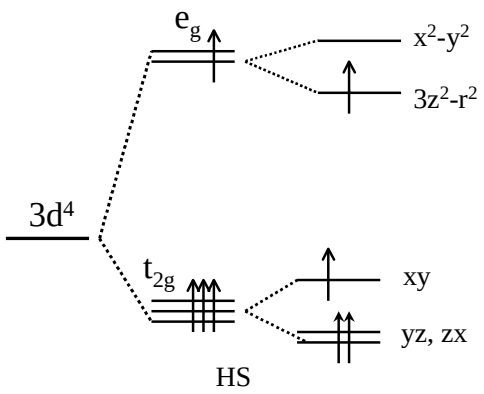

Figure 1.4: Crystal field splitting for the Mn^{3+} ions in an octahedral environment [170].

large deviations of the metal–anion–metal bond angle from 180°. Hence, additionally to the double–exchange and electron–phonon interactions, other mechanisms have to be considered in order to explain the CMR effect, observed not only in chromium spinels, but also in different classes of materials, as: pyrochlores $Tl_2Mn_2O_7$ [155], $Sr_{2-x}Nd_{1+x}Mn_2O_7$ [16], double–layered systems $La_{2-2x}Sr(Ca, Sn)_{1+2x}Mn_2O_7$ [121, 37, 10], $Eu_{14}MnBi_{11}$ [30].

An important property of the perovskites is the capability of controlling the band filling and the bandwidth, which are two important parameters for the strongly correlated systems and strongly coupled electron–phonon systems.

In order to explain the very interesting physics behind CMR in connection

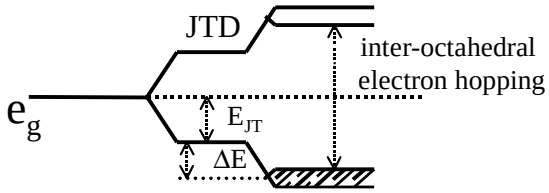

Figure 1.5: Schematic representation of the Jahn–Teller splitting for the e_g levels; the occupied bands are marked with hatched area [139].

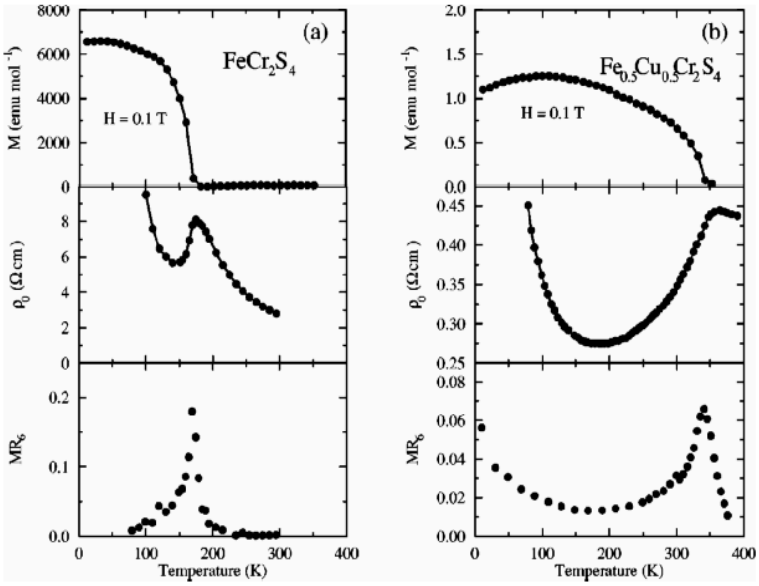

Figure 1.6: Magnetization (M), resistivity (ρ) and magnetoresistance (MR_H) versus temperature for $\mathrm{Fe}_{1-x}\mathrm{Cu}_x\mathrm{Cr}_2\mathrm{S}_4$ ($x = 0.0; 0.5$) [134].

with their potential applications for reading heads, magnetic sensors and other devices, further theoretical and experimental investigations of these compounds are desirable.

Chapter 2

X–ray photoelectron and X–ray emission spectroscopy

A very important and widely used experimental technique to obtain information about the occupied electronic states is the photoelectron spectroscopy (PES). The experiment is based on the *photoelectric effect*: when photons having enough energy ($h\upsilon$) to interact with a solid, electrons are ejected and it is the kinetic energy of the photoemitted electrons (E_{kin}) that is measured in a PES process (see Fig. 2.1).

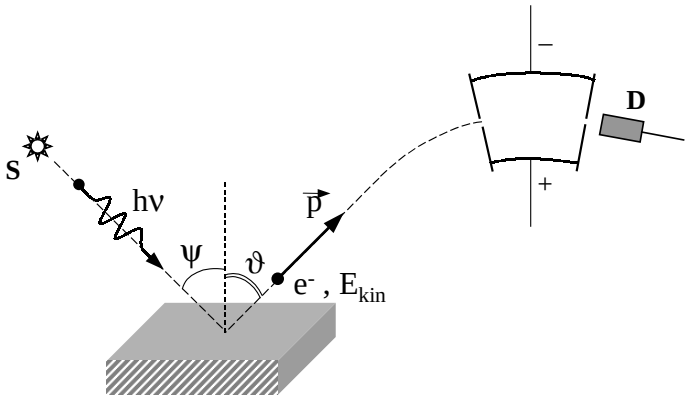

Figure 2.1: The principle of a PES experiment (after [71]).

During photoemission a hole is created at a certain level of the core or valence

orbitals. Whereas for the emission of the valence electrons only ultraviolet (UV) or soft X–ray radiation is required, for the core level emission high energy X–rays are necessary. The valence band and core level photoemission gives different types of spectra due to the fact that the number of the photoelectrons emitted at a certain energy depends on the density of states of the electrons in solid, as discussed later.

Depending on whether one uses UV or X–ray radiation, the technique is called Ultra Violet (UPS) or X–ray photoelectron (XPS) spectroscopy. XPS is an appropriate technique for the chemical analysis of materials, being very sensitive to the chemical environment, that is why it is often called ESCA (*E*lectron *S*pectroscopy for *C*hemical *A*nalysis) [162].

2.1 X–ray photoelectron spectroscopy

For a free atom or molecule, the energy conservation before and after photoemission is given by:

$$E_{in} + h\upsilon = E_{kin} + E_{fin} \tag{2.1}$$

where E_{in} and E_{fin} are the total initial and final energies of the atom or molecule before and after photoemission, respectively, $h\upsilon$ is the photon energy and E_{kin} is the photoelectron kinetic energy. The binding energy (E_B) for a given electron is defined as the energy necessary to remove the electron to infinity with zero kinetic energy. Therefore, one can write:

$$h\upsilon = E_{kin} + E_B \tag{2.2}$$

In eq. (2.2) the vacuum level is considered as reference level since it corresponds to a free atom (molecule). For the case of solids, the spectrometer and the solid are electrically connected in order to keep the system at a common potential during photoemission. Being connected, the Fermi levels of the spectrometer and solid become the same, as shown in Fig. 2.2 for a metal. Therefore, the kinetic energy of the photoelectron leaving the solid surface (E_{kin}) will be modified by the field[1] ($\Phi_s - \Phi_{sp}$) in such a way that in spectrometer one measures a photoelectron

[1] Φ_s and Φ_{sp} are the work functions of the solid and spectrometer, respectively.

kinetic energy E'_{kin}= E_{kin}+($\Phi_s - \Phi_{sp}$).

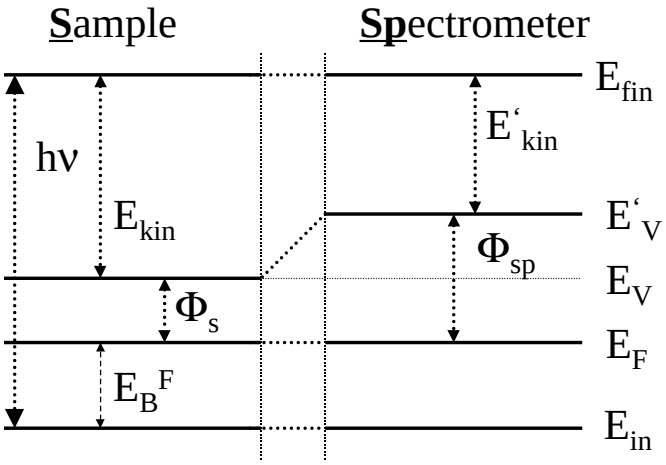

Figure 2.2: The energy level diagram for a solid electrically connected to a spectrometer [42].

The binding energy for the metallic solid relative to the Fermi level is then given by:

$$E_B^F = h\upsilon - E'_{kin} - \Phi_{sp} \tag{2.3}$$

2.1.1 Theoretical approaches to the photoemission process

A rigorous theoretical description of the photoemission process implies a full quantum–mechanical treatment of the process in which an electron is removed from an occupied state within the solid and then detected. Theoretical approaches of this type treat photoemission as a one–step process [21]. Less accurate, but very simple, is the three–step model that is a phenomenological approach [109, 138].

2.1.1.1 Sudden approximation

If one considers Ψ_{in} and Ψ_{fin} the wavefunctions corresponding to the initial and final states, before and after photoemission, the transition probability between the

two eigenfunctions of the same Hamiltonian H_0 obeys Fermi's golden rule (2.4), by assuming that the perturbation H^* applied to the system is small:

$$\omega \sim | \langle \Psi_{fin} \mid H^* \mid \Psi_{in} \rangle |^2 \, \delta(E_{fin} - E_{in} - h\upsilon) \tag{2.4}$$

The incident radiation, characterized by the vector and scalar potentials $\mathbf{A}$ and Φ, causes the perturbation of the system so that the initial Hamiltonian H_0 becomes H:

$$H = H_0 + \frac{e}{2mc}(\mathbf{A} \cdot \mathbf{P} + \mathbf{A} \cdot \mathbf{P}) - e\Phi + \frac{e^2}{2mc^2}|\mathbf{A}|^2 \tag{2.5}$$

The last three terms in (2.5) are the perturbation terms (H^*), e and m denote the electron charge and mass, c is the light speed and $\mathbf{P}$ stands for the momentum operator. By assuming that in the initial state there are N electrons in the considered system, the initial and final wavefunctions can be written in the sudden–approximation [2] as (2.6) and (2.7):

$$\Psi_{in}^{(N)} \sim \psi_{in}^{k} \Psi_{in}^{(N-1)} \tag{2.6}$$

$$\Psi_{fin}^{(N)} \sim \psi_{fin}^{E_{kin}} \Psi_{fin}^{(N-1)}, \tag{2.7}$$

in which ψ_{in}^{k} is the wavefunction of the k orbital and $\psi_{fin}^{E_{kin}}$ is the wavefunction of the photoelectron that has left out the k level with the kinetic energy E_{kin}. Hence, the matrix element $\langle \Psi_{fin} \mid H^* \mid \Psi_{in} \rangle$ is the product of a one–electron matrix, $\langle \psi_{fin}^{E_{kin}} \mid H^* \mid \psi_{in}^{k} \rangle$ and a (N–1) electron overlap integral, $\langle \Psi_{fin}^{(N-1)} \mid \Psi_{in}^{(N-1)} \rangle$.

In the *frozen–orbital approximation* the orbitals are assumed to remain unmodified during the photoemission process. Within this assumption $\Psi_{fin}^{(N-1)} = \Psi_{in}^{(N-1)}$ and the transition matrix element equals the one–electron matrix element. In this approximation, the binding energy measured in a XPS process is given by Koopmans' theorem: "*for a closed shell molecule the ionization potential of an electron in a particular orbital is approximately equal to the negative of the orbital energy calculated by an SCF* (self–consistent field) *ab initio method*" [88]:

$$E_B(k) = -\epsilon_k \tag{2.8}$$

[2] the photoelectron is emitted so fast, that there is only negligible interaction with the remaining (N-1) electron system [21].

The above equation is only approximately valid, since important effects were not considered, as [73]:

– the relaxation effects; after photoemission the orbitals in the excited system will be different as compared to the inital state. There is an intra–atomic relaxation related to the reorganization of the orbitals in the same atom and, additional, an extra–atomic relaxation connected with the charge flow from the crystal to the ion where the hole was created during photoemission [71]. Hence, additional to the orbital energy in (2.8) one has to take into account the relaxation (reorganization) energy (E_{relax}).

– the correlation effects, which are related to the fact that the electrons motions are not independent, but correlated (E_{corr}).

– the relativistic effects.

2.1.1.2 Three–step model

In this model [167, 19], the photoelectron process is considered as consisting of three independent events:

– the local absorption of the photon and the excitation of the (photo)electron (photoionization);

– the propagation of the electron through the sample to the surface;

– the penetration of the photoelectron through the surface and emission into the vacuum, where it is detected [109].

The first process, namely the optical excitation of the electron, is described by Fermi's golden rule (2.4). For an energy E and a wave vector around $\mathbf{k}$, the internal electron current I_{int} (E, hυ, $\mathbf{k}$) is given by[3]:

$$I_{int}(E, h\upsilon, \mathbf{k}) = \sum \mid \langle \Psi_{fin} \mid H^* \mid \Psi_{in} \rangle \mid^2 f(E_{in}) \\ \delta(E_{fin}(\mathbf{k}) - E_{in}(\mathbf{k}) - h\upsilon)\delta(E - E_{fin}(\mathbf{k})) \tag{2.9}$$

where f(E_{in}) is the Fermi distribution function.

[3]It is necessary to mention that only the electrons with energies above vacuum energy and with the final state vector $\mathbf{k}$ directed outwards from the surface ($\mathbf{k}_\perp > 0$) can be detected.

During the propagation to the surface, many electrons lose part of their energy by electron–electron and electron–plasmon scattering. The continuous background in the XPS spectrum is due to such electrons, which do not carry any more information about their initial states.

The transport probability $D(E, \mathbf{k})$, which describes the propagation process, is proportional to the mean–free path λ (2.10):

$$D(E, \mathbf{k}) \sim \lambda(E, \mathbf{k}) \tag{2.10}$$

where λ depends on energy E, electron wave vector $\mathbf{k}$ and the particular crystallographic direction.

The penetration of the electron through the surface depends on the transmission rate[4]:

$$T(E, \mathbf{k})\delta(\mathbf{k}_{\|} + G_{\|} - \mathbf{k}_{\|}^{\mathbf{ex}}) \tag{2.11}$$

Taking into account the three steps described above by (2.9), (2.22), (2.11), the detected (external) emission current can be written as (2.12):

$$I_{ext}(E, h\upsilon, \mathbf{k}_{\|}^{\mathbf{ex}}) = I_{int}(E, h\upsilon, \mathbf{k})D(E, \mathbf{k})T(E, \mathbf{k})\delta(\mathbf{k}_{\|} + G_{\|} - \mathbf{k}_{\|}^{\mathbf{ex}}) \tag{2.12}$$

2.1.2 Spectral characteristics

The spectroscopic notation of a state is nl_j, where n and l are the principal and orbital quantum numbers and $j = l \pm s$ ($s = 1/2$). For a given principal quantum number, l can take n values: 0, 1, 2, 3,... $(n-1)$ and the corresponding levels are denoted as *s, p, d, f,...,* respectively.

2.1.2.1 Core levels

The XPS lines associated with core levels are usually sharp, may have variable intensities and widths and, except the s levels, are doublets. The doublet character of the core lines arises through the spin–orbit $(j-j)$ coupling. In the $j-j$

[4] $\mathbf{k}_{\|} + G_{\|} = \mathbf{k}_{\|}^{\mathbf{ex}}$ is required by the conservation of the electron wave vector parallel to the surface.

coupling, the total angular momentum of one electron (j) is given by the sum of the electronic spin and angular momenta ($j = l + s$). To obtain the total angular momentum of an atom (J), one has to sum all total angular momenta of the constituent electrons: $J = \Sigma j$. Therefore, except the case of $l = 0$ (s levels), for each state *(nl)* there will be a double–line (doublet) in the XPS spectrum: $nl_{l+1/2}$ and $nl_{l-1/2}$, respectively, of which relative intensities are given by (2.13):

$$\frac{I_{(l+1/2)}}{I_{(l-1/2)}} = \frac{l+1}{l} \tag{2.13}$$

For example, for $l = 1$ (p levels), the relative intensities of the corresponding doublet, $p_{3/2}$ and $p_{1/2}$ are $2:1$, whereas for $l = 2$ (d levels), $\mathrm{I}_{5/2}/\mathrm{I}_{3/2} = 3/2$.

The width of a XPS core line depends upon several factors of inherent and instrumental nature: the lifetime of the core hole created during photoemission, unresolved chemically–shifted peaks, multiple final states and X–ray linewidth, the finite resolution of the analyser, etc. [22]. The peak width (FWHM = *full width at half–maximum*) can be written as (2.14):

$$\Delta E = \sqrt{(\Delta E_n)^2 + (\Delta E_p)^2 + (\Delta E_a)^2} \tag{2.14}$$

where ΔE_n represent the natural width of the core level, ΔE_p and ΔE_a being connected with the spectrometer, namely the width of the X–ray line and the analyser resolution, respectively [22].

For metals, the lines have an asymmetric form, due to the screening effect by the conduction electrons [98]. They are well described by the Doniach–Sunjic formula [46]:

$$I(E - E_0) = \frac{\Gamma(1-\alpha)\cos[\pi\alpha/2 + (1-\alpha)\arctan(E - E_0)/\gamma]}{[(E - E_0)^2 + \gamma^2]^{(1-\alpha)/2}} \tag{2.15}$$

where E_0 is the center of the energy distribution curve for the core line, Γ is the Γ function, α and γ are parameters. For insulators and semiconductors $\alpha = 0$, and eq. (2.15) is reduced to a Lorentz–type line.

The *equivalent–core approximation* is often used to determine the core–level binding energies. In this model the photoionisation of a core level is assumed to be equivalent with the addition of a positive charge ($+e$) to the nucleus, this is why it is often called the *(Z+1) approximation* [50].

Chemical shifts

The binding energies of a certain core level for non–equivalent atoms (with different formal oxidation states, surrounded by different chemical environments, having different lattice sites) are different. The binding energy difference is called *chemical shift*, by analogy with nuclear magnetic resonance spectroscopy. It can be regarded as the result of a change in the spatially–averaged Coulomb and exchange potentials exerted upon an electron by its environment.

There are many theoretical procedures to calculate chemical shifts. *Self–consistent field* (SCF) calculations can be carried out, either by using the non–relativistic Hartree-Fock formalism or the relativistic Dirac–Fock method [42]. An accurate binding energy can be calculated if one takes into account relaxation, correlation and relativistic effects:

$$E_B = -\varepsilon_k - \delta E_{relaxation} + \delta E_{correlation} + \delta E_{relativistic} \tag{2.16}$$

Another alternative is given by the so called *charge potential model*, where the core binding energy is considered to depend on the potentials created by the valence electrons of the considered atom and also by the electrons from the neighboring atoms [59]. Hence, the shift in the binding energy of an atom (i) in a molecule/solid with respect to the binding energy of the same core electron of the same atom in a reference compound can be written as:

$$\Delta E_B^i = a\left[\left(\frac{q_i}{r_i}\right) - \left(\frac{q_i}{r_i}\right)_{Ref}\right] + a\left[\sum_{i\neq j}\left(\frac{q_j}{r_{ij}}\right) - \sum_{i\neq j}\left(\frac{q_j}{r_{ij}}\right)_{Ref}\right] \tag{2.17}$$

where q_i and r_i represent the charge and radius of the valence shell of the atom (i), q_j denotes the charge of the neighboring atom (j) and r_{ij} are the distances between the atom (i) and its neighbors (j). The two terms in square brackets reflect the intra–atomic and inter–atomic potentials.

An important application of the core–level analysis is the study of the structural properties from the chemical shifts. The core–level spectroscopy can be also used for the observation and investigation of phase transitions [98].

2.1.2.2 Valence band levels

Whereas the core levels are usually reflected by well–resolved sharp XPS peaks, the valence band spectra are characterized by a band structure (many closely spaced levels) [22]. The valence electrons involved in the delocalized or bonding orbitals have low binding energies (< 20 eV). Because of the lower cross–sections of the valence photoelectrons as compared to the core photoelectrons, the valence band spectra intensity will appear much lower than for the core level spectra.

From the valence band one can get information about the electronic structure of the investigated systems. When the photon energy varies, the relative intensities of the various valence electrons peaks can drastically change because the relative photoionization cross sections[5] of the various electronic states will change. This effect can be used to obtain information about the partial contributions to the total density of states for different constituents of a system (for example, by comparing the UPS and XPS valence band spectra[6] of a transition metal oxide, one can get information about the relative partial contributions of the metal $3d$ and O $2p$ states in the valence band).

2.1.2.3 Multiplet splitting

Multiplet (exchange) splitting of the core level lines can occur for systems with unpaired electrons in the valence levels. If one considers the photoemission from the $3s$ core levels of transition–metal compounds, because the spin $s = 1/2$ of the core hole created during photoemission can couple parallel or antiparallel to the total spin of the valence electrons (S), the core line will split and the exchange splitting (ΔE_s) can be written, according to the van Vleck theorem [184]:

$$\Delta E_s = \frac{2S+1}{2l+1} G^2(3s, 3d) \tag{2.18}$$

where $G^2(3s, 3d)$ is the Slater exchange integral and l is the orbital quantum number ($l = 2$). The binding energy of the state with spin $(S + 1/2)$ is lower than the binding energy corresponding to $(S - 1/2)$, as indicated in Fig. 2.3.

[5] for a detailed description about how they can be determined see [42, 59].

[6] both give information about the total density of states.

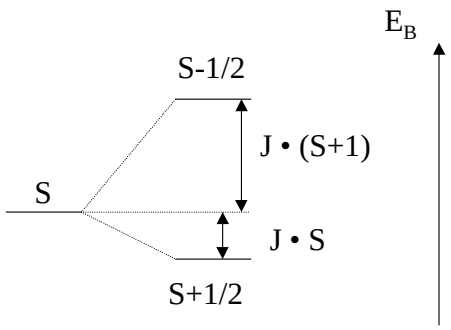

Figure 2.3: Scheme of the $3s$ exchange splitting.

The intensity ratio for the two peaks is given by:

$$\frac{I_{S+1/2}}{I_{S-1/2}} = \frac{S+1}{S} \tag{2.19}$$

More than 30 years ago it has been found that there are spectra for which the van Vleck theorem is not fulfilled: the multiplet intensities ratio was higher than that predicted by (2.19), whereas the value of the splitting was about two times smaller than expected [51]. To explain these discrepancies, correlation effects, configuration interaction and covalence have been considered [161, 129].

For the other core levels ($l \neq 0$), the multiplet splitting is more complex because an additional spin–orbit splitting occurs in spectra.

Charge–transfer satellite

For many TM compounds, the interpretation of the core level spectra is more complicated. In many TM compounds (as Cu dihalides, CuO–see (Fig.4.3), NiO [181]) the $2p_{3/2}$ and $2p_{3/2}$ lines are accompanied by additional peaks, the so called charge–transfer satellites. When one notes with L the ligand shell (oxygen, for TM oxides), the charge–transfer process refers to a transfer of one electron from the ligand $2p$ (L) to the metal $3d$ shell: $3d^nL \rightarrow 3d^{n+1}L^{-1}$. The energy required by this charge transfer (Δ) is therefore given by (2.20):

$$\Delta = E(d^{n+1}L^{-1}) - E(3d^nL) \tag{2.20}$$

Depending on whether Δ is lower or exceeds the correlation energy, one can talk about charge–transfer or Mott–Hubbard compounds [200]. Whereas the late TM oxides can be regarded as CT compounds, the situation is very complicated for the middle row TM compounds, where correlation and hybridization effects play both an important role.

A suggestive illustration of the two limit cases, Mott–Hubbard (MH) and charge–transfer (CT), is presented in Fig. 2.4.

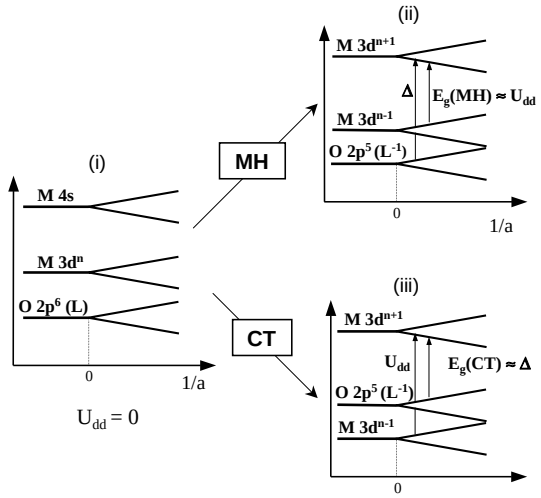

Figure 2.4: One–electron (i), Mott–Hubbard(ii) and charge–transfer (iii) diagrams of a metal transition oxide [71].

2.1.2.4 Shake–up and shake–off

Simultaneously with the removal of a core electron during the photoemission process, a second electron can be transferred to another orbital with higher energy in a *shake–up* process or can be completely removed in a *shake-off* process (see Fig. 2.5). The energy necessary for either process is supplied from the kinetic energy of the photoelectron produced during the initial ionization. Therefore, the corresponding satellites in the XPS spectrum will appear on the high binding (low kinetic) energy side of the main peaks. For the electron involved in a shake–up or shake–off process the selection rules: $\Delta l = 0$, $\Delta s = 0$, $\Delta j = 0$ are fulfilled. Therefore, only a change of n can occur in the shake–up and shake–off

processes [73].

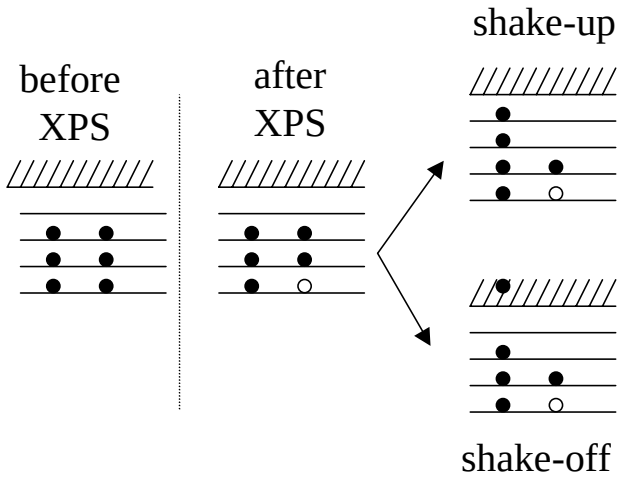

Figure 2.5: Electron shake–up and shake–off processes following ionization [73].

2.1.2.5 Background corrections

During their transport to the surface, some photoelectrons lose part of their energy through inelastic scattering processes and end up at a lower energy in the spectrum, giving rise to a 'background'. For quantitative analysis of the XPS spectra, the true peaks area and their shapes need to be determined. Therefore, ussually background corrections are applied. Shirley [160] proposed a method in which the background intensity within a peak is proportional to the integrated intensity at higher energy with the presumption that the background matches the spectrum outside the peak region. In the Tougaard algorithmus [173, 174] the measured spectra $j(E)$ is considered to consist of photoelectron spectra $F(E)$ and background, as given in eq. (2.21):

$$j(E) = F(E) + \lambda(E) \int_{E}^{\infty} K(E, E - E')j(E)dE' \tag{2.21}$$

where $K(E, E' - E)$ describes the probability that an electron with the energy E loses the energy $(E' - E)$ during a mean free path travel. The loss function $\lambda(E)K(E, E - E')$ can be described for many materials with a reasonable approximation by[7]:

$$\lambda(E)K(E, E - E') \simeq \frac{B(E - E')}{[C + (E - E')^2]^2} \tag{2.22}$$

2.2 X–ray photoemission spectroscopy

Two additional processes can simultaneously occur with the photoionization. The ions produced during the photoemission process can relax by emitting X–ray radiation (*fluorescence*) or by the ejection of a second electron (*Auger process*), as illustrated in Fig. 2.6.

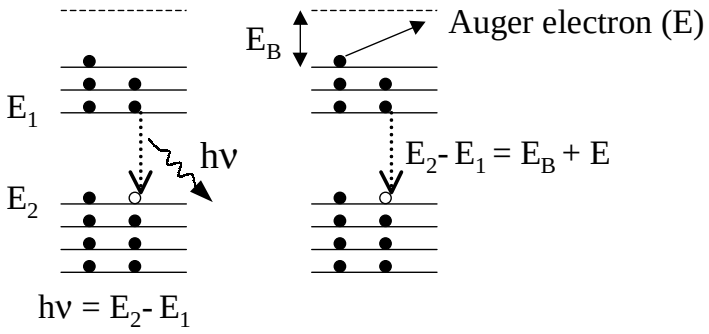

Figure 2.6: Schematic representation of the X–ray emission and Auger processes

X–ray emission

The first process, namely the X–ray emission, obeys the following selection rules: $\Delta l = 1$ and $\Delta j = 1; 0$, if one only considers the electric dipole vector of the radiation. The probability of ions relaxation via dipolar emission is more than two times larger than that corresponding to the electric quadrupoles or to the magnetic dipol vector, therefore the last two can be usually neglected [24].

[7] B=2886 eV^2 and C=1643 eV^2.

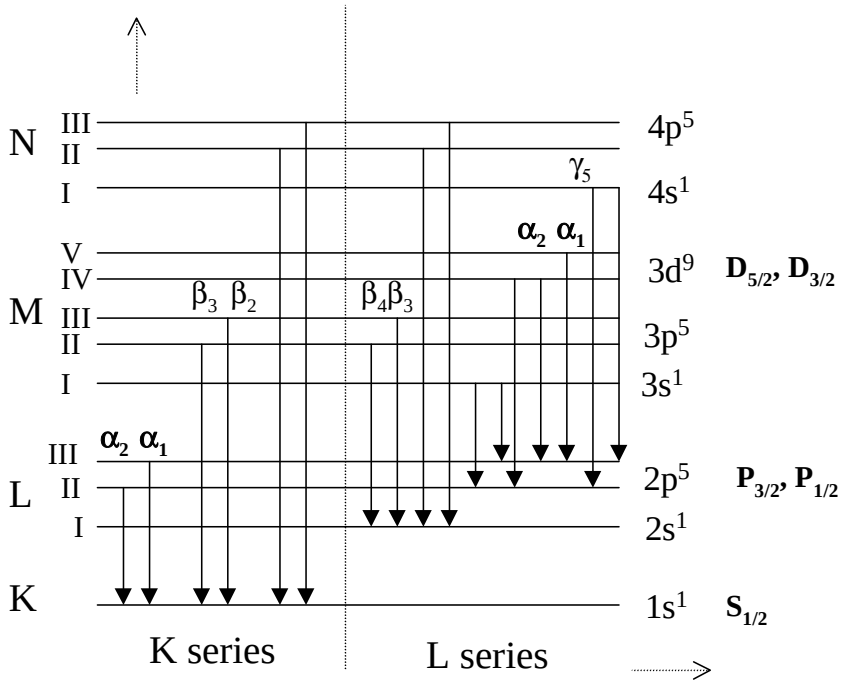

Figure 2.7: Schematic diagram of the main X–ray emission lines in the K and L series [24].

The X–ray emission lines are called after the name of the shell where the initial vacancy was created during the ionization process: K ($l = 0$), L ($l = 1$), M ($l = 2$), etc., followed by a Greek letter (α, β,...) and numerical subscripts, as indicated in Fig. 2.7.

The X–rays emitted from singly ionized ions may arise from inner (core) orbital to inner orbital transitions or from valence–shell to inner orbital transitions. The last type of X–ray emission spectra, which contains information about the nature and structure of the chemical bond, has been analyzed in the present work. We have used the transition metal $L\alpha$ ($3d \rightarrow 2p$ transitions) and O $K\alpha$ ($2p \rightarrow 1s$ transitions) XES spectra to obtain information about the metal $3d$ and oxygen $2p$ partial densities of states and, implicitly, to interpret the valence band XPS spectra of the investigated transition metal compounds. In order to bring the XPS and XES spectra on the same energy scale, the common procedure was used: one measures the ionization energy of the inner orbital level involved in the X–ray emission by XPS (for example, TM $2p$ and O $1s$ when one studies the TM

$L\alpha$ and O $K\alpha$ XES spectra). Then, the XES spectra can be easily brought to the binding energy scale by difference.

The Auger process

The second way of ion relaxation is the ejection of a second electron in an Auger process. To describe it, the following nomenclature is used: XYZ, where X stands for the hole's shell, Y denotes the shell from where the recombination starts and Z labels the shell from where the Auger electron is emitted. The X (Y or Z) are named K for the $1s$ levels, L_I, L_{II} and L_{III} for $2s$, $2p_{1/2}$ and $2p_{3/2}$, M_I, M_{II}, M_{III}, M_{IV} and M_V for $3s$, $3p_{1/2}$, $3p_{3/2}$, $3d_{3/2}$ and $3d_{5/2}$, respectively [42]. For example, the KL_IL_{II} line corresponds to the case when a hole from the $1s$ shell is filled by an electron from the $2p_{1/2}$ shell and the resulting energy is taken by an electron from the $2p_{3/2}$ shell, which is emitted as Auger electron[8].

If the initial and final hole states are on the same shell, but in different orbitals (for example, $L_IL_{III}M_I$) the process is called of *Coster–Kronig* type [98].

2.3 Experimental details

Most of the presented XPS results were obtained by using the PHI 5600 multi–technique spectrometer[9] (Fig. 2.9). The main components of this spectrometer are: the X–ray source, monochromator, electron energy analyzer, main chamber, ion gun, neutralizer, as shown in Fig. 2.8.

As concerning the radiation source, the PHI 5600 spectrometer is equipped with a dual Al/Mg anode. The energies of Al $K\alpha$ and Mg $K\alpha$ radiations are 1486.6 eV and 1253.6 eV and their half–widths for the unmonochromatized radiation are 0.85 eV and 0.7 eV, respectively. $K\alpha$ indicates that an electron has been ejected from the K shell and the radiation is due to an electron from the L shell that occupies the hole created in the K shell. By using a monochromator[10],

[8] Other authors use instead of I, II, III, IV, etc. the notation: 1, 2, 3, 4... and, therefore, the Auger KL_IL_{II} line will be denoted as KL_1L_2.

[9] for a detailed description of the spectrometer, see [137, 112].

[10] A monochromator works on the basis of the constructive interference from crystal diffraction, as given by Bragg equation: $n\lambda = 2d\sin\theta$, where d represents the distance between lattice

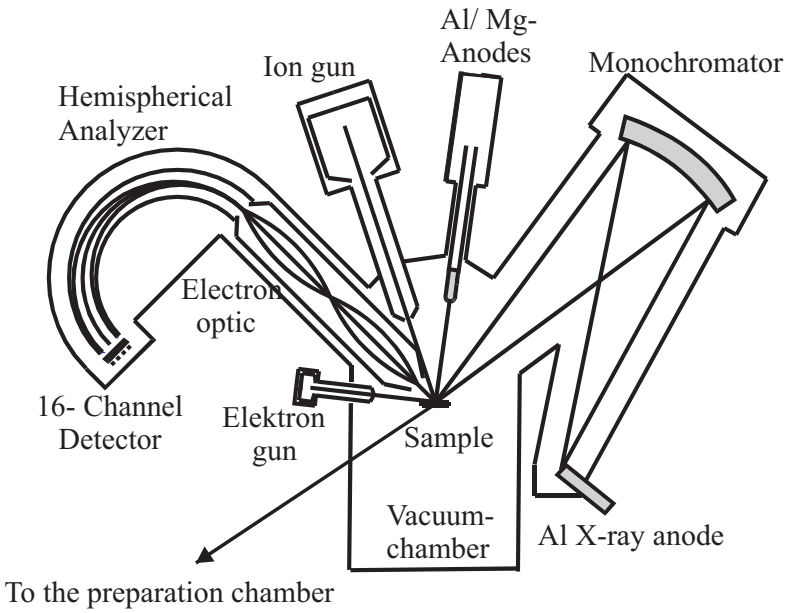

Figure 2.8: Schematic diagram of the PHI 5600 spectrometer [82]

the halfwidth of the Al $K\alpha$ radiation is reduced to ~ 0.3 eV.

The role of the neutralizer is to supply low–energies electrons to insulating samples, which can otherwise develop positive charges due to the photon bombardement.

In order to keep clean surfaces for the investigated samples during measurements - which can take up to few hours -, ultra–high vacuum is required. For all measurements presented in this study, the pressure in the main chamber was kept below 1×10^{-9} torr.

The low–temperature measurements were performed with a similar PHI 5700 spectrometer at the Silesian University of Katowice (Poland)[11].

All XPS spectra presented in this work were recorded using Al Kα monochromatic radiation. The investigated samples were cleaved in high vacuum before measuring, so that fresh clean surfaces were obtained. In very few cases, the neutralizer was used in order to compensate the charge effects that occur for

planes, λ is the radiation wave length and θ is the angle between the incident radiation and the deflecting planes.

[11] We thank all ESCA laboratory members for assistance during measurements.

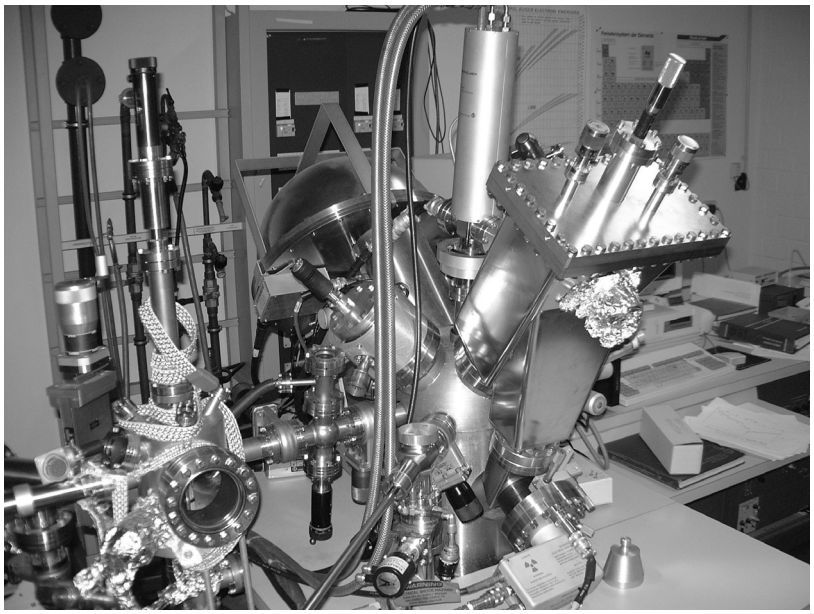

Figure 2.9: PHI 5600 spectrometer

non–conducting samples.

The X–ray emission measurements were performed at the Institute of Metal Physics, Ekaterinburg (Russia)[12]. The Mn Lα and O Kα X–ray emission spectra were measured with a RSM–500 type X–ray vacuum spectrometer with a diffraction grating (N=600 lines/mm, R=6 m) and electron excitation [207]. The sample is mounted on the X–ray tube anode (hollow copper cylinder cooled with water). The electron beam emitted by the cathode (tungsten filament) is vertically focused, so that the spot on the sample has a 10 mm height and 0.2 mm width. The radiation from the specimen is focused onto the fixed entrance slit by a spherical mirror at grazing incidence, as shown in Fig. 2.10[13]. The radiation is detected using a secondary electron amplifier with a CsI coated photocathode. The energy resolution was about 0.8$\div$1.3 eV.

The Mo L$\beta_{2.15}$ X–ray emission spectra were recorded using a fluorescent Johan–type spectrometer with a position–sensitive detector [45]. Pd L X–ray radiation from a sealed X–ray tube was used for the excitation of the fluorescent

[12]We acknowledge Prof. Kurmaev group for providing the XES spectra.

[13]the grating and exit slit can move, as indicated in the figure. The grating is rotated so that the diffraction angle θ remain constant, whereas the incidence angle φ changes ($0 \div 6$o)

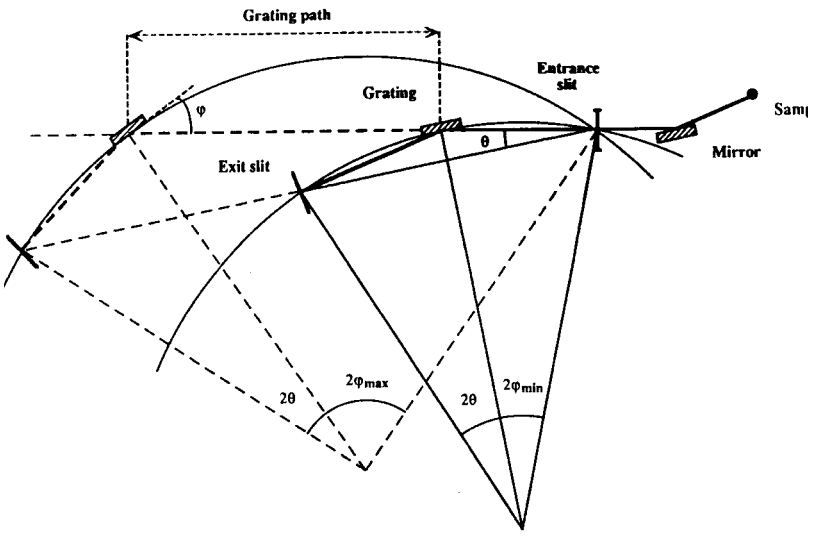

Figure 2.10: Scheme of the RSM–500 spectrometer [207]

Mo L$\beta_{2,15}$ spectra. A quartz (1010) single crystal curved to $R = 1400$ mm was used as a dispersion element. The energy was detected with an accuracy of $\pm$ 0.25 eV.

2.4 Electronic structure calculations–overview

The electronic structure of materials in question is obtained by solving the non–relativistic many–body Schrödinger equation (2.23):

$$\left[-\frac{\hbar^2}{2m}\sum_i \nabla_i^2 - \sum_{i,k}\frac{Z_k e^2}{|r_i - R_k|} + \frac{1}{2}\sum_{i\neq j}\frac{e^2}{|r_i - r_j|}\right]\Psi = E\Psi \qquad (2.23)$$

where R_k, Z_k are the positions and atomic numbers of the nuclei considered fixed (Born–Oppenheimer approximation) [87].

When one uses the first–principles (*ab initio*) calculations to determine the electronic structure of a given material, one starts from atoms and electrons with their mutual Coulomb interactions in the continuum space. There are several approximations that can be employed [76] in order to reduce the insoluble many–particle problem (2.23) to a soluble one–electron equation:

a) configuration–interaction method (by diagonalization of the Hamiltonian matrix, small clusters under the atomic potential with the relevant electronic orbitals can be exactly solved);

b) Hartree–Fock approximation; one considers a single Slater determinant as a variational state of the many–body hamiltonian from (2.23). The single–particle state $\psi_l(r_i)$ is determined by energy minimization and solving of the self–consistent eq (2.24):

$$\begin{aligned}&\left[-\frac{\hbar^2}{2m}\Delta + V_{lat}(r) + \sum_{l'}\int dr' \frac{e^2}{|r-r'|}|\psi_{l'}(r')|^2\right]\psi_l(r) \\ &-\sum_{l'}{}' \left[\int dr \frac{e^2}{|r-r'|}\psi^*_{l'}(r')\psi^*_l(r')\right]\psi_{l'}(r) = \varepsilon_l\psi_l(r)\end{aligned} \tag{2.24}$$

where $V_{lat}(r)$ denotes the atomic periodic potential of the lattice and $\sum_{l'}{}'$ is taken over those l' that have the same spin as l (l and l' –quantum numbers including orbital degrees of freedom). The last term of the eq. (2.24) represents the exchange term and can be written as (2.25):

$$V^l_{ex}\psi_l(r) \tag{2.25}$$

where

$$V^l_{ex}\psi_l(r) = \int dr' \rho^l_{ex}(r,r')\frac{e^2}{|r-r'|} \tag{2.26}$$

and

$$\rho^l_{ex}(r,r') = \frac{\psi^*_l(r)\psi_l(r')\sum_{l'}{}'\psi^*_{l'}(r')\psi_{l'}(r)}{|\psi_l(r)|^2} \tag{2.27}$$

One difficulty of the Hartree–Fock formalism is that the exchange potential V^l_{ex} depends on the solution $\psi_l(r)$ itself. The correlation interaction between the electron with different spins is not considered, therefore to calculate systems with strongly correlated electrons, different ways to take into account these correlation effects have to be considered.

(c) local–density approximation (LDA)[14]; it is based on the density–functional theory [87]. In this approximation the exchange–correlation potential $V_{xc}(r)$ in (2.28) is calculated from the uniform electron gas with the density $n(r)$ (2.29):

$$V_{xc}(r) = \int dr' \rho_{xc}(r, r') \frac{e^2}{|r - r'|} \tag{2.28}$$

$$n(r) = \sum_l |\psi_l(r)|^2 \tag{2.29}$$

In order to make possible the calculation of spin–density waves or antiferromagnetic state, the local spin–density approximation has been developed (LSDA)-[76]. Here, one introduces the spin–dependent electron densities, $n_\uparrow(r)$ and $n_\downarrow(r)$, so that the exchange correlation energy (2.30) is replaced by (2.31):

$$\int dr V_{xc}(r) n(r) \tag{2.30}$$

$$\int dr [n_\uparrow(r) + n_\downarrow(r)] V_{xc}[n_\uparrow(r), n_\downarrow(r)] \tag{2.31}$$

However, the LSDA fails to reproduce the AF ground state of many compounds with strongly correlated electrons, where the correlation effects cannot be appropriately treated within this approximation. The electron correlation is in general large when two electrons having the spins up and down occupy the same atomic orbital of the TM atom. The spatial extension of the d orbital determines the Coulomb repulsion between the two electrons.

To consider the correlation effects, a combination of the LDA and Hartree–Fock approximation (LDA+U) has been developed, with good results for many TM compounds [8]. The difficulty of this approach is related to the way of choosing U, which depends on the different choices of the local atomic orbital in the basis set, such that the LMTO (liniar muffin–tin orbital) and LCAO (the

[14]Since our results were mainly compared with LDA calculations, we will give a short description of this method.

liniar combination of atomic orbitals) calculations could give different results for U.

Although many efforts have been done in the last few years [7], the band structure calculations have difficulties in including charge and spin fluctuations effects and, therefore, in describing the metallic states near the Mott insulator, where the mentioned effects play an important role [76].

Chapter 3

Manganese perovskites

In the last few years the manganese perovskites, $La_{1-x}A_xMnO_3$ (A= Sr, Ba, Ca, Pb) have been the subject of intense experimental and theoretical studies due to the colossal magnetoresistance effect (CMR) that occurs in the low–doping regime [141, 186, 79, 141].

The parent compound $LaMnO_3$ is an A–type antiferromagnetic insulator with orthorhombic crystal structure [61]. The structure can be considered as cubic (Fig. 3.1) with two types of distorsions: local tetragonal Jahn–Teller distorsion of the oxygen atoms around each Mn site and tilting of the MnO_6 octahedra (the Mn–O–Mn angles become less that 180°). In the A–type antiferromagnetic order the spins are parallel aligned in plane and antiparallel between planes (see Fig. 3.1). The electronic configuration of the Mn^{3+} ions is a high–spin $3d^4$ state with three electrons in the $t_{2g\uparrow}$ band and one in the $e_{g\uparrow}$ band. The t_{2g} orbitals are weakly hybridized with the O $2p$ states, therefore the t_{2g} electrons can be regarded as localized by the strong correlation effects (S=3/2). The e_g orbitals are strongly hybridized with the oxygen $2p$ states.

Orbital ordering in $LaMnO_3$ was recently experimentally observed [124], which confirms the much earlier scheme of the orbital ordering proposed by Goodenough [60]. Several theoretical studies have analyzed the above mentioned phenomenon in relation with the lattice distorsion that plays a very important role in stabilizing the A–type antiferromagnetic order [166, 48, 119, 139].

When $LaMnO_3$ is doped with divalent alkaline–earth cations A^{2+}, a charge redistribution from Mn^{3+} to Mn^{4+} takes place. In a doping range of $0.2 \div 0.5$

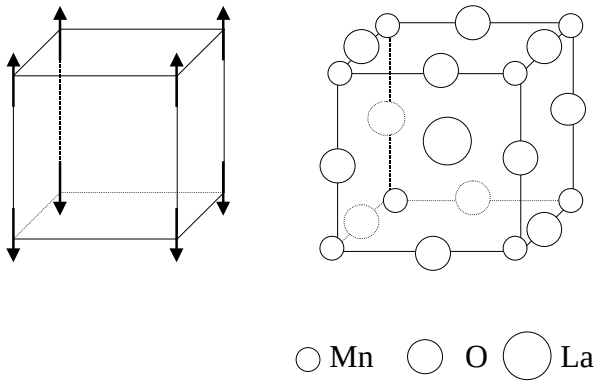

Figure 3.1: The A–type antiferromagnetic structure (left) and the ideal cubic perovskite structure of $LaMnO_3$ (right); arrows denote the spin–up and spin–down orientations.

these manganites undergo a paramagnetic insulator to ferromagnetic metal phase transition upon cooling, giving rise to a sharp resistivity peak near the Curie temperature T_C. By applying an external magnetic field, the resistivity is strongly suppressed and the sharp peak position shifts to higher temperatures, producing a large negative magnetoresistance. The first explanation of this effect was given by the *double–exchange model*, which assumes that the conduction is achieved through the hopping of an electron from the e_g state of the Mn^{3+} ions into the unoccupied e_g band of the Mn^{4+} ions [204, 6, 40]. Later it has been shown that one has to take into account the electron–phonon interaction in order to explain the high values of the resistivity at $T > T_C$ or the large drop in resistivity just below T_C [117, 118]. The microscopic origin of the strong electron–phonon coupling is the large Jahn–Teller effect that occurs for d^4 ions in an octahedral environment [77, 78]. Other effects playing an important role in the CMR scenario are: the ferromagnetic/antiferromagnetic superexchange interaction between the local spins, intersite exchange interaction between the e_g orbitals and intra-site and intersite Coulomb repulsions among the e_g electrons [170].

3.1 Sr–doped manganese perovskites

The electronic and magnetic diagram of $La_{1-x}Sr_xMnO_3$ has been established from electrical and magnetic measurements [182, 171]. For $x < 0.1$ the system is an antiferromagnetic spin–canted insulator and for $0.1 < x < 0.17$ it is a ferromagnetic insulator. For $x = 0.175$ there is a phase transition from orthorhombic to rhombohedral at room temperature. For $x > 0.2$ an unusual transition from FM insulator to FM metal takes place [172].

Several spectroscopic studies of the electronic structure of $La_{1-x}Sr_xMnO_3$ (polycrystals) have been previously reported [146, 152, 147, 90]. Strong changes in the valence band temperature–dependent photoemission spectra of $La_{1-x}Sr_xMnO_3$ were observed and they were related to the degree of hole localization on oxygen $2p$ orbitals [28, 151, 149]. For the $La_{1-x}Sr_xMnO_3$ single crystals there are very few XPS data up to now [97].

We present here an investigation of the $(La_{0.9}Sr_{0.1})_{0.9}MnO_3$, $La_{0.8}Sr_{0.2}MnO_3$ and $La_{0.7}Sr_{0.3}MnO_3$ single crystals by means of X–ray photoelectron and X–ray emission spectroscopy. The new experimental data are compared with those previously reported on similar polycrystalline compounds. They are discussed in relation to the band structure calculations available from literature.

- *Experimental details*

Single crystals of $(La_{0.9}Sr_{0.1})_{0.9}MnO_3$, $La_{0.8}Sr_{0.2}MnO_3$, $La_{0.7}Sr_{0.3}MnO_3$ were grown by the floating–zone method at the Moscow Institute of Steel and Alloys[1]. The initial samples were prepared by the standard ceramic procedure from a mixture of Mn_2O_3, La_2O_3, and $SrCO_3$ or $BaCO_3$ powders.

The X–ray photoelectron spectra were recorded using the PHI 5600 spectrometer with monochromatic Al Kα radiation. All samples were measured after breaking in ultra–high vacuum ($< 1 * 10^{-9}$ torr). The spectra were recorded at room temperature and calibrated using an Au–foil ($E_B(4f_{7/2}) = 84.0$ eV). The energy resolution as determined at the Fermi level of the Au–foil was ~ 0.4 eV.

[1]Prof. Ya. M. Mukovskii is acknowledged for supplying the single crystals.

The Mn Lα (Mn $2p_{3/2} \rightarrow$ Mn $3d4s$ transitions) and O Kα (O $1s \rightarrow$ O $2p$ transitions) X–ray emission spectra were measured with a RSM–500 X–ray vacuum spectrometer having an energy resolution of $\sim 0.8 \div 1.3$ eV .

3.1.1 XPS Mn $2p$ and $3s$ spectra

The XPS Mn $3s$ spectra can be used to estimate the valence state of manganese ions in Sr–doped $LaMnO_3$. It is well known that the magnitude of the Mn $3s$ splitting, which originates from the exchange coupling between the $3s$ hole and $3d$ electrons, is proportional to the local spin of the $3d$ electrons in the ground state [184].

The Mn 3s XPS spectrum of $(La_{0.9}Sr_{0.1})_{0.9}MnO_3$ is presented in Fig. 3.2. The exchange splitting (ΔE_s) is 5.3 eV, corresponding to a Mn valency between 3+ and 4+.

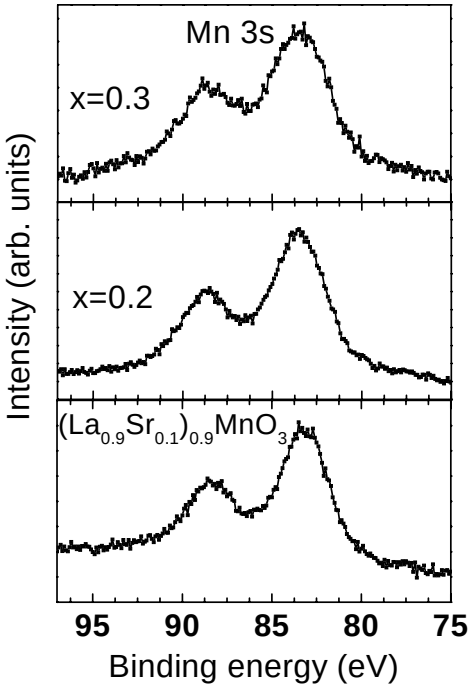

Figure 3.2: The XPS Mn $3s$ spectra of $(La_{0.9}Sr_{0.1})_{0.9}MnO_3$, $La_{0.8}Sr_{0.2}MnO_3$ and $La_{0.7}Sr_{0.3}MnO_3$ (single crystals).

In the above figure (Fig. 3.2) the Mn 3s XPS spectra of $La_{0.8}Sr_{0.2}MnO_3$ and

$La_{0.7}Sr_{0.3}MnO_3$ are shown. The Mn $3s$ exchange splitting is the same as for $(La_{0.9}Sr_{0.1})_{0.9}MnO_3$. It appears that in this doping range (x< 0.3) the electronic configuration of the Sr–doped manganites does not change.

For $La_{0.84}Sr_{0.16}MnO_3$ a smaller value of the Mn 3s exchange splitting was previously reported [97]. Polycrystalline samples of $La_{1-x}Sr_xMnO_3$ (x = 0.0, 0.1, 0.3, 0.5, 0.9) were also investigated by XPS and an increase in the exchange splitting when x decreases was observed, including the low–doping regime [146]. However, for $x < 0.3$ we did not observe any changes in the Mn $3s$ splitting for single crystals of $La_{1-x}Sr_xMnO_3$.

In Fig. 3.3 the Mn $3s$ spectra of several Mn oxides are presented. One can observe different exchange splitting values for compounds with different manganese ions: Mn^{2+} (MnO), Mn^{3+} ($LaMnO_3$) and Mn^{4+} ($SrMnO_3$). The value of the splitting decreases when the formal valence of Mn increases, as shown in Fig. 3.4. For MnO the main peak is mainly due to the $3s^1 3d^5$ states and for $LaMnO_3$ the main line corresponds to a $3s^1 3d^4$ final–state configuration [57].

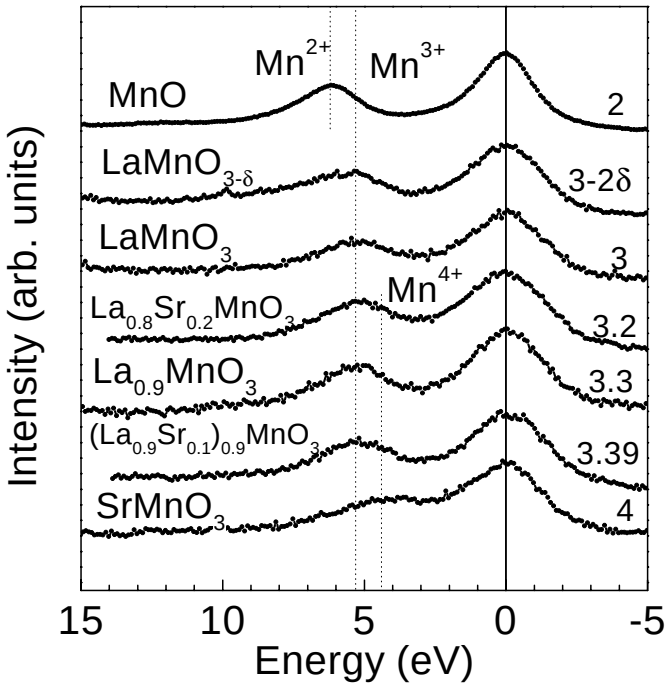

Figure 3.3: The Mn $3s$ splitting for manganese oxides with different Mn ions; on the left side the numbers indicate the formal Mn valence.

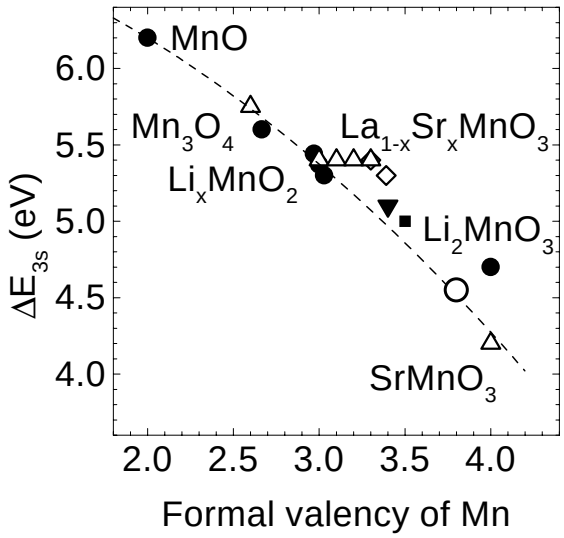

Figure 3.4: The Mn $3s$ exchange splitting versus the Mn formal valence; ♢ $La_{0.9}MnO_3$, $(La_{0.9}Sr_{0.1})_{0.9}MnO_3$; ▼ $La_{1.2}Sr_{1.8}Mn_2O_7$; ■ $Pm_{0.5}Sr_{0.5}MnO_3$; ○ $LiMnO_{2.4}$.

The question: where do the holes/electrons reside when substitutions are made? has been solved for several TM oxides. For the early TM (Ti, V) oxides it has been shown that the extra electrons/holes induced by doping have mainly $3d$ character, whereas in the late TM (as Ni) oxides the doping holes primarily reside at the oxygen sites. For the intermediate TM (as Fe, Mn) oxides the problem is more complicated and often the extra charges were found to be of mixed O $2p$ - TM $3d$ character [1, 92].

In the following we will try to answer this question by using the XPS Mn $3s$ spectra. When La is substituted by Sr in $La_{1-x}Sr_xMnO_3$, the doped holes may be localized either in (a) the Mn $3d$ or (b) O $2p$ states.

If the first situation occurs (a), each line in the spectrum will be given by a sum of $3s^1d^4$ and $3s^1d^3$ configurations. There are different energies for the two configurations and also different exchange splitting values because ΔE_s is proportional to the total $3d$ occupancy.

If the doping holes are localized at the O sites (b), the spectrum corresponds to the $3s^1d^4$ and $3s^1d^4\underline{L}$ configurations, where $\underline{L}$ denotes the O $2p^5$ state (one electron was transferred from the ligand $2p$ to transition metal $3d$ states). These

configurations correspond to different energies, but to the same exchange splitting, since there is the same occupancy of the d states in both cases (d^4).

From the spectra presented in Fig. 3.2, one can observe the same splitting of the Mn $3s$ levels, while the widths of the lines increase with x. Both observations suggest that the second case (b) is realized. Therefore, we conclude that the same value of the Mn $3s$ exchange splitting in the investigated single crystals, $(La_{0.9}Sr_{0.1})_{0.9}MnO_3$, $La_{1-x}Sr_xMnO_3$ ($x = 0.2; 0.3$) indicates that for $x < 0.3$ the doped holes are mainly localized in the O $2p$ states. A similar result was obtained by X–ray absorption spectroscopy [81].

The Mn $2p$ spectra of $La_{1-x}Sr_xMnO_3$ are presented in Fig. 3.5. The spin–orbit doublet peaks are located at $\sim$ 642 eV and $\sim$ 654 eV, respectively. For all investigated samples, single– and poly–crystals, the Mn $2p$ spectra exhibit satellites, at about 665 eV. The energy difference between the Mn $2p_{3/2}$ and Mn $2p_{1/2}$ is almost the same as the energy difference between the main line and satellite, in consequence the satellite that accompanies the $2p_{3/2}$ main line is obscured by the $2p_{1/2}$ main line. Such structures indicate that the Mn $3d$ states are strongly hybridized with the O $2p$ states [146], as we also conclude from a detailed analysis of the XPS valence band and XES spectra (see Section 3.1.2). Cluster–model calculations have revealed that for $LaMnO_3$ the main lines are due to $\underline{c}d^5\underline{L}$, whereas the satellites arise largely from $\underline{c}d^4$ and $\underline{c}d^6\underline{L}^2$ states (here $\underline{c}$ denotes a hole in the Mn $2p$ states, namely $2p^5$) [146]. For polycrystalline samples, similar Mn $2p$ XPS spectra were previously reported [152, 147, 97].

3.1.2 XPS valence band spectra

In Fig. 3.6 we present the XPS valence band and Mn $L\alpha$ and O $K\alpha$ XES spectra of $La_{1-x}Sr_xMnO_3$ ($x = 0.0; 0.2$). The valence band spectra consist of a wide band with two peaks and a low–intensity feature close to the Fermi level. The highest peak, located at $\sim$ 6 eV does not change with x. For the second peak of the wide band, at $\sim 3 \div 4$ eV, there is a slight shift to lower binding energies when x increases. The intensity of the low–intensity feature decreases with x, indicating that these states arise from Mn e_g, which are unoccupied for Mn^{4+} ($3d^3$) and occupied with one electron for Mn^{3+} ($3d^4$).

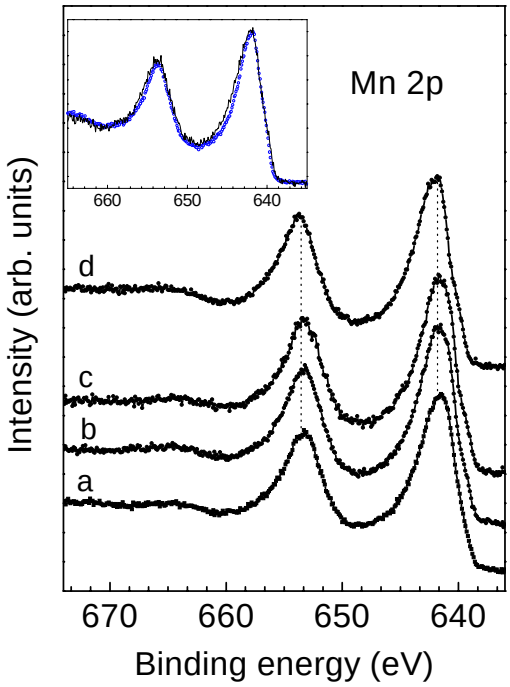

Figure 3.5: XPS Mn $2p$ spectra for: (a) $La_{0.6}Sr_{0.4}MnO_3$, (b) $La_{0.64}Sr_{0.2}MnO_3$, (c) $La_{0.56}Sr_{0.2}MnO_3$ polycrystals and (d) $(La_{0.9}Sr_{0.1})_{0.9}MnO_3$ single crystal; in inset: comparison of the Mn $2p$ XPS spectra for the single crystals $La_{1-x}Sr_xMnO_3$ ($x = 0.1$ ($\circ$) and 0.3 ($-$)).

In order to determine the partial Mn $3d$ and O $2p$ contribution to the valence band, we compare the XPS spectra with the Mn $L\alpha$ and O $K\alpha$ XES spectra. There is a superposition of the O $2p$ and Mn $3d$ states over the whole valence band, which point out the strong hybridization of these states. The experimental results are in good agreement with band structure calculations reported for both, end members of the $La_{1-x}Sr_xMnO_3$ series [146] and intermediate regime [90]. To illustrate this, in the same figure (Fig. 3.6) the LMTO band structure calculations for $x = 0.25$ from [90] are shown.

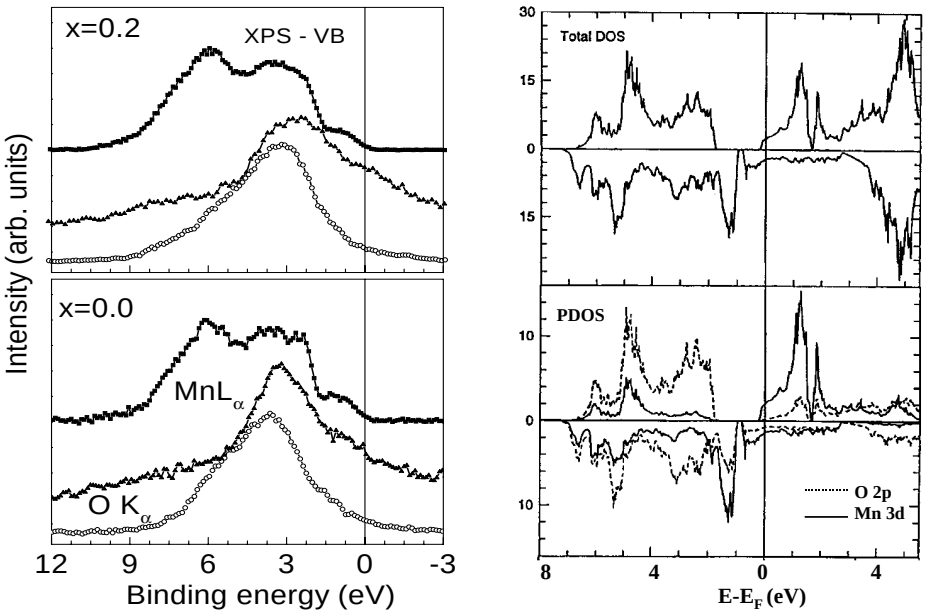

Figure 3.6: (left): XPS valence band and XES Mn $L\alpha$ and O $K\alpha$ spectra of $La_{1-x}Sr_xMnO_3$ ($x = 0.0; 0.2$); (right): Spin decomposed total density of states (up) and the partial contributions of the Mn and O atoms (down) [90].

3.2 Ba–doped manganese perovskites

The crystal structure of $La_{1-x}Ba_xMnO_3$ changes from orthorhombic through rhombohedral ($x > 0.13$) to cubic ($x > 0.35$) with increasing barium concentration [36, 80]. Studies of the magnetic, magnetotransport and optical properties of the polycrystalline samples of $La_{0.67}Ba_{0.33}MnO_3$ have shown that there is a change in the type of conductivity at $T = 333K$ [18, 17]. Very few spectroscopic studies on the Ba–doped manganese perovskites–single crystals are available up to now.

We present here a spectroscopic study of several Ba–doped $LaMnO_3$ single crystals $(La_{0.8}Ba_{0.2})_{0.93}MnO_3$, $La_{0.55}Ba_{0.3}Eu_{0.15}MnO_3$ and $La_{1-x}Ba_xMnO_3$ polycrystals ($x = 0.2 \div 0.55$). The valence band XPS spectra are discussed in relation with available band structure calculations. The XPS core level Mn $2p$ spectra are also studied. New XPS results of $La_{1-x}Ba_xMn_{1-y}Ni(Co)_yO_3$, single crystals, are presented.

3.2.1 XPS valence band spectra

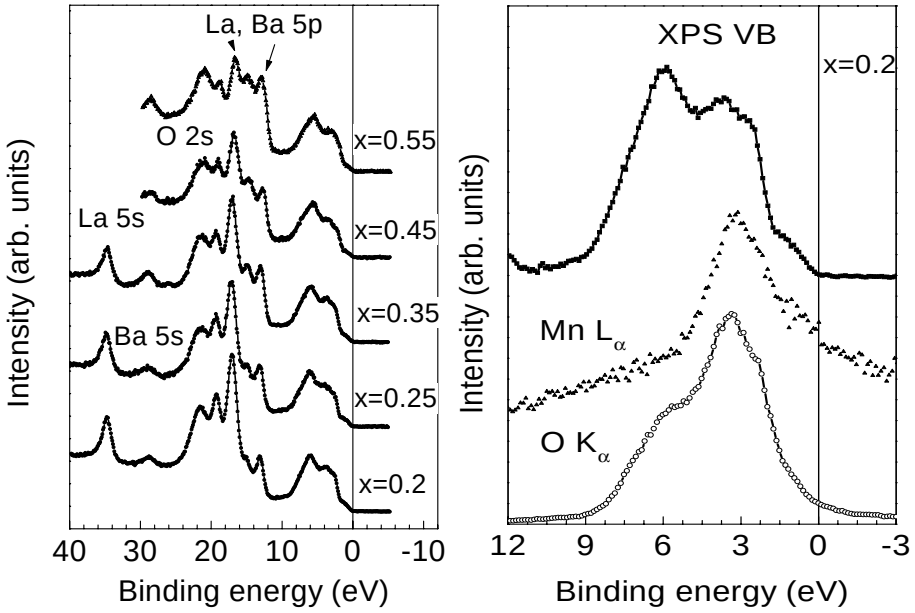

Figure 3.7: (left): XPS valence band spectra of $La_{1-x}Ba_xMnO_3$ (right): comparison of the XPS valence band, XES Mn Lα and O Kα spectra of $La_{0.8}Ba_{0.2}MnO_3$.

The valence band XPS spectra of the $La_{1-x}Ba_xMnO_3$ ($x = 0.2 \div 0.55$) polycrystals are shown in Fig. 3.7. The La $5p$ peaks are situated at $\sim$ 16.9 eV and $\sim$ 19 eV below Fermi level. Their intensity decrease when the Ba content (x) increases, as expected. The binding energy for the O $2s$ states is 21.5 eV. The valence band spectra have similar structures for all investigated Ba–doped sample: a large band that corresponds to the Mn $3d$ and O $2p$ hybridized states and a well pronounced peak just below Fermi level. To determine the partial contributions of differents atoms in the valence band we use, as previously, the XES Mn Lα and O Kα spectra and compare them with the valence band XPS spectra (see Fig. 3.7). For this, the Mn Lα and O Kα XES spectra were brought to the binding energy scale using the E_B values of the corresponding core levels (Mn $2p$ and O $1s$), as determined by XPS.

Additionally, we compare our experimental data with theoretical band structure calculations taken from Ref. [198]. The Mn Lα and O Kα spectra overlap over the whole valence band region, which emphasizes the strong hybridization

between the Mn $3d$ and O $2p$ states. According to [153] the peak at about 3 eV mainly arises from Mn t_{2g} states. The same result was experimentally obtained by using resonant photoemission technique [187]. The density of states at E_F consists of mainly e_g electrons of Mn d orbitals [198, 68]. Indeed, in Fig. 3.7 one can observe that the Fermi level passes through the e_g states, which are reflected in a well pronounced XPS peak. For $x > 0.33$, in the half–metallic regime, the LMTO band structure calculations showed that the contribution to DOS at the Fermi level comes solely from e_g electrons (see Fig. 3.8) [198].

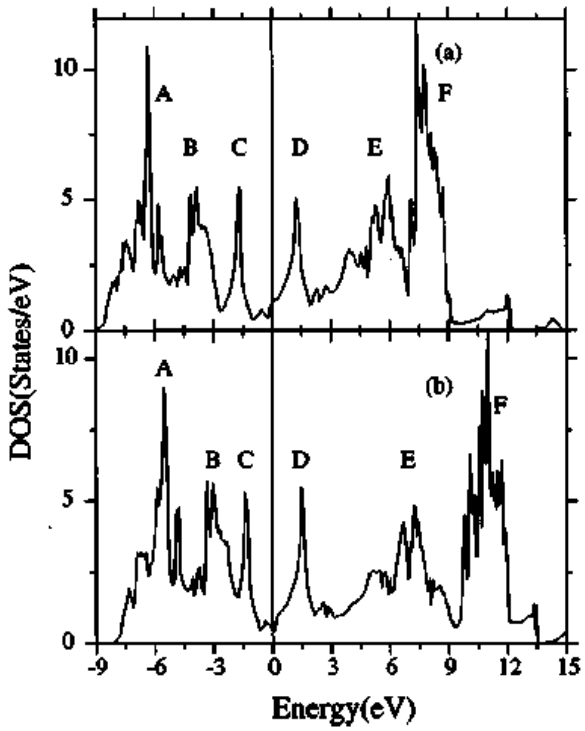

Figure 3.8: Total density of states for $La_{1-x}Ba_xMnO_3$: (a) $x = 0.2$ and (b) $x = 0.4$ ([198]).

In Fig. 3.9 the valence band spectra for the single crystals $(La_{0.8}Ba_{0.2})_{0.93}MnO_3$ and $La_{0.55}Ba_{0.3}Eu_{0.15}MnO_3$ are shown. We have compared the two VB spectra corresponding to $x = 0.45$, namely the spectrum of $La_{0.55}Ba_{0.3}Eu_{0.15}MnO_3$–single crystal and the spectrum of $La_{0.55}Ba_{0.45}MnO_3$–polycrystal. A slight shift of the highest structure in the valence band spectrum of the Eu–doped compound was

detected. Additionally, an enhancement of the states at $6 \div 10$ eV occurs. The explanation cannot be given by considering strong differences in the VB spectra of single crystalline and polycrystalline samples, since for $x = 0.2$ no significant changes were detected between poly– and single–crystal spectra (see Figs. 3.9 and 3.7). Theoretical calculations are required to explain this behaviour, which seems to be connected with O $2p$ hybridized with Eu $4f$ states [100].

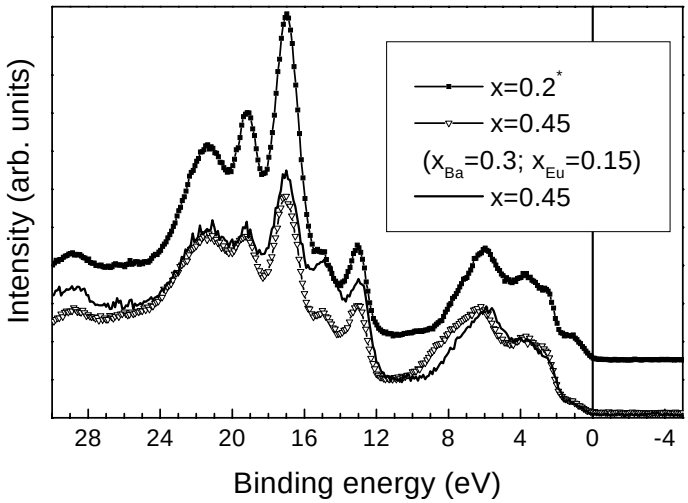

Figure 3.9: XPS valence band spectra of the single crystals $(La_{0.8}Ba_{0.2})_{0.93}MnO_3$ and $La_{0.55}Ba_{0.3}Eu_{0.15}MnO_3$; for comparison the valence band spectrum of $La_{0.55}Ba_{0.45}MnO_3$ is given.

3.2.2 XPS core level spectra

The Mn $2p$ spectra of $La_{1-x}Ba_xMnO_3$ are presented in Fig. 3.10. As in case of Sr–doped manganese perovskites, the Mn $2p_{3/2}$ and Mn $2p_{1/2}$ levels situated at $641.5 \div 642$ eV and $653.5 \div 654$ eV, are not very much mofidied with increasing x. However, a very slight shift to higher binding energies with increasing x is observed, suggesting a charge redistribution from Mn^{3+} to Mn^{4+} during the Ba doping. Unfortunately, in the case of $La_{1-x}Ba_xMnO_3$ the Mn $3s$ XPS spectra can not be used to determine the $3d$ occupancy, because the Mn $3s$ emission overlaps the with Ba $4d$ contribution.

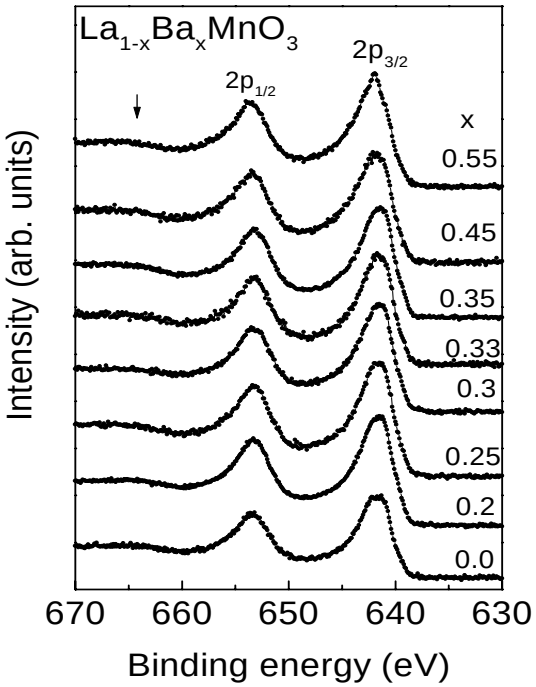

Figure 3.10: XPS Mn $2p$ spectra for $La_{1-x}Ba_xMnO_3$.

3.2.3 $La_{1-x}Ba_xMn_{1-y}Ni(Co)_yO_3$

Although the crystallographic and magnetic properties of Mn–site doped perovskites, as $LaMn_{1-y}TM_yO_3$, were studied in the 60's, CMR effect in these compounds was firstly mentioned very recently [148, 196]. Structural, magnetic and magnetotransport studies of $La_{0.825}Sr_{0.175}Mn_{1-x}Cu_xO_3$, $La_{0.7}Pb_{0.3}Mn_{0.9}TM_{0.1}O_3$ $(TM = Fe, Co, Ni)$ [206, 65], $La_{2/3}Ca_{1/3}Mn_{1-x}A_xO_3$ $(A = Co, Cr; x < 0.1)$ [144], $La_{(1+x)/3}Ba_{(2-x)/3}Cu_{1-x}Mn_xO_3$ $(0.7 < x < 1)$ [199], $La_{0.67}Sr_{0.33}Mn_{1-x}Ni_xO_3$ $(x < 0.2)$ [188] were reported during the last few months.

There is an actual area of interest in science to determine the role of different dopants on the electronic structure of such compounds, in order to understand their interesting behaviour and the mechanism of CMR effect. For $La_{0.7}Ca_{0.3}Mn_{1-x}Me_xO_3$ (Me=Al, Ge) a reduction of the magnetic transition temperature when the Mn ions are replaced by other $3d$ ions has been reported [58], which cannot be attributed to the changes in the ion sizes. These additions were found to destroy the long–range ferromagnetic order. By contrast, ferromagnetic

properties as well as large magnetoresistance in $La_{0.7}Ba_{0.3}Mn_{0.85}Nb_{0.15}O_3$ were reported [175].

Further, we present new XPS results of $La_{1-x}Ba_xMn_{1-y}Ni(Co)_yO_3$, single crystals[2]. Valence band and core level spectra are analyzed. The magnetic properties of the investigated single crystals $La_{1-x}Ba_xMn_{1-y}Co_yO_3$ were reported and the phase transition was associated with change in the ground state of Co^{2+} ions [176]. For $0.16 < x < 0.22$ there is a strong enhancement of magnetization at $T_t = 180$ K. The transition temperature appears to be unmodified by the Co content. A sharp magnetoresistance maximum was found at temperatures close to T_C for all investigated samples (Fig 3.11).

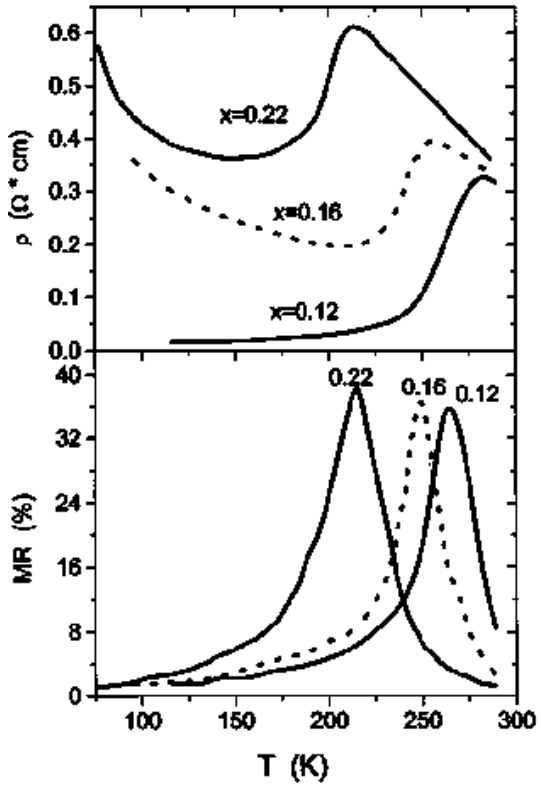

Figure 3.11: Temperature dependences of the resistivity and magnetoresistance (H=9 kOe) of the single crystals $La_{0.76}Ba_{0.24}Mn_{1-x}Co_xO_3$ [176].

In Fig. 3.12 and 3.13 the XPS valence band spectra of the single crystals

[2]Prof. I. O. Troyanchuk is acknowledged for providing single crystal samples.

$La_{1-x}Ba_xMn_{1-y}Ni(Co)_yO_3$ are presented.

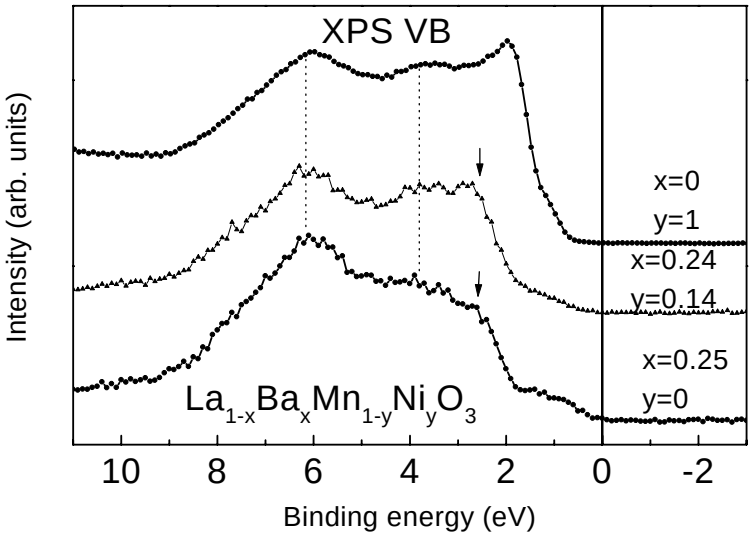

Figure 3.12: XPS valence band spectra of $La_{1-x}Ba_xMn_{1-y}Ni_yO_3$ (single crystals).

We use the valence band XPS spectrum for $La_{0.75}Ba_{0.25}MnO_3$, discussed above, as reference compound for the investigated $La_{0.76}Ba_{0.24}Mn_{0.86}Ni_{0.14}O_3$ single crystal (see Fig. 3.12). The two valence band spectra exhibit similar features, a broad band with double structure and a low intensity peak close to the Fermi level. However the intensity of the small peak is lower for the Ni–doped sample, suggesting smaller occupancy of the e_g states. The first peak of the broad band is much increased for the Ni–doped compound, indicating that it arises from Ni $3d$ states. Indeed, the band structure calculations of $LaNiO_3$ showed that the Ni $3d$ contributes to the density of states over the whole VB region (pointing out strong hybridization with O $2p$ states), but with the highest contribution at low binding energies [150, 111]. The same conclusion is obtained, if one compares the VB spectrum of $La_{0.76}Ba_{0.24}Mn_{0.86}Ni_{0.14}O_3$ with the VB spectrum of another reference compound, $LaNiO_3$. The Ni $3d$ contributes to the density of states at lower binding energies, in comparison with Mn $3d$. Additional XES measurements and/or band structure calculations could give an answer to the electronic structure of this double–doped compound.

In Fig. 3.13 we present the valence band spectrum of $La_{0.78}Ba_{0.22}Mn_{0.84}Co_{0.16}O_3$ and for comparison we use the spectrum of $(La_{0.8}Ba_{0.2})_{0.93}MnO_3$ (that is identical

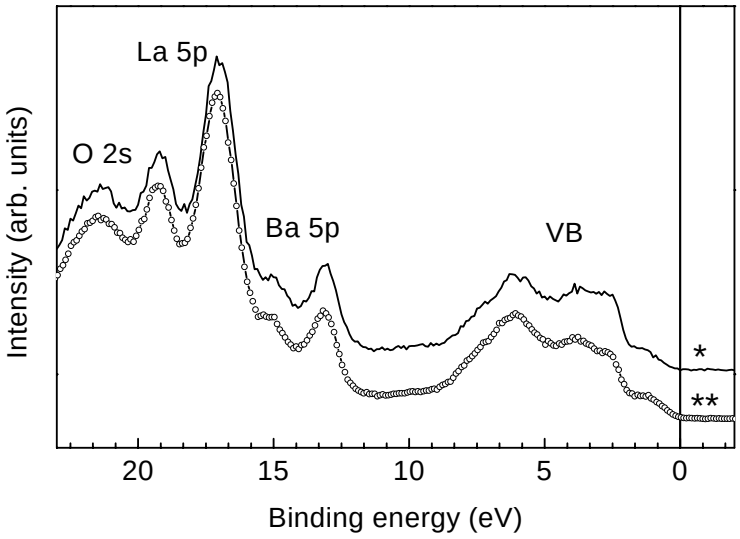

Figure 3.13: XPS valence band spectra of the single crystals $La_{0.78}Ba_{0.22}Mn_{0.84}$-$Co_{0.16}O_3$ (*) and $(La_{0.8}Ba_{0.2})_{0.93}MnO_3$ (**).

with the VB of $La_{0.75}Ba_{0.25}Mn_{1-y}O_3$, polycrystal shown in Fig. 3.12). Also in this case, an increase of the intensity at about $2.5 \div 4$ eV for the VB of Co–doped sample can be easily observed. The intensity of the small peak close to Fermi level slightly decreases when the Co content increases to 22%. This suggests a lower occupancy of the e_g states. The study of $LaCoO_3$ showed that there is a strong hybridization between Co $3d$ and O $2p$ states over the whole VB, with the main contribution of Co $3d$ just below the Fermi level [148].

The study of $LaMn_{1-x}Co_xO_3$ by X–ray absorption and resonant photoemission spectroscopy showed the divalent character of the Co ions [132]. In Ref. [196] it was found that, for $LaMn_{1-x}Co_xO_3$, the Co ions do not lie in the low–spin state, as in $LaCoO_3$ ($3d^6$), but they have non–zero magnetic moments. To get information about the Co valence state, we have used the Co $2p$ XPS spectra (see Fig. 3.14). Because in the same binding energy region there is Co $2p$ and La $3d$ photoelectron emission, we have obtained the Co contribution as follows: the La $3d$ spectrum of $La_{0.75}Ba_{0.25}MnO_3$ was extracted from the XPS spectrum of $La_{0.78}Ba_{0.22}Mn_{0.84}Co_{0.16}O_3$. Although the Ba concentration in the two samples is not identical (25 % and 22 %, respectively), we consider that the obtained 'difference spectrum' contains mainly information from the Co $2p$ states. With

this assumption, we compare the 'difference spectrum' with the Co $2p$ spectrum of $LiCoO_2$ (Co^{3+}) and CoO (Co^{2+}) (see Fig. 3.14). The spectral Co $2p$ features for Co^{2+} and Co^{3+} compounds are completely different, namely the distance between the main line and satellite is much larger for $LiCoO_2$ and the intensity ratio main line/satellite is much higher for CoO, as compared to $LiCoO_2$.

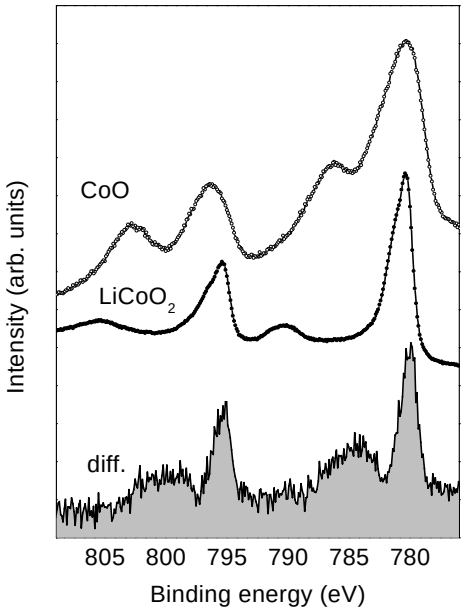

Figure 3.14: XPS Co $2p$ spectra of CoO, $LiCoO_2$ together with the 'difference' spectrum obtained by substraction of the La $3d$ spectrum of $La_{0.75}Ba_{0.25}MnO_3$ from the 'La $3d$ + Co $2p$' spectrum of $La_{0.78}Ba_{0.22}Mn_{0.84}Co_{0.16}O_3$.

The 'difference' spectrum has a structure similar to the Co $2p$ spectrum for CoO. This suggests that in $La_{0.78}Ba_{0.22}Mn_{0.84}Co_{0.16}O_3$, Co has bivalent character. Unfortunately, Co $3s$ and Mn $3s$ XPS spectra can not be used to extract information about the electronic configurations of the Co and Mn ions, because the corresponding XPS spectra are obscured by the stronger Ba $4d$ and La $4d$ states.

Additional experimental studies and band structure calculations are required in order to get more information about the electronic structure of the double doped $La_{1-x}Ba_xMn_{1-y}Co_yO_3$ system.

3.3 Ca– and Pb–doped manganese perovskites

The end members of the $La_{1-x}Ca_xMnO_3$ series are antiferromagnetic insulators and they have different crystal structures and magnetic symmetries. The antiferromagnetic structure of $LaMnO_3$ is of A–type (T_N=140 K), whereas $CaMnO_3$ has an G–type AF structure with T_N=120 K [195, 47]. The $La_{1-x}Ca_xMnO_3$ system becomes a ferromagnetic metal for $0.2 < x < 0.5$. Large magnetoresistance was reported for the $La_{0.65}Ca_{0.35}MnO_3$ single crystals (300 %) and higher values were found for thin films of similar composition [102].

The electronic structure of $La_{1-x}Ca_xMnO_3$ was intensively studied in the last few years [135, 131, 202, 180]. Several reviews treat this subject in detail, in relation to various CMR and metal–insulator transitition (MIT) mechanisms [33, 170, 141]. The metal–insulator transition in these CMR materials was related by some authors to an Anderson localization transition, whereas others proposed that there is most likely a finite temperature crossover phenomenon [165].

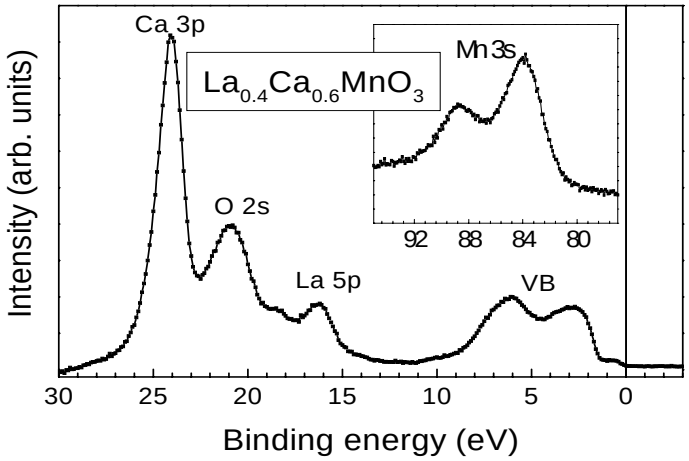

Figure 3.15: XPS valence band spectrum of $La_{0.4}Ca_{0.6}MnO_3$; inset: Mn $3s$ splitting for the same compound.

In Fig. 3.15 the valence band spectrum of $La_{0.2}Ca_{0.8}MnO_3$ [3] is presented in an energy range from -3 to 30 eV, including the Ca $3p$, O $2s$ and La $5p$ peaks. The valence band consists of a wide two–peaks structure and a low intensity feature close to the Fermi level. Using the LMTO band structure calculation

[3]Prof. E. Burzo is acknowledged for providing the polycrystalline sample.

results [205], we assign the small feature at E_F to the Mn e_g band and the first peak of the broad structure at ~ 2.7 eV to the Mn t_{2g} states. Moreover, by using resonance photoemission spectroscopy, an enhancement of the states around 4 eV was determined [114], showing their dominant Mn $3d$ nature. The second peak at ~ 6 eV has mainly O $2p$ character. The asymmetric part of this peak, at higher binding energy, is associated with Mn t_{2g}–O $2p$ hybridized states [153]. In the inset of the same figure, a well resolved splitting of the Mn $3s$ states can be observed. The value of the splitting (5.0 eV) corresponds to a mixed–valent Mn^{3+}/Mn^{4+} system. The large value of the Mn $3s$ splitting suggests a high spin configuration of the Mn^{3+} ions, in agreement with neutron diffraction data [195].

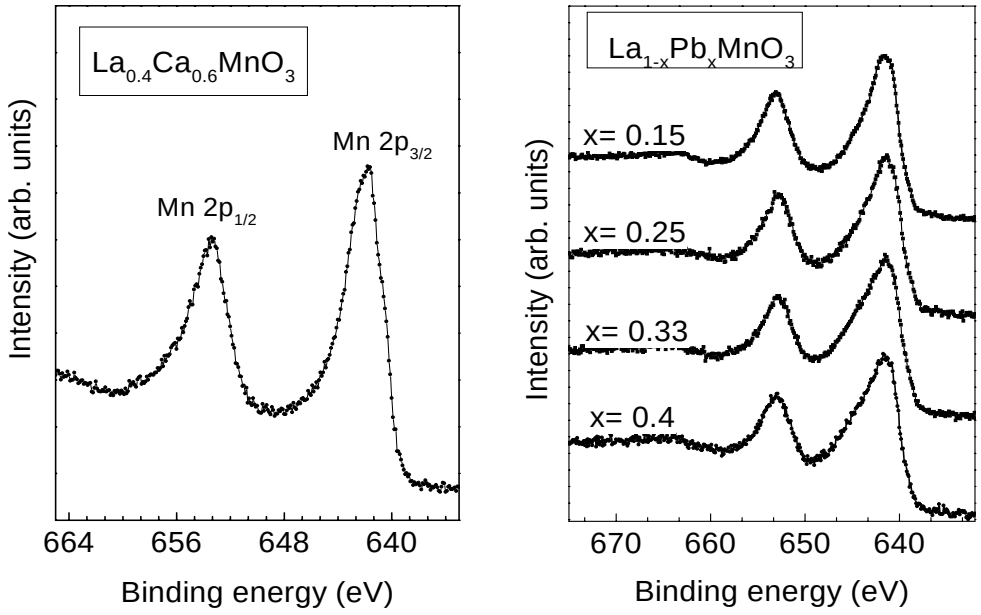

Figure 3.16: XPS Mn 2p spectra of $La_{0.4}Ca_{0.6}MnO_3$ and $La_{1-x}Pb_xMnO_3$.

The Mn $2p$ spectrum of $La_{0.4}Ca_{0.6}MnO_3$ shown in Fig. 3.16 consists of broad $2p_{3/2}$ and $2p_{1/2}$ peaks, supporting the idea of mixed–valency. The Mn K_β emission results for $La_{1-x}Ca_xMnO_3$, which provide a direct method to probe the total Mn $3d$ spin and the effective charge density on the Mn sites, are consistent with a mixed–valent Mn^{3+}/Mn^{4+} [180]. The Mn $2p$ spectra of $La_{1-x}Pb_xMnO_3$ for x=0.15, 0.25, 0.33 and 0.4, are shown in the same figure. The width of the Mn $2p_{3/2}$ peak increases with x, as expected from the increasing of the Mn^{4+} amount

with doping.

In this chapter we have presented XPS and XES results of manganese perovskites, $La_{1-x}A_xMnO_3$, the first reported CMR compounds.

The role of the La–substitutions by Sr, Ba, Ca and Pb was discussed and the influence of the dopants on the electronic structure has been determined. By comparing the XPS and XES data we could localize the Mn $3d$ and O $2p$ states in the valence band; for all investigated samples, a strong hybridization of the metal $3d$ and ligand $2p$ states was found, in good agreement with the band structure calculations.

For the Sr–doped samples, we found no changes in the Mn $3s$ splitting for $x < 0.3$, which suggest that the doping holes have mainly O $2p$ character. The new experimental results on single crystals materials were discussed in relation to the previously reported data.

Very recently, a high interest has appeared in La– and Mn–doped compounds. New XPS data for the $La_{1-x}Ba_xMn_{1-y}TM_yO_3$ (TM=Ni, Co) single crystals were discussed in relation to the band structure calculations available for related systems. The first XPS data of the single crystals $La_{1-x}Ba_xMn_{1-y}Co_yO_3$ suggest the bivalent character of the Co ions, in agreement with the magnetic data obtained for the same samples [176].

Chapter 4

Cr–based spinel chalcogenides

A remarkable interest in the magnetic chalcogenides has been renewed due to the *colossal magnetoresistance effect (CMR)* recently reported in the $Fe_{1-x}Cu_xCr_2S_4$ ferrimagnets close to room temperature [142]. Unlike the manganese perovskites (first reported CMR compounds), the ACr_2S_4 spinels are characterized by no mixed valence, an A–site cation that can contribute to electronic states near the Fermi level and large deviations of the metal–anion–metal bond angle from 180°. Therefore, other mechanisms, besides the double–exchange and electron–phonon interactions, should be responsible for the CMR effect observed not only in $Fe_{1-x}Cu_xCr_2S_4$, but also in other classes of materials (pyrochlores $Tl_2Mn_2O_7$ [155], $Sr_{2-x}Nd_{1+x}Mn_2O_7$ [16], double–layered systems $La_{2-2x}Sr(Ca, Sn)_{1+2x}Mn_2O_7$ [121, 37, 10], $Eu_{14}MnBi_{11}$ [30]).

In the following section a comprehensive study of the $Fe_{1-x}Cu_xCr_2S(Se)_4$ spinel system is presented. A special attention has been paid to the $CuCr_2Se_4$ system, where the Cu valence is still a matter of controversy. Two models developed by Lotgering [106, 107] and Goodenough [62] suggest both monovalent and divalent character of the Cu ions. Using the Cu $3s$ and $2p$ core level XPS spectra, we suggest that in $Fe_{0.5}Cu_{0.5}Cr_2S_4$ the Cu ions have the $3d^{10}$ electronic configuration [178], which is in agreement with the first model.

Several other spinel chalcogenides $ACr_2S(Se)_4$ (A= Fe, Mn, Zn, Cd, Hg) have been investigated by X–ray photoelectron spectroscopy. From the observed splitting of the Cr, Fe and Mn $3s$ core levels the electronic configurations of the corresponding ions were determined. A well resolved splitting of the Cr $2p$ core

levels in the investigated crystals was found [179].

- Experimental aspects

Single crystals of $FeCr_2S_4$, $Fe_{0.5}Cu_{0.5}Cr_2S_4$ and $CuCr_2Se_4$ have been grown by chemical transport reaction[1]. The Fe Lα, Cr Lα, and Cu Lα X–ray emission spectra ($3d4s \rightarrow 2p_{3/2}$ transitions) were obtained by electron excitation and measured with the aid of a RSM 500–type X–ray vacuum spectrometer. The S Kβ_1 X–ray emission spectra ($3p \rightarrow 1s$ transitions) were measured by using a fluorescent Johan–type vacuum spectrometer equipped with a position–sensitive detector [45]. The S $L_{2,3}$ X–ray emission spectra ($3s, 3d \rightarrow 2p$ transitions) were recorded with an ultrasoft X–ray spectrometer having a high energy resolution using electron excitation [94].

4.1 Electronic structure of $Fe_{1-x}Cu_xCr_2S(Se)_4$

This section is structured in two parts. In the first part the changes induced in the electronic structure of $FeCr_2S_4$ by the Cu–doping are analyzed by using the X–ray photoelectron and X–ray emission spectroscopies. The experimental results are discussed in relation to the LMTO band structure calculations. The second part is dedicated to the $CuCr_2Se_4$ system.

4.1.1 $Fe_{1-x}Cu_xCr_2S_4$ (x=0.0, 0.5)

The $FeCr_2S_4$ and $CuCr_2S_4$ compounds form a series of solid solutions and their electrical and magnetic properties were extensively studied since early $1970s$ [106]. Both compounds crystallize in the normal spinel close–packed fcc lattice [$Fd\overline{3}m$], in which the chromium ions occupy octahedral sites, the iron and copper ions tetrahedral sites, respectively (Fig. 4.1).

$FeCr_2S_4$ and $Fe_{0.5}Cu_{0.5}Cr_2S_4$ are p– and n–type semiconducting ferrimagnets [103, 104, 67, 107], whereas $CuCr_2S_4$ and $CuCr_2Se_4$ are ferromagnetic metals with the Curie temperatures of 425 K and 460 K, respectively [105].

[1]Dr. V. Tsurcan is acknowledged for providing the single crystals.

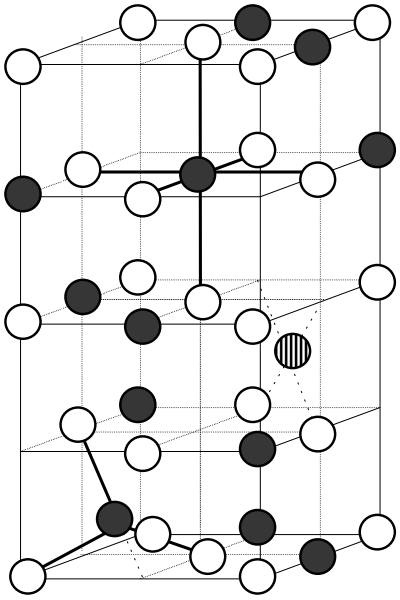

Figure 4.1: The spinel (AB_2X_4) crystal structure: the A, B and X ions are represented as striated, filled and empty spheres, respectively.

The ferrimagnetic transition temperatures for the investigated compounds $FeCr_2S_4$ and $Fe_{0.5}Cu_{0.5}Cr_2S_4$ (single crystals) were determined by measuring the magnetization at low magnetic fields (Fig. 4.2) [95]. Values of 168 K and 348 K were found, which are in agreement with previously reported data [142, 128].

In $FeCr_2S_4$ the Fe^{2+} and Cr^{3+} ions have $3d^6$ and $3d^3$ electronic configurations, respectively. For the $CuCr_2S(Se)_4$ system the question of the Cu valence state has been a long-standing problem. In connection with this, two models were proposed by Lotgering [106, 107] and Goodenough [62]. The first model claimed that the Cu valence state should be monovalent (Cu^{1+}), whereas the second one claimed that Cu is divalent (Cu^{2+}). For the $Fe_{0.5}Cu_{0.5}Cr_2S_4$ system the situation becomes even more complicated, since several possibilities can occur for the substitution of Cu for Fe, depending on whether Cu is present as Cu^{1+} or Cu^{2+} and various possibilities were discussed by several authors [107, 67, 134].

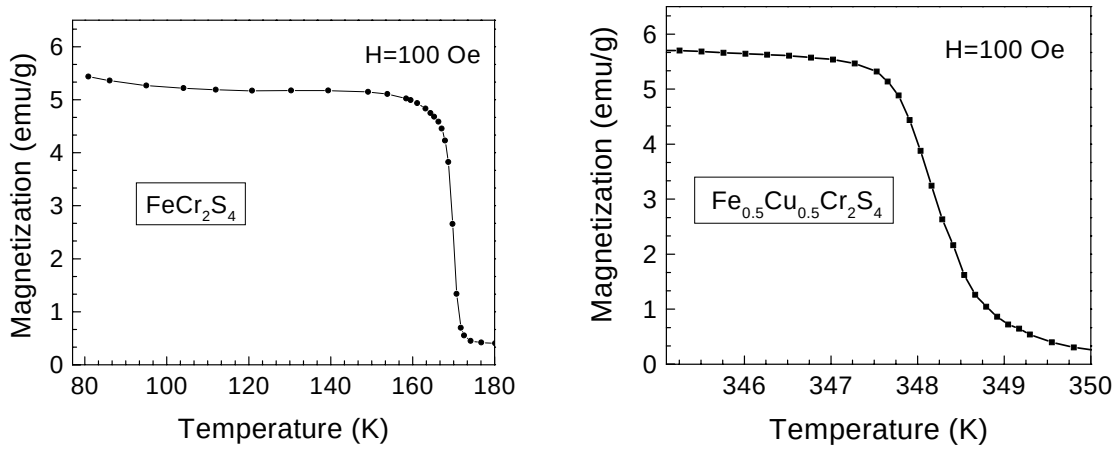

Figure 4.2: Magnetization versus temperature for the single crystals $FeCr_2S_4$ and $Fe_{0.5}Cu_{0.5}Cr_2S_4$.

4.1.1.1 Cu $2p$ and $3s$, Fe $2p$, Cr $2p$ and $3s$ and S $2p$ core level spectra

In this section the Cu $2p$ and $3s$, Fe $2p$, Cr $2p$ and $3s$, and S $2p$ core level spectra of the $Fe_{1-x}Cu_xCr_2S_4$ (x= 0.0, 0.5) single crystals are presented and the electronic configurations of the constituent ions are determined.

The Cu $2p$ XPS spectrum of $Fe_{0.5}Cu_{0.5}Cr_2S_4$ presented in Fig. 4.3 exhibits a doublet structure due to the spin–orbit coupling. This spectrum closely resembles the Cu $2p$ XPS spectra of the Cu_2O and $CuFeO_2$ [56] compounds, in which the Cu ions are present as Cu^{1+}. The only difference is around $955 - 960$ eV, where a small shoulder arises from the Cr LMM Auger states. In the same figure the Cu $2p$ spectrum for CuO (Cu^{2+}) is also presented. A characteristic feature of the Cu $2p$ XPS spectra in the Cu^{2+} oxides is the presence of an intense high–energy satellite structure [168, 70, 203]. The satellite lines in the Cu $2p$ spectrum of CuO correspond to the $2p^{-1}3d^9L$ final states, whereas the main lines ($E_B(2p_{3/2})$= 933.3 eV and $E_B(2p_{31/2})$= 953.2 eV) are associated with the $2p^{-1}\ 3d^{10}\ L^{-1}$ states ($2p^{-1}$ and L^{-1} denote a hole on the Cu $2p$ level after the XPS process and a hole on the ligand atom after the charge–transfer process, respectively). The Cu $2p$ spectrum of $Fe_{0.5}Cu_{0.5}Cr_2S_4$ shows no such features suggesting the monovalent character of the Cu ions. However, although in the Cu oxides the presence/absence of the satellite structures in the Cu $2p$ XPS spectra is a strong indicator of the $3d^9/3d^{10}$

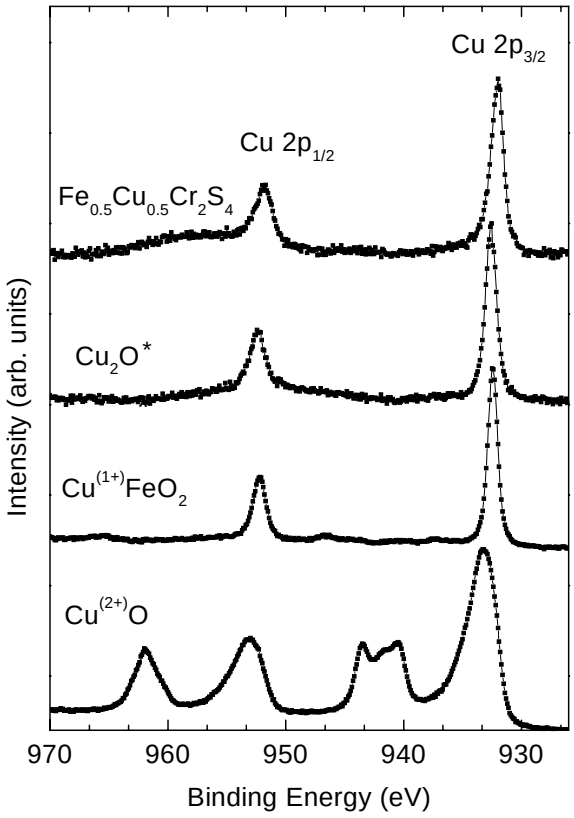

Figure 4.3: The XPS Cu $2p$ spectra for $Fe_{0.5}Cu_{0.5}Cr_2S_4$, Cu_2O, $CuFeO_2$ [56] and CuO.

electronic configurations (Cu^{2+}/Cu^{1+}), this is not always the case for other Cu compounds. For example, no shake–up satellite lines were observed in CuSe, CuS, Cu_2Se [145] and $Cu_xGa_yCr_zSe_4$ [194].

In order to check the Cu electronic configuration in this system, the Cu $3s$ XPS spectrum was measured (see Fig. 4.4). It is known that the spectral splitting of the $3s$ XPS core–level spectra of the transition metals (TM) originates from the exchange coupling between the $3s$ hole created in the photoemission process and the $3d$ electrons. The $3s$ splitting is related to the total spin of the $3d$ electrons [184] and therefore from its value one can obtain information on the

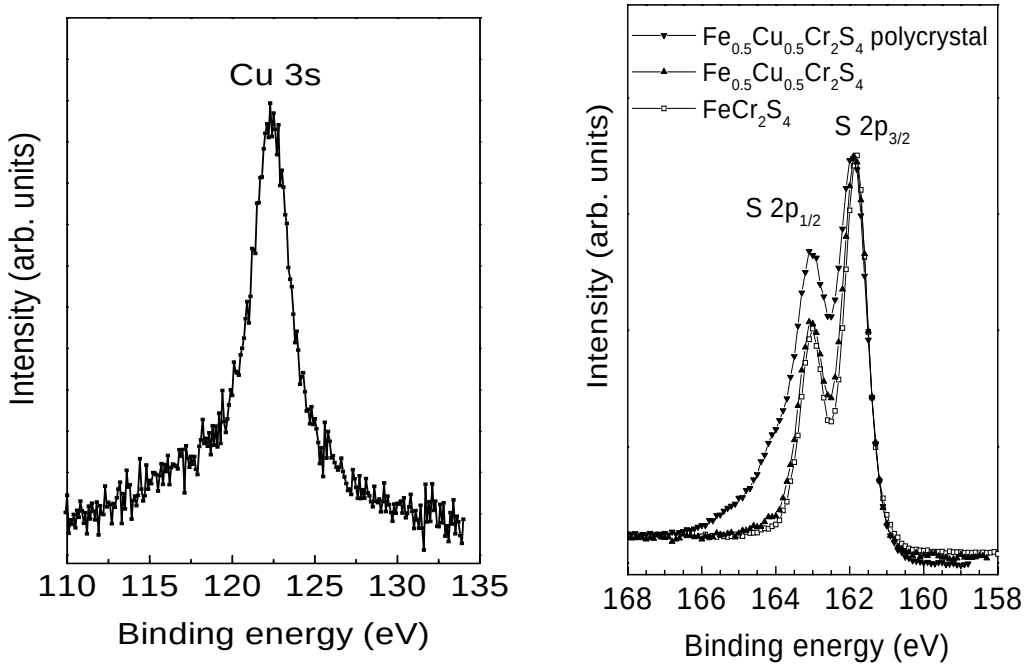

Figure 4.4: The XPS Cu 3s spectra of the single crystal $Fe_{0.5}Cu_{0.5}Cr_2S_4$ (left) and XPS S 2p spectra of $Fe_{1-x}Cu_xCr_2S_4$, x= 0.0, 0.5 (right).

TM electronic configuration. There is no exchange splitting of the Cu 3s level of $Fe_{0.5}Cu_{0.5}Cr_2S_4$, which indicates a $3d^{10}$ electronic configuration for the Cu^{1+} ions [178].

The S 2p spectrum of the $Fe_{0.5}Cu_{0.5}Cr_2S_4$ single crystal (see Fig. 4.4) looks very similar to the S 2p spectrum of the $FeCr_2S_4$ single crystal. For the $Fe_{0.5}Cu_{0.5}Cr_2S_4$ polycrystalline sample an additional weak S $2p_{3/2,1/2}$ doublet appears with an energetic position very close to FeS_2^- [96], and the corresponding spectrum exhibits a different shape. However, the spectrum of the $Fe_{0.5}Cu_{0.5}Cr_2S_4$ single crystal shows no additional S^- features due to the delocalized nature of the sulphur states.

Furthermore we have analyzed the Fe 2p XPS spectra of $Fe_{0.5}Cu_{0.5}Cr_2S_4$ and $FeCr_2S_4$ (see Fig. 4.5). For the $FeCr_2S_4$ single crystal, where Fe appears as Fe^{2+} ($3d^6$), the Fe 2p spectrum exhibits a doublet structure (Fe $2p_{3/2}$ and Fe $2p_{1/2}$) due to the spin–orbit coupling. Additionally, one can observe satellite structures very similar to $Fe^{2+}O$ [56], where the main lines and the satellites were identified

as reflecting the $2p^{-1}3d^7L^{-1}$ and $2p^{-1}3d^6$ final states [201].

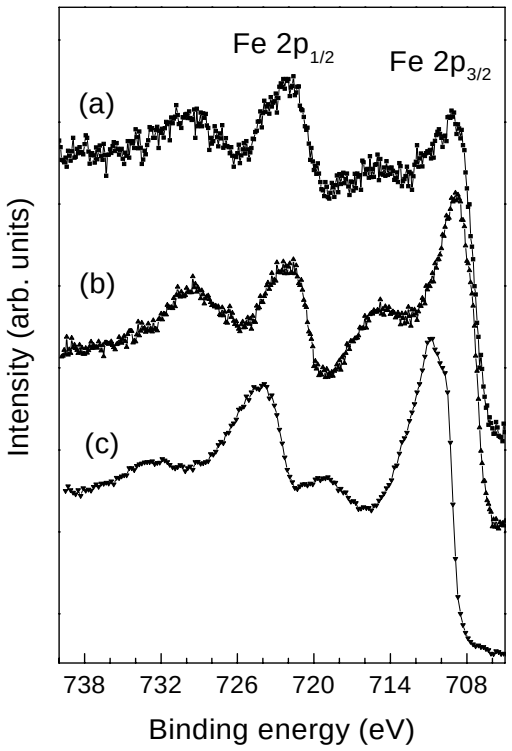

Figure 4.5: The XPS Fe $2p$ spectra of: (a) $Fe_{0.5}Cu_{0.5}Cr_2S_4$, (b) $FeCr_2S_4$ - single crystals and (c) Fe_2O_3 - reference compound.

The introduction of Cu^+ in the $FeCr_2S_4$ structure should lead to the appearance of the Fe^{3+} in the Fe $2p$ spectra. However, the Fe $2p$ spectra of the $Fe_{0.5}Cu_{0.5}Cr_2S_4$, poly– and single– crystals are similar to the Fe^{2+} $2p$ spectrum of $FeCr_2S_4$ (the same energetic positions and similar shapes). They appear to be broader than in the case of $FeCr_2S_4$ and the satellite structures are less pronounced. This is caused by the superposition of the Fe $2p$ XPS with Cu LMM Auger spectra.

For comparison, the Fe $2p$ spectrum of $Fe_2^{3+}O_3$ is presented in the same figure (Fig. 4.5). One can observe a different ratio of the main peak/satellite intensities and also a clear shift of the spectrum to higher binding energies. The same characteristics were found for other Fe^{3+} oxides: $CuFeO_2$ and $LiFeO_2$ [56]. In

this case the main lines are associated with the $2p^{-1}3d^6L^{-1}$ final states, whereas the satellites reflect the $2p^{-1}3d^5$ states.

The explanation for the similarities of the Fe $2p$ XPS spectra of $Fe_{0.5}Cu_{0.5}Cr_2S_4$ and $FeCr_2S_4$, although they correspond to different electronic configurations (Fe^{2+} and Fe^{3+}), is that during the photoemission process a charge transfer from the S^{2-} to Fe^{3+} ions takes place and therefore XPS measures excited $Fe^{2+}S^-$ states. However, in the ground state no significant charge transfer is found and magnetic measurements indeed showed the existence of the Fe^{3+} ions in $Fe_{0.5}Cu_{0.5}Cr_2S_4$ [130].

Let us now analyze the electronic configuration of the Cr ions by using the Cr $2p$ and $3s$ core level spectra (Fig. 4.6). In the Cr $2p$ spectrum, besides the spin–orbit splitting ($2p_{3/2}$, $2p_{1/2}$) there is also a well resolved splitting of the Cr $2p_{3/2}$ level, of about 1 eV. A detailed analysis of the observed structure will be given in the Section 4.2.1. The spectrum in the right panel of Fig. 4.6 consists of two regions: one derives from Cu $3p$ and Cr $3s$ states and the second, at higher binding energies, is given by the Fe $3s$ contributions. In order to obtain information on the Cr electronic configuration we followed the next procedure: the Cu $3p$ contribution has been extracted from the total spectrum by using the Cu $3p$ spectrum of $Cu^{1+}FeO_2$ measured with the same apparatus (shown in inset). Hence, the remaining spectrum only carries information about the Cr $3s$ states. The exchange splitting associated with the Cr $3s$ states is about 4 eV. This value corresponds to a $3d^3$ configuration of the Cr^{3+} ions [57]. This result is in good agreement with the neutron diffraction data on $Fe_{0.5}Cu_{0.5}Cr_2S_4$ polycrystals, where a value of $2.9\mu_B$ for the Cr magnetic moment was determined [130].

4.1.1.2 XPS valence band, Cr Lα, Cu Lα, Fe Lα, S Kβ and S $L_{2,3}$ XES spectra

In Fig. 4.7 the XPS valence band spectrum of $FeCr_2S_4$ (single crystal) is presented together with the Cr Lα, Fe Lα, S Kβ and S $L_{2,3}$ XES spectra. The VB spectrum consists of two bands. The first band exhibits a maximum around 4 eV, two distinct features at $\sim$ 1.5 eV and 6 eV and a clear step near the bottom of the valence band. The second band, at higher binding energies, derives from the S $3s$ states.

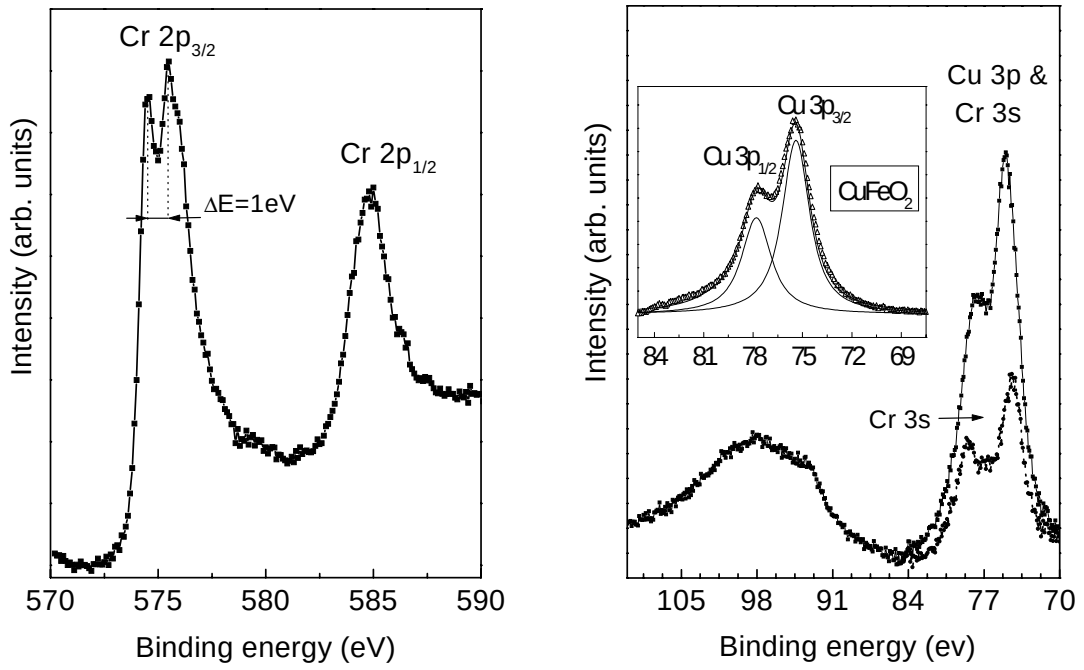

Figure 4.6: The XPS Cr $2p$ (left) and Cr $3s$ (right) spectra of the single crystal $Fe_{0.5}Cu_{0.5}Cr_2S_4$.

In order to find the partial contributions of the constituent ions (Fe, Cr, S) in the valence band, the Cr Lα, Fe Lα, S Kβ and S $L_{2,3}$ XES spectra were recorded. These spectra give information about the partial contributions of the Cr $3d$, Fe $3d$, S $3p$ and S $3s$ states to the valence band. The energy scales of the XES spectra relative to the Fermi level were calibrated using the binding energies of the relevant initial core–level states, as determined by XPS.

The features at $1-1.5$ eV, 4 eV, 6 eV and 13 eV in the VB spectrum correspond to the maxima of the Cr Lα, S Kβ, Fe Lα and S $L_{2,3}$ XES spectra. Therefore, we identify these states as Cr $3d$, S $3p$, Fe $3d$ and S $3s$. The energy difference between the S $3s$ and S $3p$ is ~ 9 eV, as observed in many other sulphur compounds [96, 108].

The same comparison between the VB–XPS and XES spectra was done for $Fe_{0.5}Cu_{0.5}Cr_2S_4$ and the results are presented in Fig 4.8. Also in this case, the valence band spectrum consists of two regions: a broad band close to the Fermi

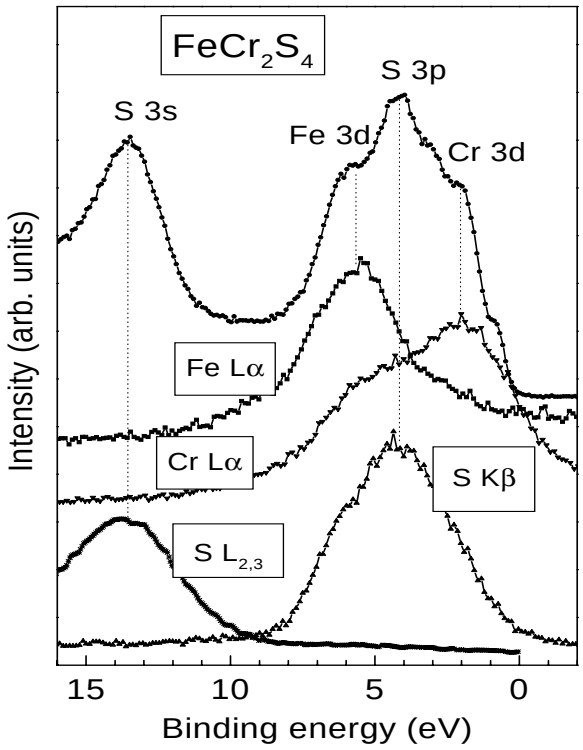

Figure 4.7: The XPS valence band, XES Cr Lα, Fe Lα, S Kβ and S $L_{2,3}$ spectra of the single crystal $FeCr_2S_4$.

level and a second peak at $\sim$ 13 eV, due to the S 3s states. The valence band spectrum of the Cu–doped compound shows an additional feature with the highest intensity at $\sim$ 2 eV, which appears to be due to the Cu 3d states. Indeed, the Cu Lα maximum is located at the same energy. There is no clear effect on the Fe 3d and Cr 3d partial density of states related to the Cu presence in the lattice, as one can observe from the shape of the Fe and Cr Lα XES spectra.

The electronic structures of $FeCr_2S_4$ and $Fe_{0.5}Cu_{0.5}Cr_2S_4$ have been calculated in the local density approximation (LDA) formalism by using the LMTO (linear muffin–tin orbital) method [134]. Similar calculations were performed in the LDA+U formalism, when the correlation effects (U) are taken into account [95].

The calculated densities of states (DOS) for both systems are shown in Fig. 4.9, where the thick line represents the occupied DOS broadened with the half–width parameter 0.25 eV, corresponding to the experimental resolution. By taking into

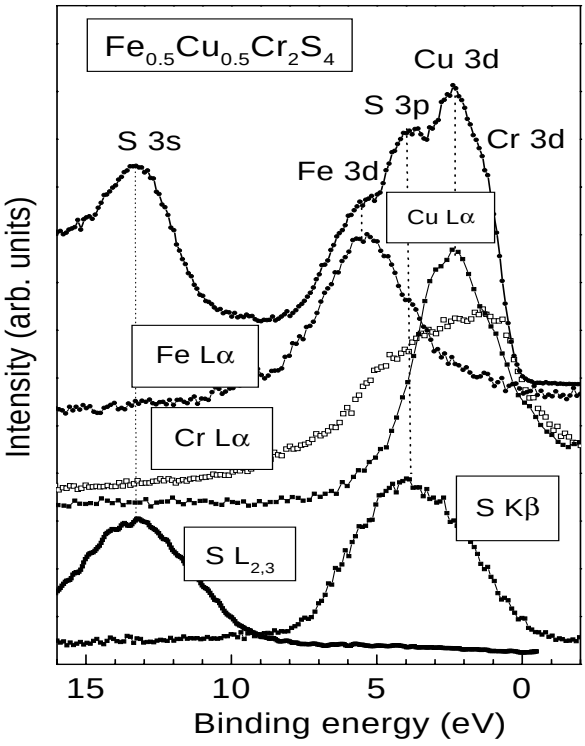

Figure 4.8: The XPS valence band, XES Cr Lα, Cu Lα, Fe Lα, S Kβ and S $L_{2,3}$ spectra of the single crystal $Fe_{0.5}Cu_{0.5}Cr_2S_4$.

account the photoionization cross sections of the constituent atoms the calculated density of states for $Fe_{0.5}Cu_{0.5}Cr_2S_4$ are strongly modified around 2 eV, where the Cu 3d states dominate [95]. This is because the Cu 3d photoionization cross section is very large with respect to the cross sections of the other constituent ions. One can observe a clear step near the bottom of the valence band spectrum of $FeCr_2S_4$, which is not present in the case of $Fe_{0.5}Cu_{0.5}Cr_2S_4$ (see Figs. 4.7 and 4.8). The states associated with this feature are given by the minority–spin state of Fe, as can be observed in Fig. 4.10, where the calculated spin–resolved partial density of states for $FeCr_2Se_4$ and $Fe_{0.5}Cu_{0.5}Cr_2S_4$ are shown.

The features at about 6 eV in the valence band spectra of both compounds can be clearly associated with the majority–spin Fe 3d states. The Cu 3d states are relatively localized and not affected by magnetic splitting. The magnetic moments at the Cr sites are antiparallel to the Fe moments and very large, 2.75μ_B, which is

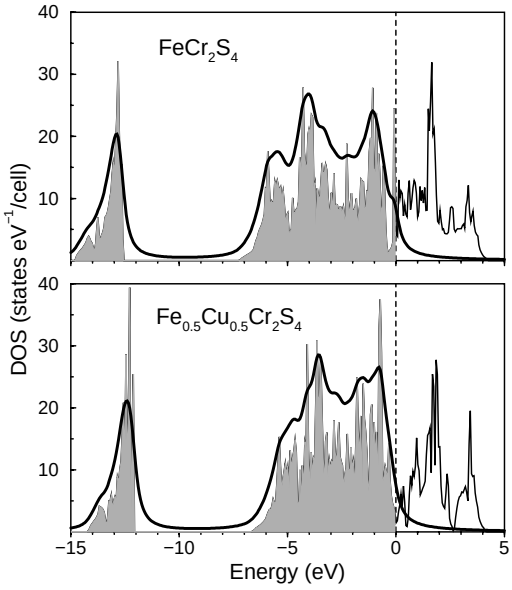

Figure 4.9: Total density of states (DOS) for $FeCr_2Se_4$ and $Fe_{0.5}Cu_{0.5}Cr_2S_4$ [95] (shaded parts); the thick lines correspond to the broadening of the calculated DOS with the half-width parameter 0.25 eV, that roughly corresponds to the spectrometer resolution.

in good agreement with the neutron diffraction data [130]. The exchange splitting of the Cr $3d$ states is smaller than the exchange splitting of Fe $3d$ and the energy position is higher. The contribution of the Cr $3d$ states to the XPS valence band spectrum is in the region of $1 \div 2$ eV, whereas the Cu $3d$ states are situated around $2 \div 3$ eV. These findings are in good agreement with the XPS and XES results presented above.

4.1.2 $CuCr_2Se_4$

Let us now discuss the last member of the $Fe_{1-x}Cu_xCr_2Se_4$ series, namely the very intriguing system $CuCr_2Se_4$. In the first part the Cu $2p$, Cu $3s$, Cr $2p$ and Cr $3s$ XPS core levels are presented and the electronic configurations of the corresponding ions are determined. In the second part the XPS valence band spectrum of the $CuCr_2Se_4$ single crystal is discussed in relation to the recently reported band structure calculations.

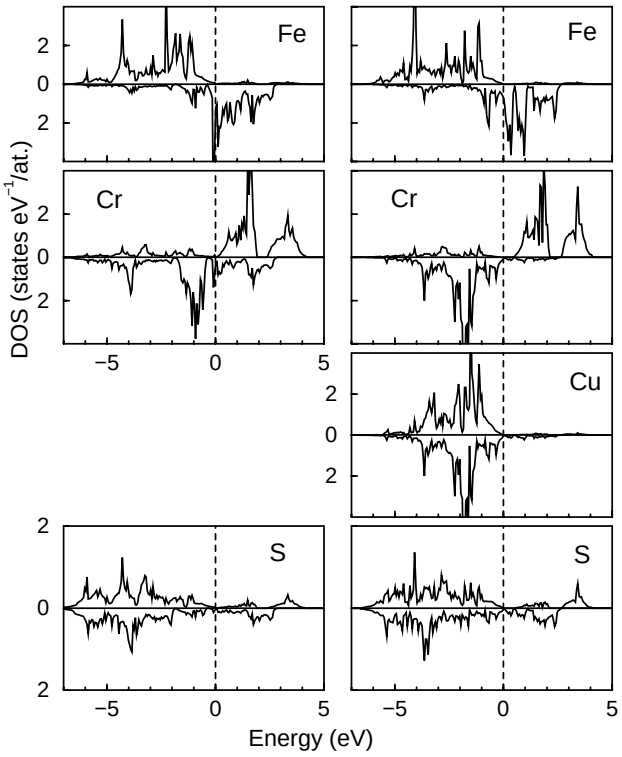

Figure 4.10: Calculated spin–resolved density of states for $FeCr_2Se_4$ (left) and $Fe_{0.5}Cu_{0.5}Cr_2S_4$ (right) [95].

4.1.2.1 XPS Cr $2p$, Cu $2p$, Cu $3s$ and Cr $3s$ core level spectra

In Fig. 4.11 the Cu $2p$ and Cr $2p$ core level XPS spectra of the $CuCr_2Se_4$ single crystal are presented. The Cu $2p$ spectrum exhibits a doublet structure due to the spin–orbit coupling. No additional features were detected, except for a broad shoulder that arises from the Cr LMM Auger states, which is also present in the case of $Fe_{0.5}Cu_{0.5}Cr_2S_4$ (see Fig. 4.3). The Cu $2p_{3/2}$ and Cu $2p_{1/2}$ peaks are located at 932.2 eV and 952.2 eV, respectively, values that are very close to those determined for several Cu^{1+} oxides [56] and spinels [95, 194]. The shape of the spectrum is very similar to the Cu $2p$ spectra of $Fe_{0.5}Cu_{0.5}Cr_2S_4$ (see Fig. 4.3).

The Cr $2p$ spectrum has a more complicated structure. Besides the spin–orbit doublet, Cr $2p_{3/2}$ and Cr $2p_{1/2}$, one can observe a well resolved splitting of the Cr $2p_{3/2}$ peak. The binding energy of the Cr $2p_{3/2}$ maximum is 573.7 eV and the splitting is $\sim$ 1 eV. An explanation of this splitting is given in detail in the

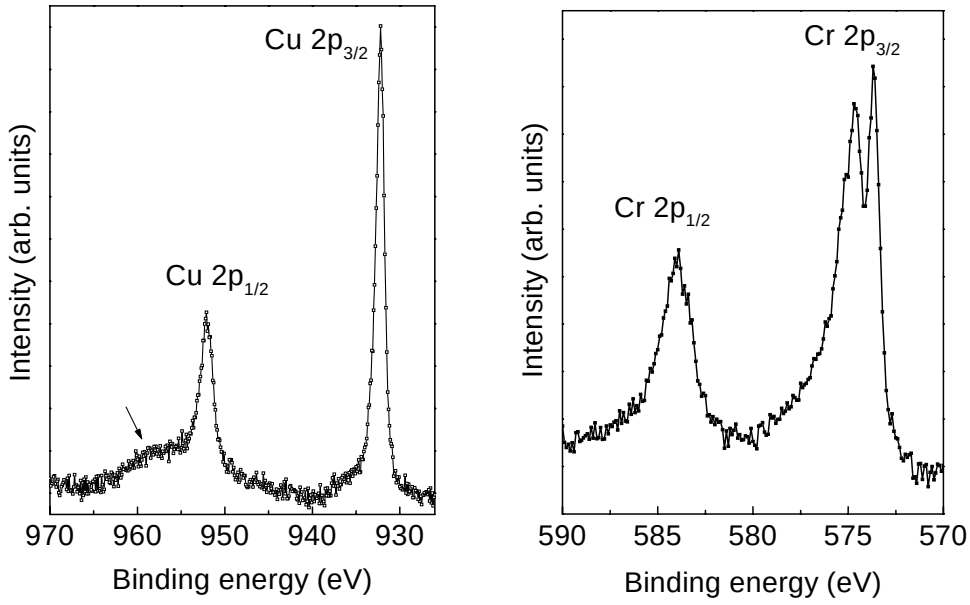

Figure 4.11: The XPS Cu $2p$ and Cr $2p$ spectra of $CuCr_2Se_4$ (single crystal).

Section 4.2.1, where similar behaviour is reported for other S and Se spinels.

The Cu $3s$ spectrum of the $CuCr_2Se_4$ single crystal (Fig. 4.12) does not exhibit exchange splitting, as for $Fe_{0.5}Cu_{0.5}Cr_2S_4$. This clearly shows that the Cu $3d$ states are fully occupied ($3d^{10}$) and therefore one can conclude that in $CuCr_2Se_4$ the formal valence of the Cu ions is 1+, in agreement with the Lotgering model [106, 107].

4.1.2.2 XPS valence band spectrum

The VB XPS spectrum of the $CuCr_2Se_4$ in the energy region from -2 eV to 10 eV is presented in Fig. 4.13. The valence band extends from Fermi level up to ~ 7.5 eV. The broad band has a two–peak structure (~ 2.5 eV and ~ 4 eV). The Se $4s$ only contributes with states at higher binding energies.

In order to identify the states in the valence band, we compare the experimental results with recently reported band structure calculations [9], which are shown in Fig. 4.14. The large band in Fig. 4.13 appears to derive from a bonding combination of Cu $3d$, Cr $3d$ and Se $4p$ states. The states close to the Fermi level are mainly due to Cr $3d$ and Se $4p$. At about $1.5 \div 2$ eV, the Cu $3d$ states

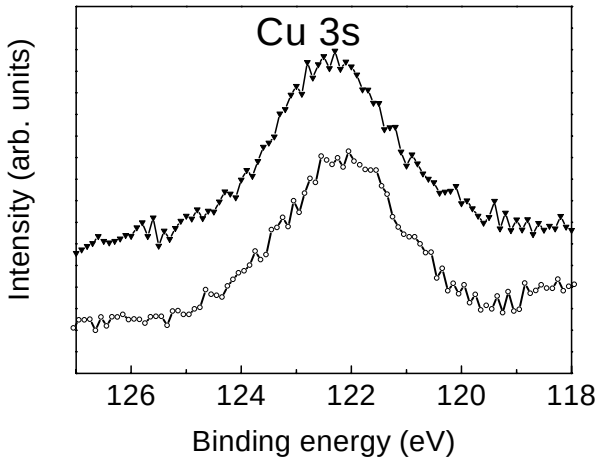

Figure 4.12: The XPS Cu 3s spectra of the single crystals: $CuCr_2Se_4$ (▼) and $Fe_{0.5}Cu_{0.5}Cr_2S_4$ (○).

dominate and give a large contribution to the total density of states (taking into account that the Cu 3d cross section is larger than that of Se 4p and Cr 3d). The Cr 3d states appear to be less localized than the Cu 3d states since they extend over a wider energy range. The sharp structure around 4 eV in the valence band spectrum reflects the Se 4p hybridized with the Cr 3d states, which extend also to higher binding energies.

4.2 Other spinel chalcogenides: ACr_2X_4

The $A^1Cr_2S_4$ (A^1= Cd, Mn, Fe, Fe: Cu) and $A^2Cr_2S_4$ (A^2= Cd, Cu, Hg, Hg: Cu) single crystals were grown by chemical transport reaction using chlorine or iodine as transport agents. The $ZnCr_2S_4$ polycrystals were prepared by solid state reaction [179].

The normal spinels $CdCr_2S_4$, $CdCr_2Se_4$ and $HgCr_2Se_4$ are semiconducting ferromagnets having the Curie temperatures of 85 K, 130 K and 106 K [13, 101], whereas $MnCr_2S_4$ is a semiconducting ferrimagnet with T_C= 95 K [62, 38]. In the case of $ZnCr_2S_4$ an insulating antiferromagnetic behaviour (T_N= 16 K) was reported [103, 86]. By contrast with most of the chalcogenide Cr spinels that are semiconductors, $CuCr_2S_4$ and $CuCr_2Se_4$ are metallic ferromagnets with Curie

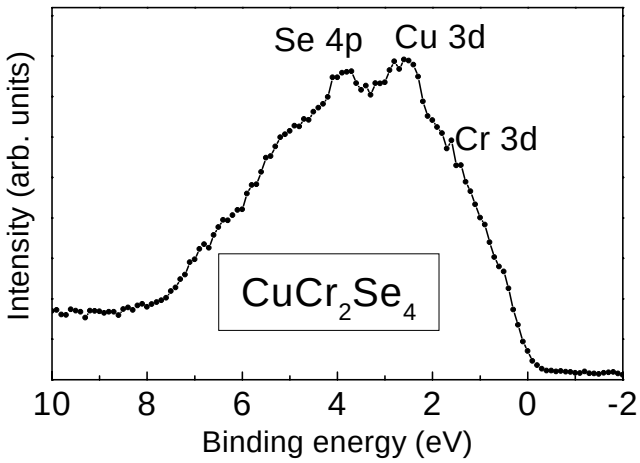

Figure 4.13: The XPS valence band spectrum of $CuCr_2Se_4$ (single crystal).

temperatures well above the room temperature (T_C= 377 K and T_C= 430 K, respectively [125]).

In the last few years the electronic structure of sulphur and selenium spinels has been an active topic of many studies due to their large variety of physical properties and their potential applications. Recently reported experimental and theoretical investigations of the electronic structure of related compounds, $Cu_{1-x}Ni_xRh_2S_4$ and $CuRh_2S_4$ [69], $CuIr_2S_4$ [113], CuM_2S_4 (M=Co, Rh, Ir) [127], CuV_2S_4 c[108], CuS, CuFe and $FeCuS_2$ [96], are consistent with the monovalent character of the Cu ions. In a previous XPS study of the $CdCr_2S_4$ and $ZnCr_2S_4$ spinels [15] the binding energies of the Cr $2p_{3/2}$ (575.7 eV and 575.6 eV) and S $2p$ levels (162.1 eV and 162.2 eV) were reported. The same Cr $3s$ splitting (4 eV) was found for both systems.

4.2.1 XPS Cr $2p$ core level spectra

The Cr $2p$ core level XPS spectra of the sulphide spinels $A^1Cr_2S_4$ (A^1= Zn, Mn, Cd, Fe, Fe:Cu), normalized to their maximum are presented in Fig. 4.15. For $MnCr_2S_4$ and $ZnCr_2S_4$ charging effects took place due to their more insulating character in comparison with the other studied compounds. By using a low energy electron flood gun, the charging effects could be neutralized.

For all investigated sulphides a clear splitting of the Cr $2p_{3/2}$ lines was found.

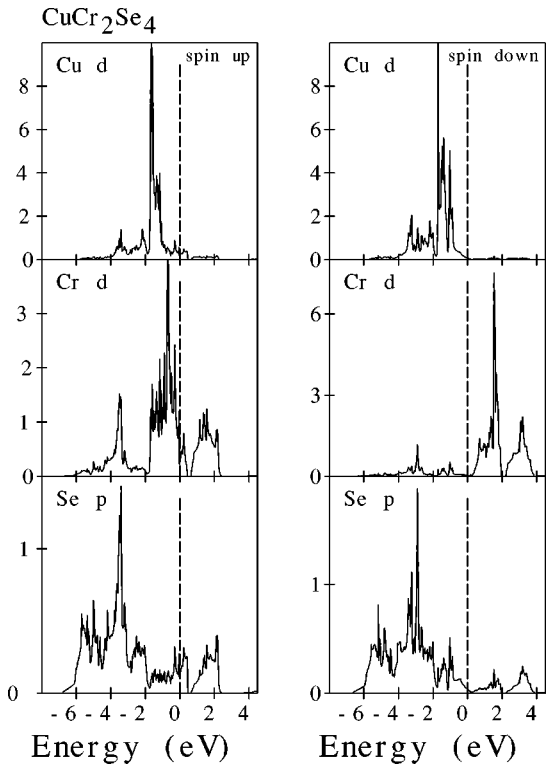

Figure 4.14: The spin–projected semirelativistic partial density of states of - $CuCr_2Se_4$ (states/atom eV spin) [9].

The value of this splitting, very similar for all investigated compounds, is $\sim$ 1.0 ± 0.1 eV.

For magnetic ions the splitting of their core levels is generally attributed to the spin polarisation of the $3d$ states. A similar splitting of the Mn $2p$ core level in half–metallic ferromagnetic Heusler alloys was recently reported and considered as a result of the well defined local $3d$ states of the Mn ions [197].

Very recently, the well resolved fine structure observed in the Mn $2p$ XPS $2p$ spectra of atomic Mn was interpreted on the basis of atomic multiplet splitting due to the $2p$–$3d$ Couloumb interactions [191]. The importance of the interaction $2p$–core hole and $3d$–valence electrons was also underlined for Cr by a linear magnetic dichroism study [190, 189].

A very well resolved splitting of the Cr $2p_{3/2}$ levels was also observed in Cr–chalcogenide selenides. The Cr $2p$ XPS spectra of the $A^2Cr_2Se_4$ (A^2= Cd, Hg,

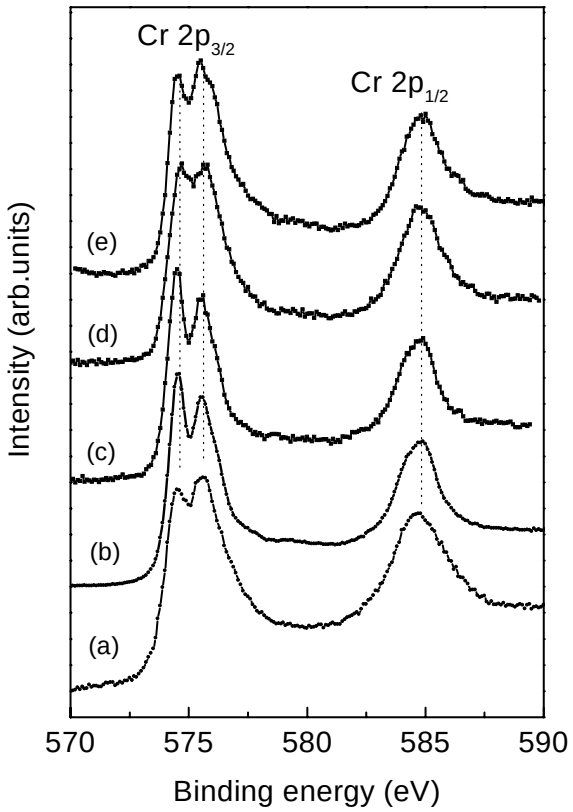

Figure 4.15: The XPS Cr $2p$ spectra of: $ZnCr_2S_4$, polycrystal (a), $MnCr_2S_4$ (b), $CdCr_2S_4$ (c), $FeCr_2S_4$ (d) and $Fe_{0.5}Cu_{0.5}Cr_2S_4$ (e) - single crystals.

Hg: Cu, Cu) single crystals are presented in Fig. 4.16. The value of the Cr $2p_{3/2}$ splitting for selenides was found be very similar to that found for sulphides (see Fig. 4.15).

A linear dependence between the Mn $2p$ splitting and the local magnetic moments in some Heusler alloys was recently determined [136]. In order to estimate the magnetic moment at the Cr–site in the investigated compounds, we have used the magnetic moments values from literature and compared the Cr $2p_{3/2}$ and Mn $2p_{3/2}$ splittings [136]. For Co_2MnAl a Mn local magnetic moment of 3.0 μ_B was determined by neutron scattering and a Mn $2p$ splitting of 1.0 eV was measured ([197]). For $MnCr_2S_4$, $CdCr_2S_4$ and $Fe_{1-x}Cu_xCr_2S_4$ (x=0.0, 0.5) values of the local Cr magnetic moment of 3 μ_B and 2.9 μ_B were reported [116, 140,

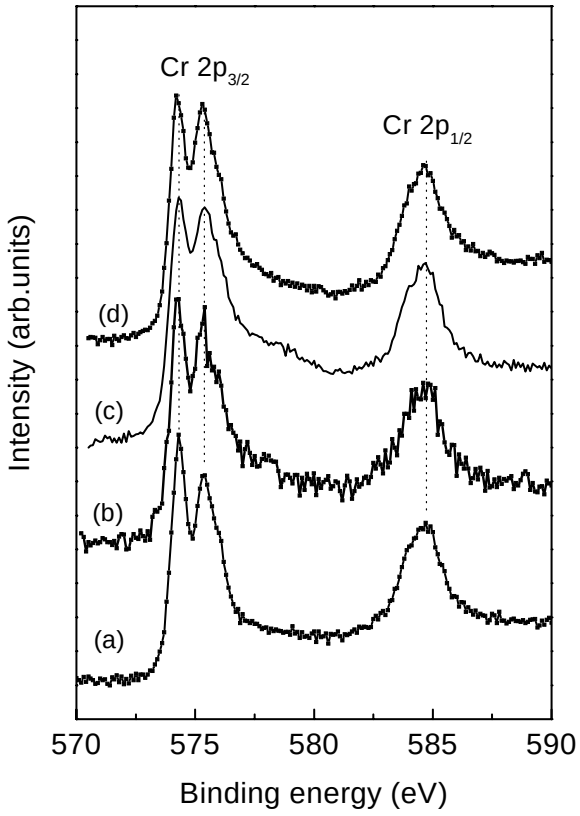

Figure 4.16: The XPS Cr $2p$ spectra of the single crystals: $CdCr_2Se_4$ (a), $HgCr_2Se_4$ (b), (Hg:Cu)Cr_2Se_4 (c) and $CuCr_2Se_4$ (d).

159, 130]. The Cr $2p_{3/2}$ splitting value of 1 ± 0.1 eV corresponds to a magnetic moment of 3 μ_B, which is in good agreement with the values determined by neutron diffraction and magnetic measurements.

Although the investigated compounds exhibit completely different macroscopic magnetic properties, the same values of the Cr $2p$ splitting could indicate similar values of the local magnetic moment of the Cr^{3+} ions with the $3d^3$ electronic configuration.

4.2.2 XPS Cr $3s$, Mn $3s$ and Fe $3s$ core level spectra

Fig. 4.17 shows the Cr $3s$ spectra of ACr_2S_4 (A= Mn, Zn, Cd) and (Fe, Cu)Cr_2S_4 crystals. For all investigated sulfides a well resolved Cr $3s$ multiplet splitting (~ 4

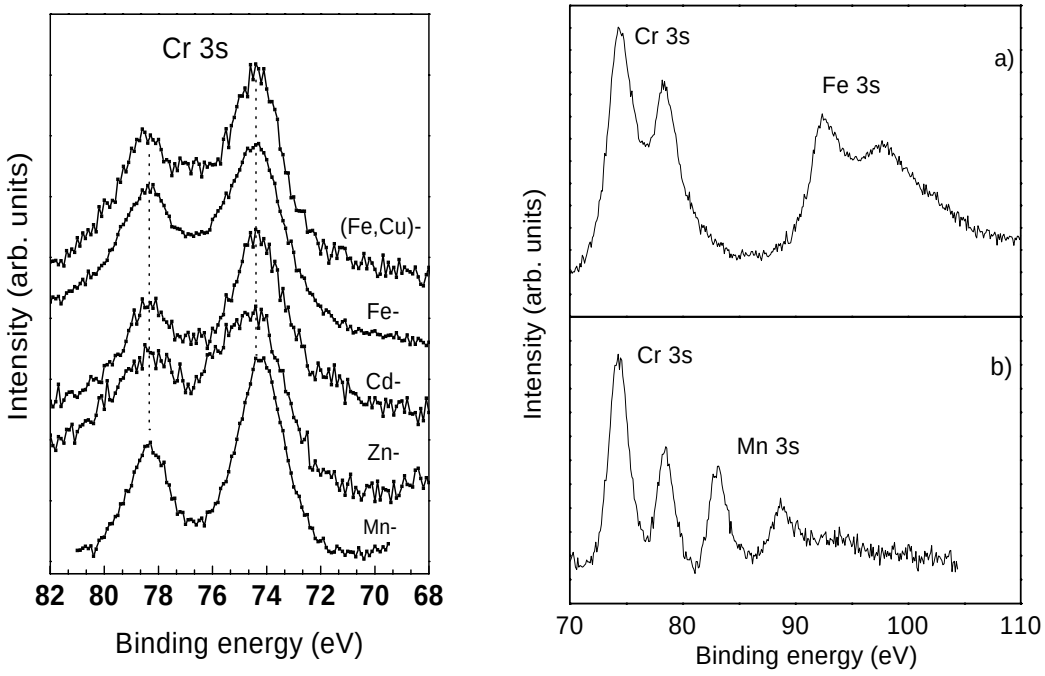

Figure 4.17: The XPS Cr 3s spectra of the ACr_2S_4 (A= Mn, Zn, Cd, Fe, Fe:Cu) crystals (left); XPS Fe 3s (a) and Mn 3s spectra (b) of the single crystals $MnCr_2S_4$ and $FeCr_2S_4$ (right).

eV) can be observed; the same value of the splitting indicates similar Cr–magnetic moments in the investigated samples. The electronic configurations of the Cr ions in ACr_2S_4 (A= Mn, Zn, Cd, Fe, Fe: Cu) is the same and its value corresponds to Cr $3d^3$ [57]. A previous study of the $CdCr_2S_4$ polycrystals reported similar values of the Cr exchange splitting [15].

The Fe 3s and Mn 3s spectra of $FeCr_2S_4$ and $MnCr_2S_4$ are presented in Fig. 4.17. There is a well resolved splitting of the 3s levels in both cases. For the $FeCr_2S_4$ single crystal we found a Fe 3s splitting of 5.4 eV, which corresponds to Fe^{3+} and is in very good agreement with the neutron diffraction results obtained for the polycrystalline samples of the same compound [159]. In binary manganese oxides, a splitting of the Mn^{2+} 3s level of 6.2 eV was reported [57]. For $MnCr_2S_4$ we found a splitting of the Mn 3s of 5.7 eV, smaller than we would expect for Mn^{2+}. There are two possible explanations for the observed effect: (1) the magnetic moment is reduced due to the existence of Mn^{3+}, or (2) the measured 3s

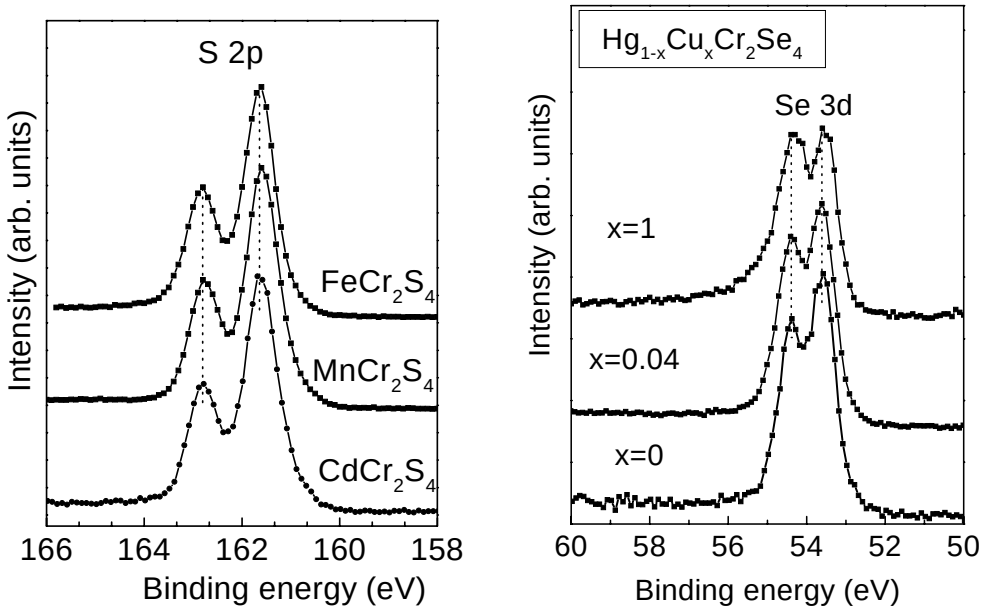

Figure 4.18: The XPS S $2p$ spectra of ACr_2S_4 (A= Cd, Mn, Fe) (left) and XPS Se $3d$ spectra of $Hg_{1-x}Cu_xCr_2Se_4$ ($x = 0; 0.04; 1$) (right).

splitting is smaller due to the covalence effect, as reported for other Mn compounds [66]. We associate the reduced Mn $3s$ splitting with covalency since the existence of Mn^{3+} was completely ruled out [126]. Therefore, one can conclude that in $MnCr_2S_4$ the Mn ions are bivalent having a $3d^5$ electronic configuration. This result is in agreement with the reported neutron diffraction data, where a magnetic moment of $4.7\mu_B$ was found for Mn^{2+} [116].

The S $2p$ spectra of ACr_2S_4 (A= Cd, Mn, Fe) are presented in Fig. 4.18. The spectral shape is the same for the investigated sulphur spinel and they are typical for bivalent S ions. There is no indication of sulphur dimers, as observed for CuS or FeS_2.

The Se $3d$ spectral shape of $Hg_{1-x}Cu_xCr_2Se_4$ ($x = 0; 0.04; 1$) do not change with composition. In the Fig. 4.18, the spectra for $Hg_{0.96}Cu_{0.04}Cr_2Se_4$and $HgCr_2Se_4$ were shifted by 0.3 eV and 0.5 eV, respectively, due to the charging effect. There is no charge effect for $CuCr_2Se_4$, since it has a metallic behaviour.

In this chapter we have investigated Cr–chalcogenide spinels ACr_2X_4 (where A= Mn, Fe, Cu, Zn, Hg; X=S, Se). X–ray photoelectron and X–ray emission spectrocopy were used to study their electronic structures. Although they have been intensively investigated since the '60s, there are still open questions related to their properties.

A special attention was paid to the $Fe_{1-x}Cu_xCr_2S_4$ ($x = 0.0; 0.5$) compounds, not only because they were recently reported as exhibiting CMR effect close to the room temperature, but also in order to investigate the long–standing controversy related to the Cu valence in these systems. Single crystals were investigated.

From the exchange splitting of the Cu $3s$ states, we have concluded that in $Fe_{1-x}Cu_xCr_2S(Se)_4$ ($x = 0.0; 0.5; 1.0$) the Cu ions are in the Cu^{1+} state, in accordance with the Lotgering model [106, 107]. Additional information about the electronic configurations of the constituent ions was obtained from other core level XPS spectra (Cu $2p$, S $2p$, Fe $2p$, Fe $3s$, Cr $2p$ and Cr $3s$). The Fe $3s$ and Cr $3s$ splitting values indicate $3d^6$ and $3d^3$ electronic configurations for Fe and Cr. Furthermore, making use of the XPS and XES techniques, we have determined the partial contributions of the constituent ions to the valence band. The experimental data were found to be in excellent agreement with the *ab-initio* TB–LMTO band structure calculations [95]. For $FeCr_2S_4$, the valence band consists of Fe $3d$, Cr $3d$ and S $3p$ states. The Cr $3d$ states were found to be less localized than the Fe $3d$ states. On going from $FeCr_2S_4$ to $Fe_{0.5}Cu_{0.5}Cr_2S_4$, no significant changes in the Cr $3d$ and Fe $3d$ states distribution were observed. The Cu $3d$ states were identified just below the Cr $3d$ states.

The similar Cr $3s$ splitting for all investigated compounds suggests the same $3d^3$ electronic configuration of the Cr ions, although they have different electronic and magnetic properties. The well resolved Cr $2p$ splitting observed for all investigated sulfides and selenides reveals the localized character of the Cr magnetic moments and its value corresponds to the $3d^3$ electronic configuration.

Chapter 5

Vanadium oxides

The vanadium oxides have been extensively studied over the past few decades due to their interesting electric and magnetic properties. It is well known that many compounds may form in the vanadium–oxygen system, such as V_2O_3, V_2O_5 and VO_2, VO, V_nO_{2n-1} (Magnéli phases) and $V_{2n}O_{5n-2}$ (Wadsley phases). Most of the vanadium oxides exhibit metal–to–insulator transitions (MIT) and many experimental and theoretical studies have been done in order to investigate the mechanism behind MIT [123, 3, 76].

5.1 V_2O_3, V_2O_5 and VO_2

Many spectroscopic studies have been perfomed on vanadium oxides, including X–ray photoelectron (XPS), X–ray absorption (XAS), X–ray emission (XES) spectroscopies [154, 41, 208, 209, 83, 2, 156, 192, 35]. Despite this, there are still many open questions related to the surface characterisation of V_2O_5, the phase transitions mechanism in V_2O_3 and VO_2, which is related by some authors to a Mott–Hubbard scenario, whereas others attribute it to the electron–phonon coupling on the basis of the change in crystal symmetry.

V_2O_5 is a diamagnetic insulator with a layer type orthorhombic structure ($Pmnm$), widely used as catalyst [26, 169]. There are three structurally different oxygens: vanadyl oxygens, coordinated to only one vanadium atom through a short distance (1.58 Å), bridge oxygens, coordinated to two vanadium atoms and chain oxygens, coordinated to three vanadium atoms, respectively (see Fig. 5.1).

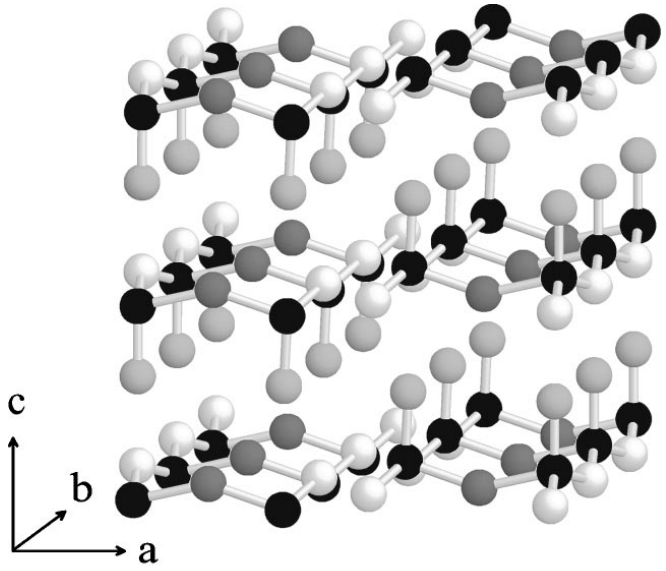

Figure 5.1: Crystal structure of V_2O_5: vanadium atoms are represented by black spheres and the three types of oxygen atoms, vanadyl, bridge and chain are shown as light gray, dark gray and white spheres, respectively [11].

The V $2p$, O $1s$ and V $3s$ core level XPS spectra of the V_2O_5 single crystal[1] are shown in Fig. 5.2. The V $2p_{3/2}$ level exhibits a narrow line at $\sim$ 517.1 eV and the O $1s$ peak is located at 530 eV. Similar values were previously reported [14, 154, 115, 83]. No splitting of the V $3s$ line was observed, according to the $3d^0$ electronic configuration of the V^{5+} ions.

The valence band spectrum, shown in Fig. 5.3, consists of a wide band with the highest intensity at $\sim$ 5.5 eV. Other two structures can be observed in the spectrum, at the bottom and top of the wide band ($\sim$ 7.4 eV and $\sim$ 3.5 eV). The O $2s$ level has a binding energy of $\sim$ 21.5 eV.

Band structure calculations of V_2O_5 have been performed since early $80's$ [99, 25] and the results were in agreement with the available experimental data [54, 53]. Recent calculations based on density–functional theory [49, 29] pointed out the hybridization of the V $3d$ and O $2p$ states in the valence band. The partial

[1] all vanadium oxide–single crystals investigated in this study were provided by W. Reichelt, Inorg. Chem. Dept., Univ. of Dresden.

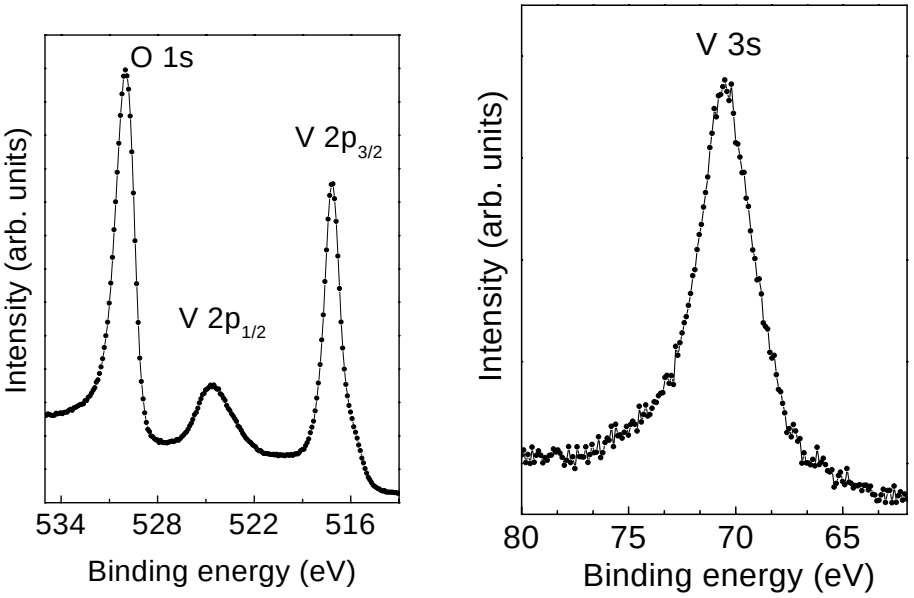

Figure 5.2: XPS core level spectra of the single crystal V_2O_5: V $2p$ and O $1s$ (left), V $3s$ (right).

densities of states (PDOS) for different oxygen types in V_2O_5 have been calculated [11, 72, 49, 29, 210] and it has been shown that the vanadyl oxygen $2p$ states are localized near the center of the valence band, whereas the PDOS of the bridge and chain oxygens extent over the whole energy range of the valence band. Therefore we associate the most prominent peak in the spectrum at ~ 5.5 eV with emission from terminal oxygen and the features at the top and bottom of the VB with bridging oxygen $2p$ states, hybridized with V $3d$.

A photoemission feature in the O $2s$–O $2p$ band gap of V_2O_5 was found at ~ 11.2 eV [158]. Similar satellite structures in the valence band spectrum has been assigned to the inelastic scattering of the photoexcited O $2p$ electrons [64]. Anyway, in our spectra of a fresh cleaved single crystal we do not observe any satellite structures. In [93] it has been shown that the existence of such additional structure in the valence band spectrum of VO_2 is not an intrinsic feature of the electronic structure, but connected with carbon contamination.

VO_2 undergoes a lattice coupled insulator–to–metal transition around 340 K. The low–temperature monoclinic structure ($P2_1/c$) changes at the transition

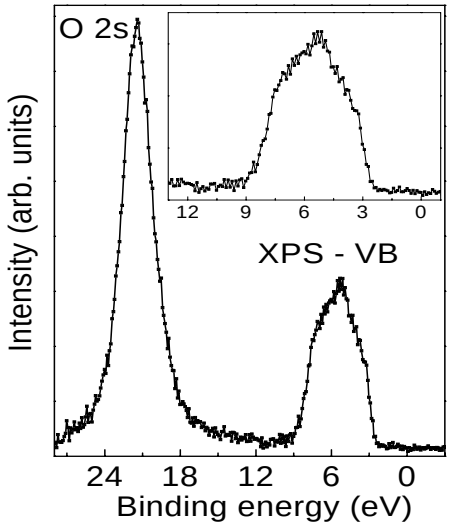

Figure 5.3: XPS valence band spectrum of the single crystal V_2O_5.

temperature to a distorted rutile phase ($P4_2/mnm$). Due to the cubic component of the octahedral crystal field the V $3d$ levels are split into triply degenerate lower t_{2g} and doubly degenerate e_g levels. One of the t_{2g} orbitals points toward the orbital of the nearest vanadium atom and forms the $d_{||}$ band. The other two t_{2g} orbitals are hybridized with the O $2p$ orbitals and form the π^* band. The higher e_g orbitals are highly hybridized with the O $2p$ orbitals and form a wide σ^* band [63].

In the metallic phase, the narrow $d_{||}$ band overlaps with the π^* band of the antibonding V–O orbitals and gives the metallic conduction as a result of partial occupancy ($d_{||}^{0.7}\ \pi^{*\ 0.3}$) [20]. In the insulating phase the $d_{||}$ band is split into upper and lower $d_{||}$ bands. The π^* band is now situated above the Fermi level, between the two $d_{||}$ bands, as illustrated in Fig. 5.4.

The XPS core level V $2p$, O $1s$ and V $3s$ spectra of the VO_2 single crystal are presented in Fig. 5.5. The V $2p_{3/2}$ and O $1s$ peaks are located at ~ 516 eV and 530 eV, respectively.

The VB spectrum, shown in Fig. 5.6, consists of a wide band ($3 \div 9$ eV) with a two–peaks structure and a low intensity peak below the Fermi level, centered at ~ 1 eV. In order to find the partial contributions of the V and O states in the valence band spectrum we use the soft X–ray emission results [156]. The peak

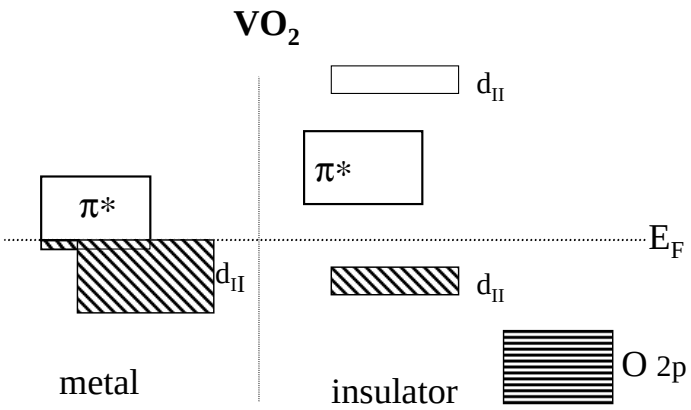

Figure 5.4: Schematic energy diagram of the V $3d$ bands around the Fermi level for VO_2 (after [157]).

close to the Fermi level mainly arises from the V $3d$ states; the O $2p$ contribution in this energetic region is low, but not zero [156]. The large band consists of highly hybridized O $2p$ and V $3d$ states: the feature at about 5.5 eV corresponds to the maximum of the O $1s$ emission spectrum, whereas the second structure at 7.3 eV has a strong V $3d$ component. These results are in good agreement with band structure calculations [93, 209, 34]. Therefore, one can conclude that V $3d$ and O $2p$ are strongly hybridized with each other over the full energy range of VB.

V_2O_3 is one of the first examples of a material exhibiting an interaction–driven Mott–Hubbard metal–to–insulator transition. It exhibits the MIT at 160 K with a conductivity increase of 6–7 orders of magnitude. The room temperature corundum (Al_2O_3–type) structure in which the vanadium ions are arranged in V–V pairs along the c axis and form a honeycomb lattice in the ab plane changes at the transition temperature to a hexagonal crystal structure.

The oxidation state of the vanadium ions is V^{3+} with a $3d^2$ configuration. Each V ion is surrounded by an octahedron of O atoms. Due to the trigonal distorsion of the V_2O_3 lattice, the t_{2g} orbitals are split into nondegenerate a_{1g} and double degenerate e_g levels. Although direct information about the electronic structure of V_2O_3 has been obtained by photoemission and other spectroscopic studies since

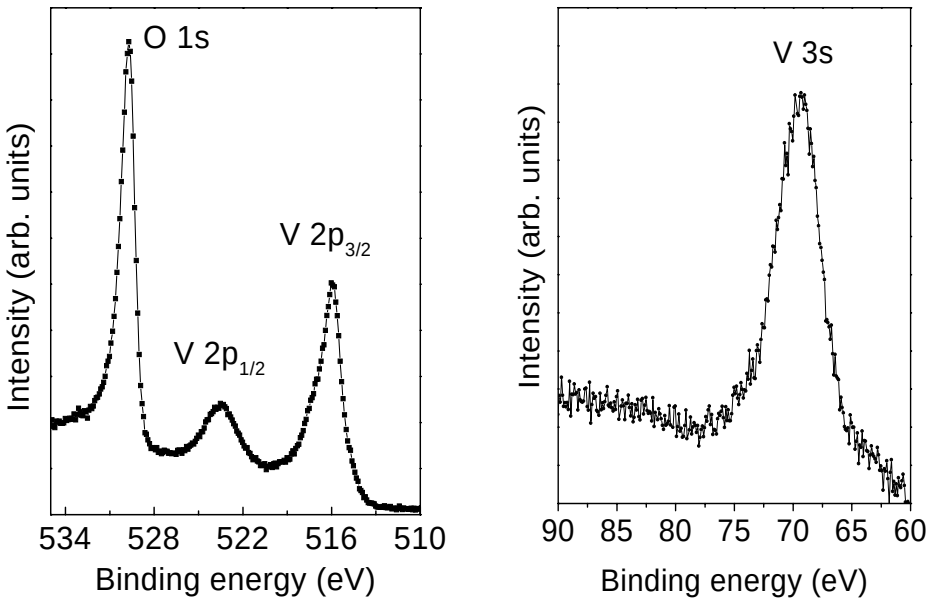

Figure 5.5: XPS core level spectra of VO_2: V2p and O 1s (left), V 3s (right)

the 1970s the electronic state of this material is still controversial.

5.2 Mixed–valence compounds: V_6O_{13}, V_4O_7 and V_3O_5

V_6O_{13} is the most important lower oxide of V_2O_5. The crystal structure was determined as formed by VO_6 octahedra linked together by edges and corners [4, 193]. Like other vanadium oxides, it exhibits a phase transition from a metallic state to a semiconductor at T_t= 145 K. V_6O_{13} is a mixed–valence oxide, consisting of V^{4+} ($3d^1$) and V^{5+} ($3d^0$) ions. The MIT mechanism in this compound has been the subject of several experimental studies [157].

The V_3O_5 shows a phase transition around 425 K. Unlike the above systems, its monoclinic structure does not change through the transition point (there is only a small change in the lattice parameters) [32, 84]. There are very few spectroscopic studies related to the metal–insulator transition in V_3O_5 [185].

The metal–insulator transition for V_4O_7 occurs at 250 K [89]. In the crystal

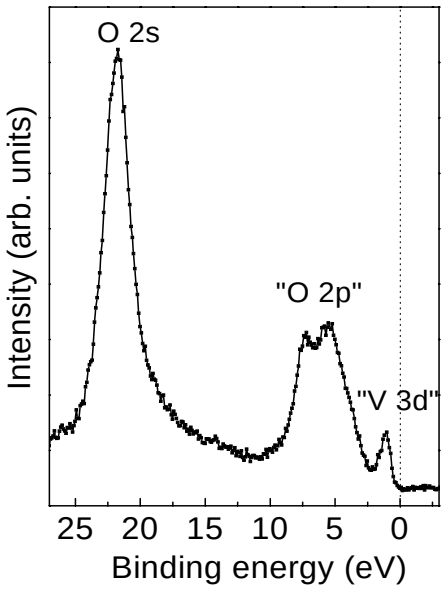

Figure 5.6: XPS valence band spectrum of the single crystal VO_2.

structure of V_4O_7, considered to consist of two regions, rutile–type and corundum–type, the oxygen atoms form a deformed hexagonal close packing arrangement [74].

5.2.1 XES V Lα and O Kα, XPS valence band and V $2p$ spectra

In the Fig.5.7 the XPS valence band, V Lα and O Kα XES spectra for the V_6O_{13} polycrystal are shown. In the same figure we present a comparison of the valence band XPS spectra of the V_2O_5, V_6O_{13} and VO_2 single crystals. The valence band spectra of the single– and poly–crystals are similar. They consist of a small peak close to the Fermi level, as for VO_2 and a wide band that arises from O $2p$ states hybridized with V $3d$ states, as can be deduced from the comparison of the XPS VB with the XES spectra (see Fig.5.7).

UPS spectra have been previously reported [157] and a three-peaks structure of the wide band ($2 \div 8$ eV) was observed, similar to V_2O_5. The origin of the small peak is mainly of V $3d$ character, but the O $2p$ contribution in this energy region is not zero, as one can deduce from the shape and position of the O Kα

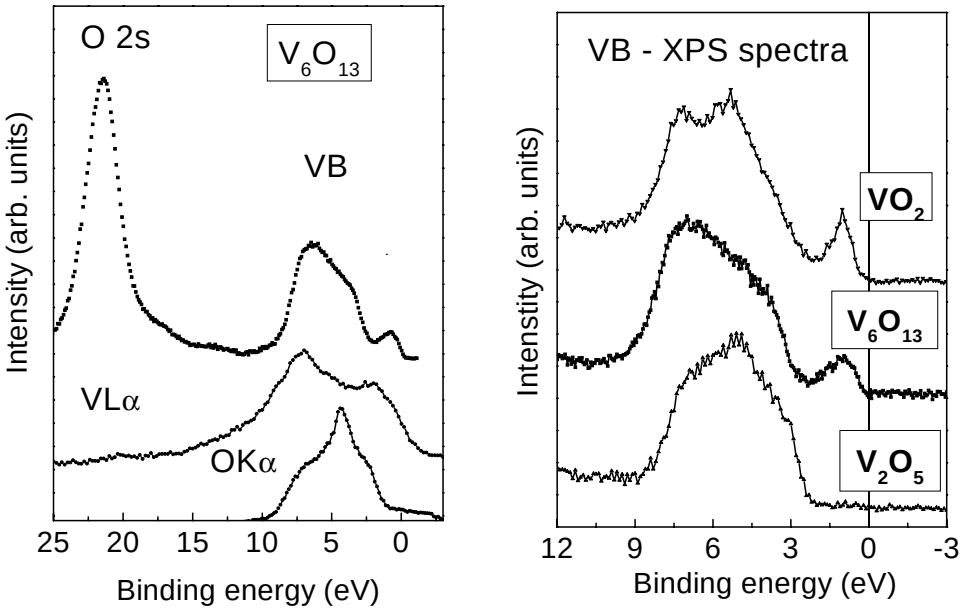

Figure 5.7: XPS valence band, XES V Lα and O Kα spectra of the V_6O_{13} polycrystal (left); XPS valence band spectra of the V_2O_5, V_6O_{13} and VO_2 – single crystals (right).

XES spectrum. Therefore, one can conclude that there is a strong hybridization of the V $3d$ and O $2p$ states in the VB of V_6O_{13}.

The V $2p$ core level spectra for several vanadium oxides: V_6O_{13}, V_4O_7, V_3O_5 recorded at the room temperature are presented in Fig. 5.8. For comparison the V $2p$ spectra of V_2O_5, VO_2 and V_2O_3 are also shown. For V^5 the V $2p_3$ line is narrow, but for the other systems it becomes broader. The broad structures of the V $2p_3$ lines in $VO_2(V^4)$ and $V_2O_3(V^3)$ were explained by the various multiplet configurations in the photoemission final states, related with the core hole–$3d$ electrons interaction [209, 154, 164]. Such effect is particularly strong in V_2O_3, where there are two electrons in the V $3d$ shell. A clear step was found at the low binding energy side of the V $2p_{3/2}$ line in V_2O_3. This structure remains visible in the V $2p$ spectra for V_4O_7 and V_3O_5. For V_6O_{13}, V_4O_7, V_3O_5 wide V $2p$ lines are expected due to the mixed–valence character of the vanadium ions. However, for V_4O_7, V_3O_5, as well as for V_2O_3 the large width of the V $2p$ lines might be due, to some extent, to the occurrence of the defects at the surface; the feature

seen at $\sim$ 512.7 eV (close to the V $2p_{3/2}$ binding energy for V metallic) could originate from defects and/or a disproportion at the surface. For V_6O_{13} and V_4O_7 asymmetrical line (Doniach–Sunjic) shapes are observed, characteristic for metallic systems.

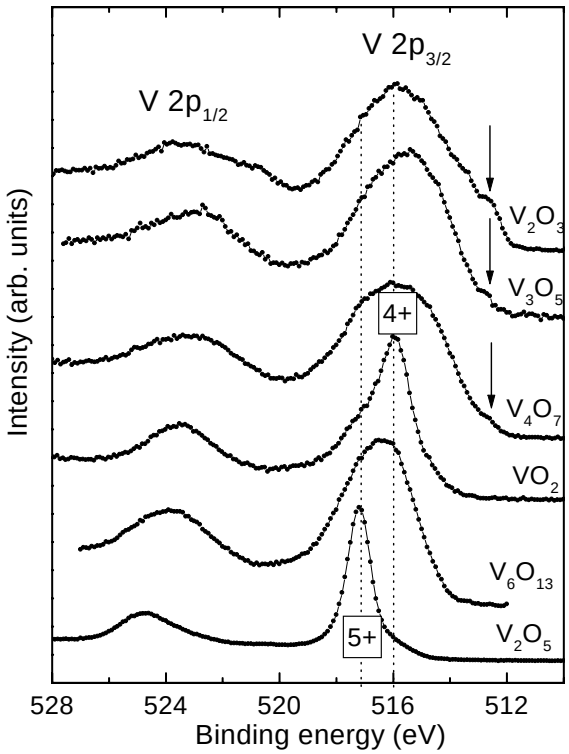

Figure 5.8: The XPS V $2p$ spectra for V_2O_5, V_6O_{13}, VO_2, V_4O_7, V_3O_5 and V_2O_3–single crystals.

5.2.2 XPS study of the metal–insulator transition in V_6O_{13}, V_4O_7 and V_3O_5

The valence band spectra of V_6O_{13}, V_4O_7 and V_3O_5, below and above the metal–insulator transition temperatures (145 K, 250 K and 425 K, respectively) are presented in Fig. 5.9. There are no real changes in the "O $2p$ band", so we will focus our attention on the small peak located close to the Fermi level.

For V_3O_5 there is a change in the "V $3d$ band" shape and intensity through the

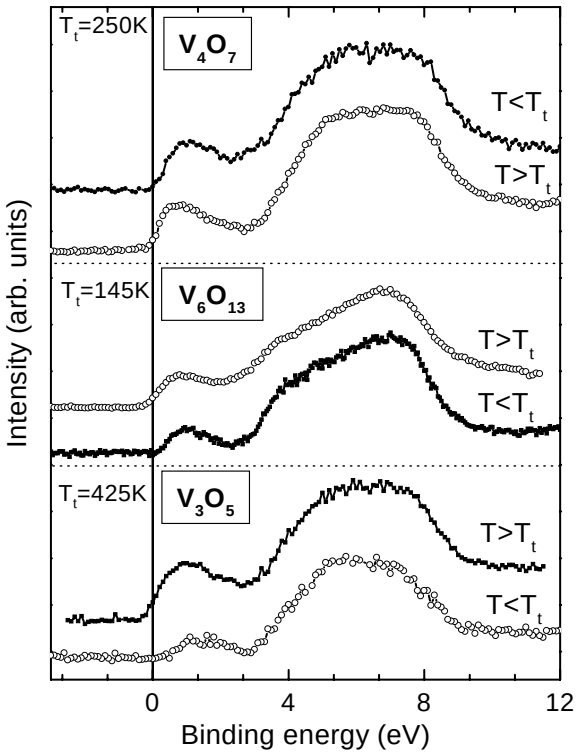

Figure 5.9: The valence band spectra for V_6O_{13}, V_4O_7 and V_3O_5 – both phases: metallic and insulating.

transition point. The width of the band is almost the same in the two phases. A possible explanation for the low intensity of this band at room temperature is the oxidation effect which could occur at the surface. Previously, it was reported that at the transition temperature the valence band spectra of V_3O_5 slightly shifts to lower binding energy and the V $3s$ and V $3p$ levels (~ 0.3 eV) also shift to lower binding energies as compared to the spectra recorded at room temperature [185].

For V_6O_{13} a very small shift of the "V $3d$ band" maximum through the transition point is observed (see Fig.5.9). Using UPS a shift of ~ 0.15 eV to smaller binding energies in the insulating phase was reported [157].

Clear changes are observed in the VB spectra of V_4O_7 through the MIT. The V $3d$ peak becomes wider in the metallic phase. A finite spectral weight at the Fermi level at room temperature is observed, consistent with its metallic behaviour.

5.3 Mo–doped vanadium oxides: $V_{2-x}Mo_xO_5$

Vanadium oxides are very interesting due to the variety of the vanadium oxidation states ($2+ \div 5+$). In the binary vanadium oxides the mixed–valence state can be realized by changing the V/O ratio, whereas in the ternary oxides when the vanadium ions are substituted by other transition metals with different number of d–electrons.

In the vanadium bronzes, $M_xV_2O_5$ or $M_xT_yV_{2-y}O_5$, (where M is a monovalent metal, as Na and T= Mo, W) V^{5+} apparently must switch to V^{4+} in order to accommodate the charge of the additional cations. Many studies have been done on the electric and magnetic properties of these very interesting materials [177]. Unfortunately, the tuning of the vanadium valence in these compounds was directly observed only in few cases using spectroscopic techniques. X–ray absorption spectroscopy was used in order to determine the charge state and the coordination geometry in a series of mixed–valence vanadium bronzes [110].

Here we report a spectroscopic study of the mixed-valent system $V_{2-x}Mo_xO_5$ by using X–ray photoelectron and X–ray emission spectroscopy [2].

- *Experimental details*

The $V_{2-x}Mo_xO_5$ compounds were prepared by the hydrochemical method with mixing of V_2O_5 and Mo and adding of water with consequent annealing at 700°C during 100 hours. According to the thermochemical analysis compounds with chemical formula $V_{2-x}Mo_xO_5 \times H_2O$ were formed. The crystal structure of these compounds was identified to be the same as for V_2O_5 (orthorhombic) with the lattice parameters for $V_{1.3}Mo_{0.7}O_5 \times 1.4\ H_2O$: $a = 11.521(7)$ Å, $b = 3.570(2)$ Å and $c = 4.375(3)$ Å.

The XPS spectra were recorded with the Phi $5600ci$ spectrometer using mono chromatized Al Kα radiation. The energetic resolution, determined as 1.5 % of the pass energy, was estimated to be ~ 0.35 eV. During the measurements the pressure in the main chamber was below $5 \cdot 10^{-9}$ mbar. The pressed pellets of the

[2] This study was done in collaboration with Prof. Kurmaev group, Ekaterinburg, where the XES measurements were performed and Dr. A. Postnikov, who performed the band structure calculations [43, 44].

$V_{2-x}Mo_xO_5$ samples were cleaved in ultra–high vacuum before the XPS measurements. The contamination with carbon was found to be low. All investigations were performed at room temperature. The spectra were calibrated using the Au $4f_{7/2}$ signal ($E_B(4f_{7/2})$= 84.0 eV) from an Au-foil.

The Mo L$\beta_{2.15}$ X–ray emission spectra were measured using a fluorescent Johan–type spectrometer with position–sensitive detector [45]. The energy position was detected with the accuracy of ± 0.25 eV.

The V Lα and O Kα X–ray emission spectra were measured with a RSM–500 type X–ray vacuum spectrometer with a diffraction grating (N= 4600 lines/mm; R= 6 m) and electron excitation. Spectra were recorded in the first order of reflection by a secondary electron multiplier with a CsI photocathode. The energy resolution was $\sim$ 1 eV.

5.3.1 XPS core level spectra: Mo $3d$, V $2p$ and O $1s$

In order to get information about the changes in the electronic structure of the $V_{2-x}Mo_xO_5$ solid solutions by varying the Mo doping, we have investigated the Mo $3d$, O $1s$ and V $2p$ core levels by using X–ray photoelectron spectroscopy.

In Fig. 5.10 one can observe that the Mo $3d$ XPS spectra do not change with the Mo doping and are very similar to the Mo $3d$ spectrum of MoO_3 (Mo^{6+}, $4d^0$). The O $1s$ XPS spectra are very similar for all investigated compounds. The O $1s$ peaks are situated at the same binding energies. Moreover, the O $1s$ FWHMs (full width at half–maximum) does not depend on the Mo content (see inset in Fig. 5.10, right panel).

Thus, we can conclude that the variation of the valences in the $V_{2-x}Mo_xO_5$ system is not due to the possible changes of the oxidation states of the Mo atoms and also that no oxygen holes (O^-) are created during Mo–doping.

Further, we have investigated the V 2p core level XPS spectra (Fig. 5.11) in order to check the possible changes in the electronic configuration of the vanadium ions. For all investigated samples, the V $2p$ XPS spectra show doublet structures, due to the spin–orbit coupling. The V $2p_{3/2}$ lines have similar characteristics: a maximum located at 517 eV and a shoulder at $\sim$ 516 eV. The first feature is located at the same binding energy as the V $2p_{3/2}$ peak of V_2O_5, where only V^{5+}

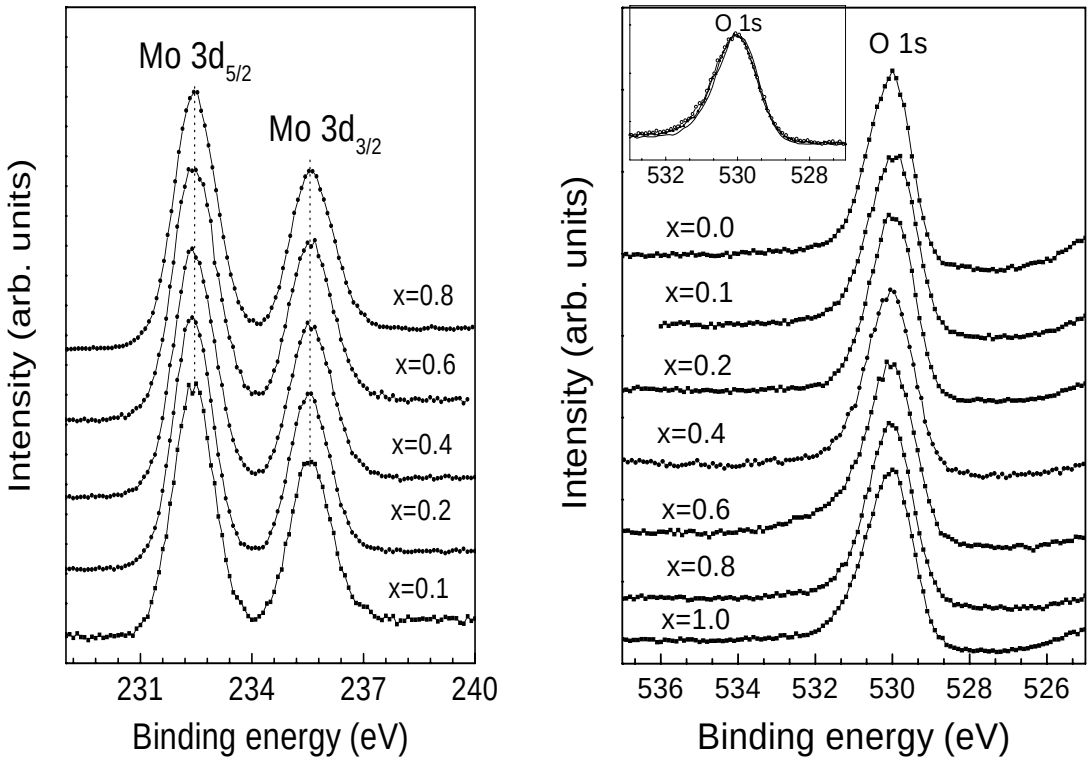

Figure 5.10: The XPS Mo 3d (left) and O 1s (right) spectra of $V_{2-x}Mo_xO_5$.

ions are present. The intensity of the shoulder at 516 eV increases with the Mo doping and its corresponding binding energy is very close to that of the V $2p_{3/2}$ peak of VO_2 (where the vanadium ions appear as V^{4+}). Therefore, we attribute the maximum at 517 eV and the shoulder at $\sim$ 516 eV to the V^{5+} and V^{4+} ions, respectively, and conclude that by Mo doping the partial reduction of the V^{5+} to V^{4+} ions takes place.

For a similar compound, $Na_xV_2O_5$ it has been shown that each additional positive charge added to the V_2O_5 lattice by the Na doping switches one V^{5+} ion to V^{4+} [110]. In our case a good quantitative analysis of the V 2p spectra is not possible due to the poor quality of the powder samples. For example, in the case of $V_{1.2}Mo_{0.8}O_5$ the V^{4+}/V^{5+} ratio is less than 2 and not 2 : 1, as we would expect by taking into account the former assumption. We explain this by the strong surface oxidation in the case of polycrystalline samples. In the inset of Fig. 5.11 one can see a very big difference in the V 2p XPS spectra of the same compound,

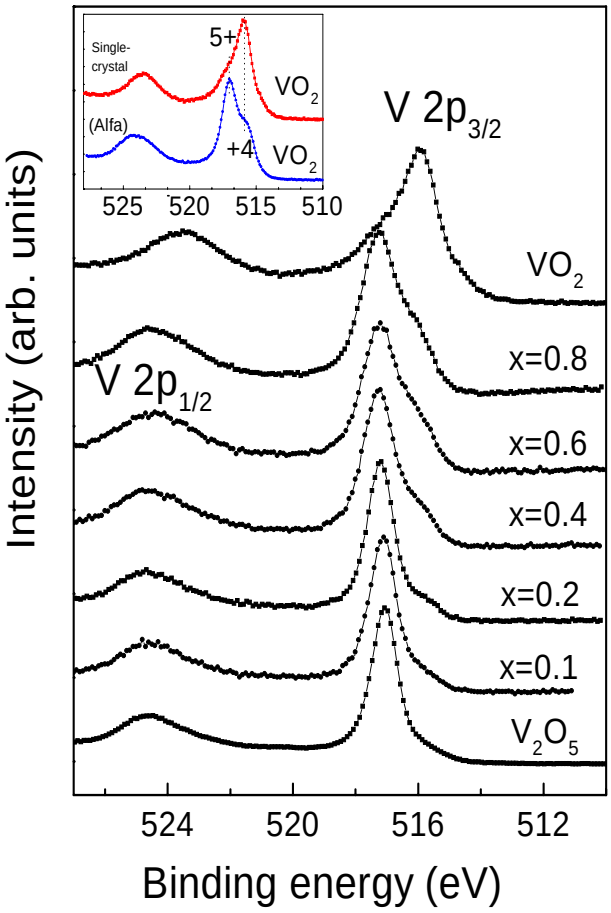

Figure 5.11: XPS V $2p$ spectra of the solid solutions $V_{2-x}Mo_xO_5$ and the reference samples: VO_2 and V_2O_5 (powders provided by *Alfa*); in the inset: V $2p$ spectra of the reference compound VO_2: single crystal and powder (*Alfa*).

VO_2– single crystal and powder[3] samples. In the single crystal spectrum the V $2p_{3/2}$ line is rather narrow, with a maximum at ~ 516 eV, reflecting the V^{4+} $2p$ states and a low–intensity shoulder at higher binding energies, which corresponds to the V^{5+} ions (low surface oxidation effect). A completely different shape of the V $2p_{3/2}$ line is observed for the VO_2–polycrystalline sample: the maximum is in this case located at ~ 517 eV (V^{5+}). In the last case the oxidation effect appears to be extremely high and much attention has to be paid in analyzing the XPS spectra of the polycrystalline samples.

[3]provided by Alfa.

5.3.2 XPS valence band, V Lα, O Kα and Mo L$\beta_{2.15}$ XES spectra

The XPS valence band spectra of the $V_{2-x}Mo_xO_5$ (x= 0.1, 0.2, 0.4; 0.6, 0.8) solid solutions are presented in Fig. 5.12.

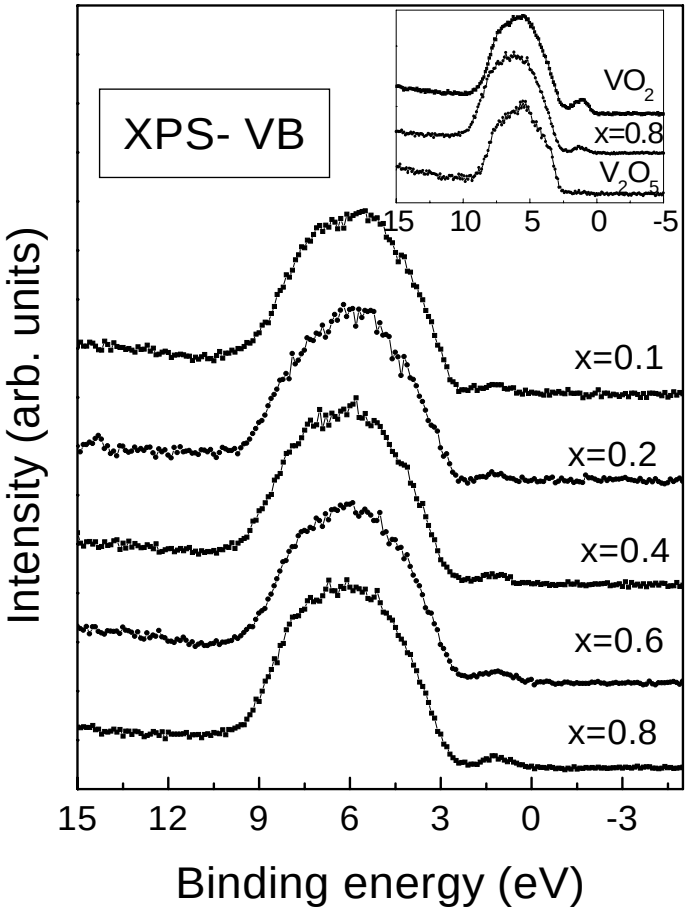

Figure 5.12: XPS valence band spectra of the solid solutions $V_{2-x}Mo_xO_5$; in inset: comparison of the VB spectrum of $V_{1.2}Mo_{0.8}O_5$ with the VB spectra of two reference compounds: VO_2 and V_2O_5.

All spectra are characterized by a wide band ($3 \div 9$ eV) and a low–intensity feature centered at ~ 1 eV. The shape of the broad band does not change with the Mo content, but the intensity of the low–energy feature is increasing with x for all investigated compounds. A comparison of the valence band spectrum of

$V_{1.2}Mo_{0.8}O_5$ with those of the reference compounds VO_2 and V_2O_5 is shown in the inset of Fig. 5.12. One can see that the small peak close to the Fermi level was not detected in the VB spectrum of V_2O_5 (V^{5+}, $3d^0$) and has the highest intensity for VO_2 (V^{4+}, $3d^1$).

The XPS valence band, Mo L$\beta_{2.15}$, V Lα and O Kα XES spectra of $V_{2-x}Mo_xO_5$ ($x = 0.4; 0.6$) are shown in Fig. 5.13. In order to identify the Mo $4d$, V $3d$ and O $2p$ partial contributions to the density of states, the XES Mo L$\beta_{2.15}$, V Lα and O Kα spectra were recorded. In this case the contribution of the surface layers is very small since XES mostly probes bulk electron states.

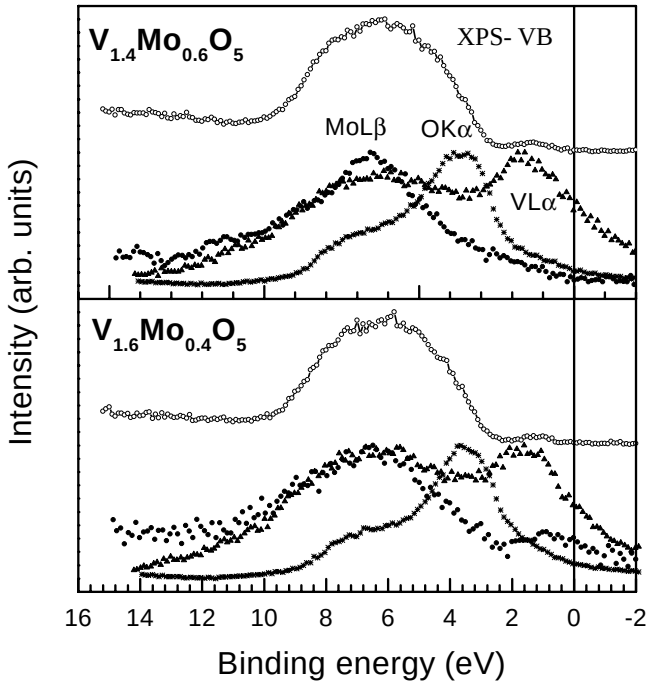

Figure 5.13: XPS valence band (○), XES Mo L$\beta_{2.15}$ (●), V Lα (▲) and O Kα (∗) spectra of the solid solutions $V_{2-x}Mo_xO_5$ ($x = 0.4, 0.6$).

The alignment of the Mo L$\beta_{2.15}$, V Lα and O Kα XES spectra on the binding energy scale was done using the Mo Lα_1 (2293.16 eV), Mo $3d_{5/2}$, O 1s and V $2p_{3/2}$ energetic positions. The shape and energetic position of the Mo L$\beta_{2.15}$ spectrum strongly depend on the valence state of the Mo atoms [31].

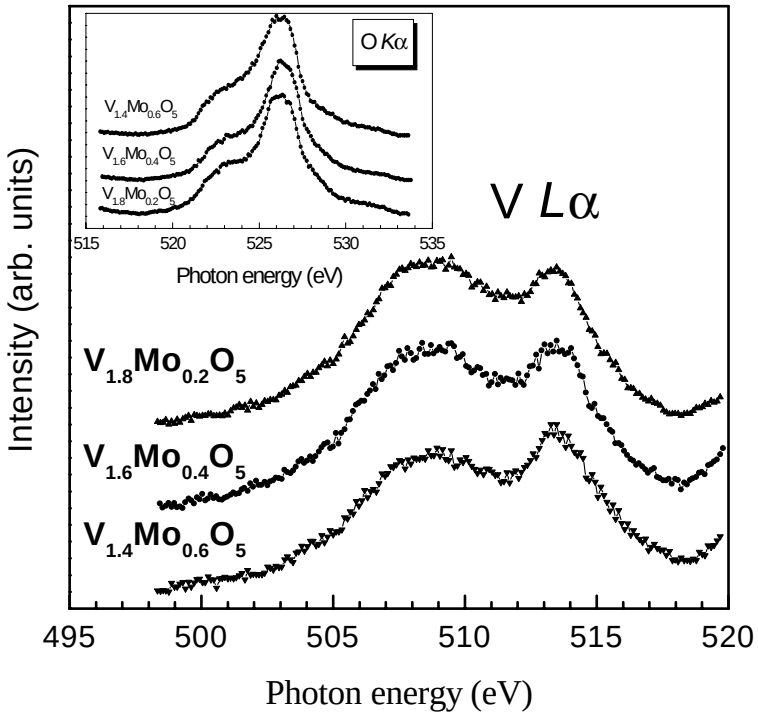

Figure 5.14: XES V Lα spectra of $V_{1.4}Mo_{0.6}O_5$ (▼), $V_{1.6}Mo_{0.4}O_5$ (●) and - $V_{1.8}Mo_{0.2}O_5$ (▲); in inset: the XES O Kα spectra of the same compounds.

In the case of $V_{1.4}Mo_{0.6}O_5$, the Mo L$\beta_{2,15}$ spectrum consists of only one band, reflecting the Mo 4*d*–states distribution in the occupied O 2*p*–like band due to the O 2*p*–Mo 4*d* hybridization. The second weak structure in the Mo L$\beta_{2,15}$ spectrum of $V_{1.6}Mo_{0.4}O_5$ situated at lower energies might indicate that only part of the additional electrons induced by the Mo doping are tranferred to vanadium, whereas some of them remain on the Mo atoms. This could be related to the changes in the crystal structure, from orthorhombic to monoclinic at $x = 0.4$ [85]. However, the Mo 3*d* XPS spectra of all investigated compounds are characterized by the same shape and binding energies. They are very similar to the Mo 3*d* XPS spectrum of MoO_3, indicating a $4d^0$ electronic configuration of the Mo ions.

The V Lα and O Kα XES spectra of $V_{1.4}Mo_{0.6}O_5$, $V_{1.6}Mo_{0.4}O_5$ and $V_{1.8}Mo_{0.2}O_5$ are presented in Fig. 5.14. The interpretation of the V Lα spectra is complicated

because the high–energy part overlaps with the V Lβ ($2p_{3/2} \rightarrow 3d4s$) spectra. However, one can observe a rise of the intensity in the high–energy band with x , which indicates an increase in the occupancy of the V $3d$ states, in agreement with the XPS results [43]. The O Kα XES spectra (inset in Fig. 5.14) do not change with composition.

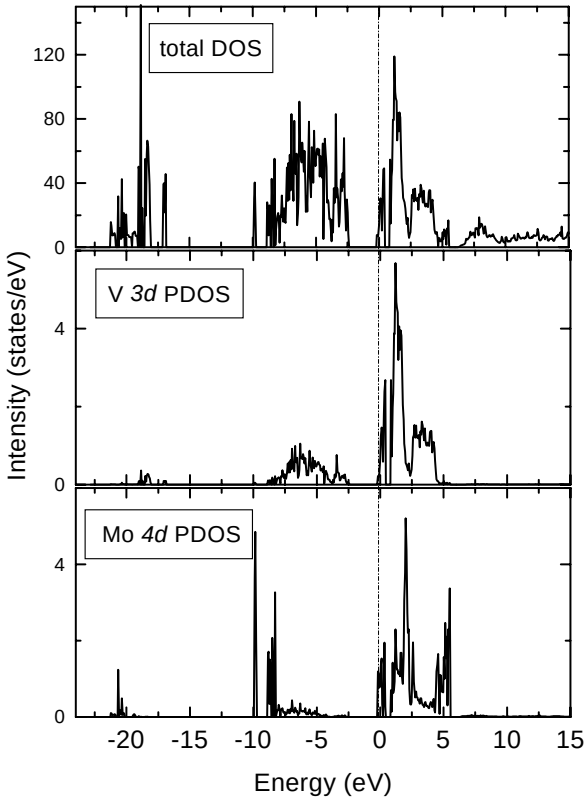

Figure 5.15: $V_{2-x}Mo_xO_5$: partial V $3d$ and Mo $4d$ density of states (PDOS) contributions together with total DOS per unit cell for the case of two Mo impurities.

The partial density of states (PDOS) corresponding to the local V $3d$ and Mo $4d$ contributions, as well as the total density of states (DOS) per unit cell, are shown in Fig. 5.15 for the case when two Mo impurities enter two different V–O warped planes and hence interact rather weakly.

The total DOS still resembles that of pure V_2O_5 with the lower (narrow) conduction band separated from the higher (broad) one. An additional quarter of

electron per formula unit provided by the Mo atoms shifts the Fermi level into the narrow conduction band. The distribution of the Mo $4d$ states in the valence band is, as compared to V $3d$, clearly ranging to lower energies. Simultaneously, the unoccupied Mo $4d$ states are somehow higher in energy than V $3d$. This reveals a stronger Mo–O hybridization and larger splitting into bonding and antibonding states, as compared to the V–O interaction, tendency that holds (apart from small variations related to the degree of localization of the Mo $4d$ states) for other two–impurity configurations studied.

On the basis of the XES results and band structure calculations we can reliably identify the structures of the XPS valence band: the wide band located at $3 \div 9$ eV is due to the O $2p$ states strongly hybridized with Mo $4d$ and V $3d$ states. The low–energy weak structure in the XPS valence band spectra arises from V $3d$ and Mo $4d$ contributions. Its intensity increases with the Mo doping and this reflects the increasing occupancy of the d–states.

Spectroscopic investigation of several vanadium oxides was performed by XPS and XES. Single crystals of V_2O_3, V_2O_5, VO_2, V_6O_{13}, V_4O_7 and V_3O_5 were available[4]. Our attention was focused on the mixed–valence oxides, which have been less investigated. New XPS results for V_6O_{13}, V_4O_7 and V_3O_5 in both phases, metallic and insulating, were reported. It was found that only small changes in the valence band spectra of the above systems occur through the metal–insulating transition. These changes are related to the V $3d$ bands, for which slight changes in the shape and width were observed. No detectable changes were found for the O $2p$ bands. The electronic structures for the mixed–valence oxides are characterized by significant V $3d$–O $2p$ hybridization, concluded from the comparison between the XPS and XES data.

The $V_{2-x}Mo_xO_5$ solid solutions were investigated by X–ray photoelectron and X–ray emission spectroscopy. The core levels analysis revealed that the V^{4+} content increases in the $V_{2-x}Mo_xO_5$ series when x increases. The X–ray emission measurements allowed us to localize the Mo $4d$, V $3d$ and O $2p$ contributions in the valence band. During Mo doping, the density of states just below Fermi level

[4]Prof. W. Reichelt from University of Dresden is acknowledged for providing the single crystals.

is enhanced. The V $3d$ and Mo $4d$ states were found to be responsible for the density of states close to Fermi level. Strong hybridization of the O $2p$, V $3d$ and Mo $4d$ states was experimentally observed and supported by band structure calculations.

Chapter 6

Cu–doped magnesium oxides

Here we present a spectroscopic study of the $Mg_{1-x}Cu_xO$ compounds by using XPS and XES techniques [55]. The core level XPS spectra are used to obtain information about the Cu $3d$–O $2p$ bonding character, in relation to the more investigated CuO system. The comparison between XPS valence band and XES spectra gives the possibility to establish the partial copper and oxygen contributions to the total density of states.

6.1 XPS Cu $2p$ and Cu $3s$ core level spectra

The XPS Cu $2p$ spectra of $Mg_{1-x}Cu_xO$ ($x = 0.1; 0.15; 0.2$)[1] are presented in Fig. 6.1. Besides the spin–orbit doublet, Cu $2p_{3/2}$ and Cu $2p_{1/2}$, all spectra exhibit broad satellite structures characteristic for the Cu^{2+} oxides. For comparison, the Cu $2p$ spectrum of CuO is shown. The main line Cu $2p_{3/2}$ is accompanied by a broad satellite ($939-945$ eV) with a fine structure that arises from the interaction between the $2p$ core hole, created during the XPS process, and the $3d^9$ electronic configuration in the final state of photoemission [183].

The main lines are associated to the $c^{-1}d^{10}L^{-1}$ states, whereas the satellites are mainly described by $c^{-1}d^9$. L^{-1} and c^{-1} denote holes on the $2p$ level of oxygen – due to the charge transfer from the ligand $2p$ to the Cu $3d$ level, and on the Cu $2p$ core level – created during the photoemission process, respectively.

[1] prepared by the solid–state reaction using commercial MgO and CuO powders.

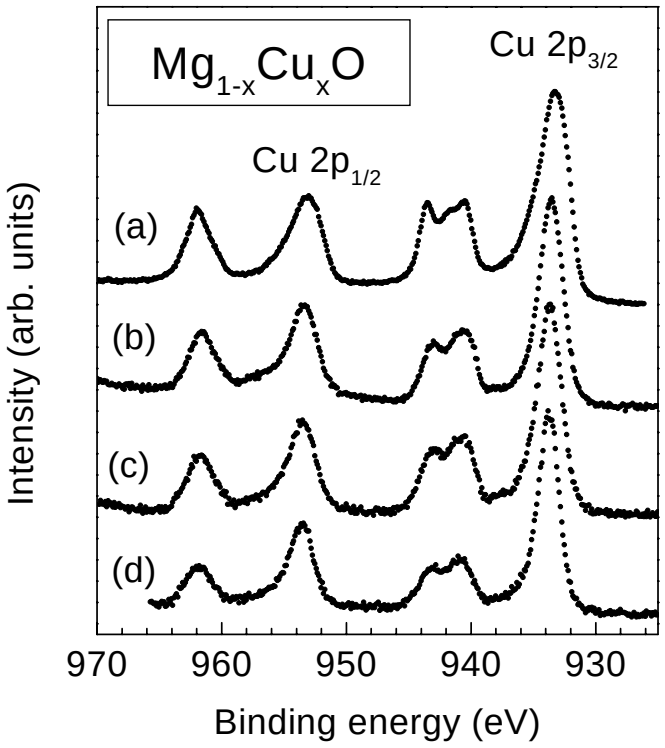

Figure 6.1: XPS Cu $2p$ spectra of CuO (a), $Mg_{0.8}Cu_{0.2}O$ (b), $Mg_{0.85}Cu_{0.15}O$ (c) and $Mg_{0.9}Cu_{0.1}O$ (d).

Fig. 6.2 shows the Cu $3s$ spectrum of $Mg_{0.8}Cu_{0.2}O$. The $3s$ splitting is related to the total spin of the $3d$ electrons in the ground state, as previously described in detail (see Chapter 2). In addition to the exchange interaction between the $3s$ hole and the $3d$ electrons, one also has to consider the charge–transfer process.

For the Cu^{2+} compounds, the $3s$ splitting is related only to the $3s^1d^9$ configuration, since there is no exchange splitting for a fully occupied d state ($3s^1d^{10}L^{-1}$). The theoretical spectrum shown in the same figure (6.2) was obtained by using the two–level model [55], in which the ground state wavefunction is considered as a linear combination of $3s^1d^{10}L^{-1}$ and $3s^1d^9$ final–state configurations. The main line is mainly due to $3s^1d^{10}L^{-1}$ and there is no splitting, as expected for a fully occupied d state. The satellite exhibits exchange splitting and corresponds to the $3s^1d^9$ configuration.

If we compare the Cu $3s$ spectrum of $Mg_{0.8}Cu_{0.2}O$ with the similar spectrum

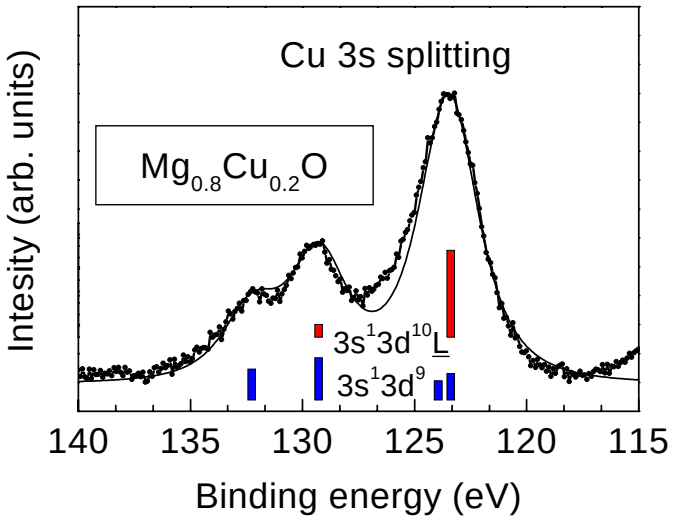

Figure 6.2: XPS Cu $3s$ spectrum (•) of $Mg_{0.8}Cu_{0.2}O$ together with the theoretical spectrum (–); the intensity of the vertical lines is related to the relative contributions of the $3s^1d^{10}L^{-1}$ and $3s^1d^9L$ final–state configurations.

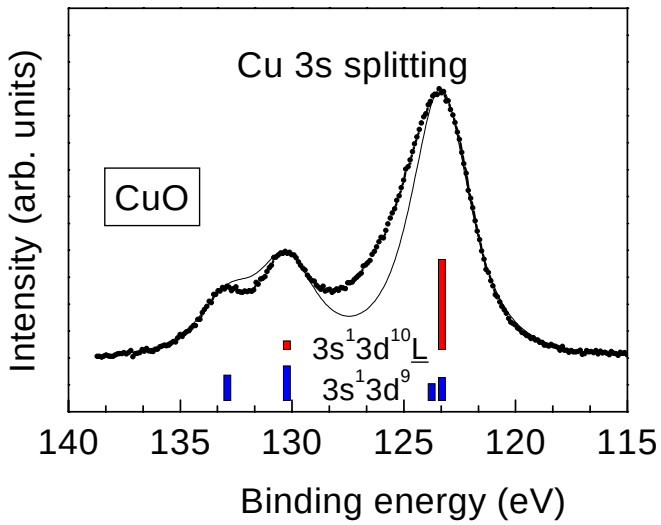

Figure 6.3: XPS Cu $3s$ spectrum (•) of CuO together with the theoretical spectrum (–); the intensity of the vertical lines is related to the relative contributions of the $3s^1d^{10}L^{-1}$ and $3s^1d^9L$ final–state configurations.

of CuO (see Fig. 6.3) one can observe that the energy difference between the main line and satellite is larger in the last case, due to the difference in the charge–transfer process. The same result was obtained by the two–level model [55], where formal 9.2 and 9.3 occupancies for the Cu $3d$ ground state was found for $Mg_{0.8}Cu_{0.2}O$ and CuO, respectively. This point out towards the more ionic character of the Cu–O bond in $Mg_{1-x}Cu_xO$, as compared to CuO.

6.2 XPS valence band and XES spectra

The XPS valence band spectra of $Mg_{1-x}Cu_xO$ ($x = 0.1; 0.15; 0.2$) are presented in Fig. 6.4. They exhibit similar three–peak structure (*a, b, c*) with the features maxima located at 4, 7.5 and 11.5 eV binding energies bellow Fermi level. In order to get information about the Cu, O and Mg partial contributions to the valence band, we have compared the XPS spectra with the Cu Lα and O Kα XES spectra. The 'subtracting' procedure was the following:

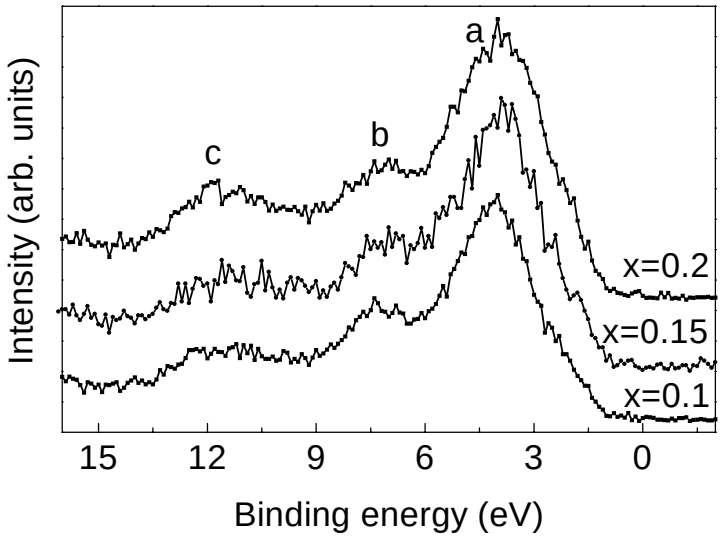

Figure 6.4: XPS valence band spectra of $Mg_{1-x}Cu_xO$ ($x = 0.1; 0.15; 0.2$).

$*$ In Fig. 6.5 the valence band spectra of $Mg_{1-x}Cu_xO$ ($x = 0.1; 0.2$) normalized to the O $2s$ intensity are shown. The shaded spectrum was obtained as difference between the spectra corresponding to $x = 0.2$ and $x = 0.1$. Since the spectra

were normalized to the O $2s$ peak, the difference spectrum corresponds mainly to the Cu $3d$ and Mg $3s, 3p, 3d$ states.

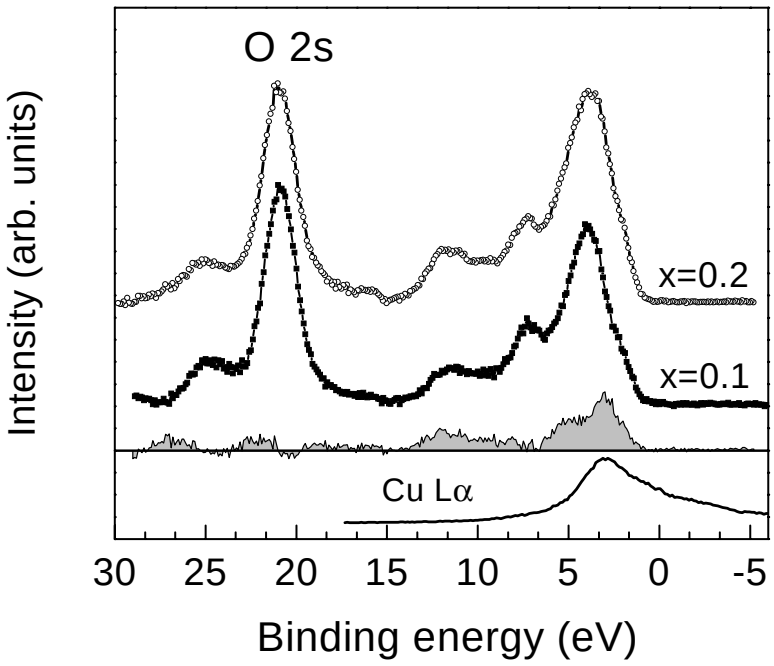

Figure 6.5: XPS valence band spectra of $Mg_{1-x}Cu_xO$ ($x = 0.1; 0.2$) together with the Cu Lα XES spectrum of $Mg_{0.8}Cu_{0.2}O$; the 'difference' spectrum (shaded area) was obtained as difference between the valence band spectra of $x = 0.1$ and $x = 0.2$, normalized to the O $2s$ intensity.

Taking into account the very small cross–sections of Mg $3s, 3p, 3d$ as compared to those of the Cu $3d$ states, one can neglect the Mg states contribution to the difference spectrum. Therefore, we can consider that the difference spectrum obtained by this 'substracting' procedure gives information about the Cu $3d$ contribution to the valence band. This is supported by the fact that the maximum of the Cu Lα XES spectrum of $Mg_{0.8}Cu_{0.2}O$, which gives the Cu $3d$ contribution to the VB, is located at the same binding energy as the maximum intensity of the 'difference' spectrum.

$*$ A similar procedure was followed to obtain the 'difference' spectrum from Fig. 6.6, but in this case the spectra were normalized to the Cu $3p$ intensity. Hence, one expects in this case information about the hybridization between the

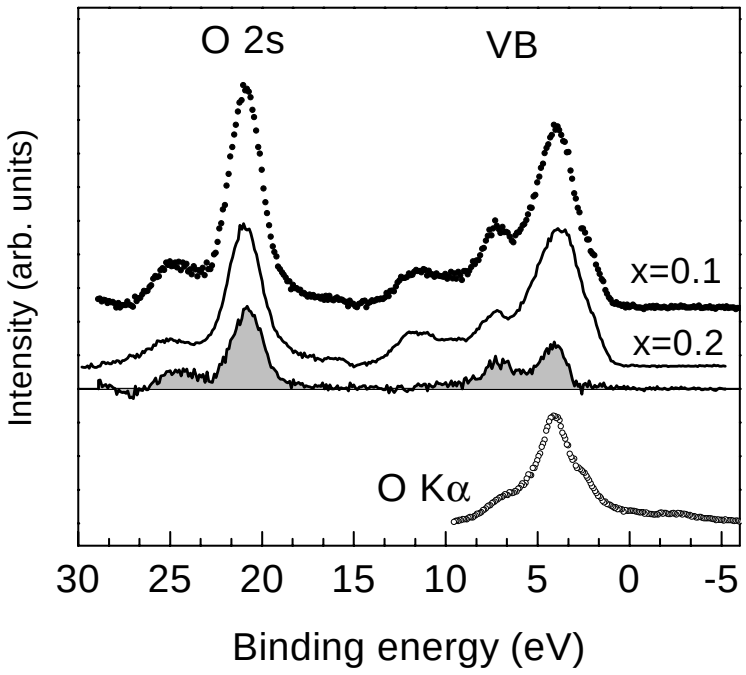

Figure 6.6: XPS valence band spectra of $Mg_{1-x}Cu_xO$ ($x = 0.1; 0.2$) together with the O Kα XES spectrum for $x = 0.2$; the 'difference' spectrum (shaded area) was obtained as difference between the VB spectra of $x = 0.1$ and $x = 0.2$, normalized to the Cu $3p$ intensity.

oxygen and magnesium states. The difference spectrum has double structure and the two peaks are located at the same binding energies as in the O Kα XES spectrum (see Fig. 6.6). It is also similar to the valence band XPS spectrum of MgO obtained by [91].

The O Kα XES spectra for the investigated solid solutions, $Mg_{1-x}Cu_xO$ ($x = 0.1; 0.15; 0.2$) are shown in Fig. 6.7. The highest peak is mainly due to O $2p$ hybridized with Mg $3p$ states, whereas the second peak of lower intensity is associated with the O $2p$ hybridized with Mg $3s$ states. In the inset of Fig. 6.7 the CuO O Kα XES spectrum is compared with the difference spectrum obtained by subtracting the O Kα spectrum for $x = 0.0$ (MgO) from the O Kα spectrum for $x = 0.15$ (both normalized to the highest intensity). The difference spectrum reflects the partial contribution of the O $2p$ states to the Cu–O bond.

If we compare this spectrum with the O Kα XES spectrum of CuO, one can

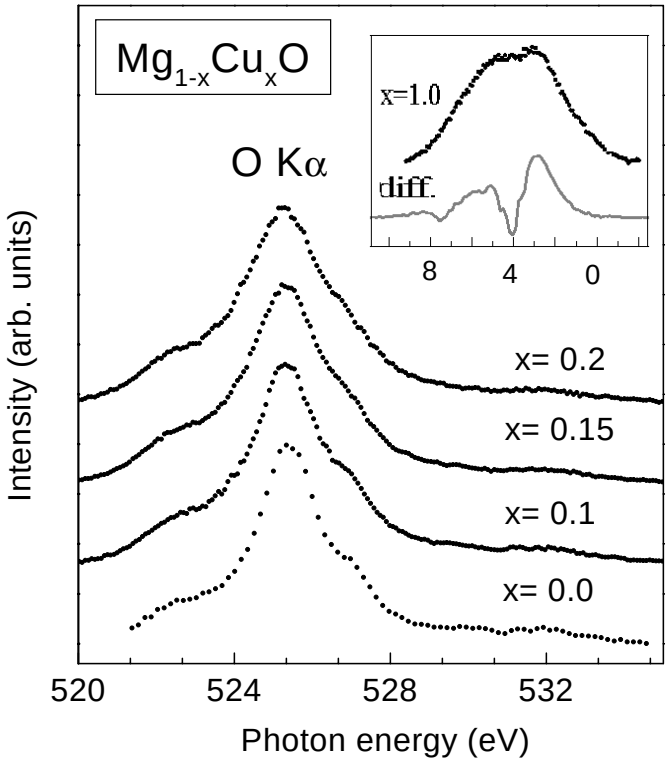

Figure 6.7: XES O Kα spectra of $Mg_{1-x}Cu_xO$ ($x = 0.0; 0.1; 0.15; 0.2$); in inset: XES O Kα spectrum of CuO and the 'difference' spectrum obtained as difference between the spectra corresponding to $x = 0.0$ and $x = 0.15$.

observe that the two features of the CuO O Kα XES spectrum correspond to the same energies as the peaks of the difference spectrum. It seems that, for this type of compounds, the crystal structure that is monoclinic for CuO and of NaCl type for $Mg_{1-x}Cu_xO$ is not an important factor that determines the electronic structure.

In this chapter, we presented an X–ray photoelectron and X–ray emission spectroscopic study of copper–doped magnesium oxide, in order to get information about the changes induced in the electronic structure of the parent compound MgO by the Cu doping in the range of $10 \div 20$ %.

The XPS Cu $2p$ and Cu $3s$ core levels were analyzed and from the exchange splitting of the $3s$ states the character of the Cu $3d$–O $2p$ bond in $Mg_{1-x}Cu_xO$

was discussed in relation to the reference compound CuO [55]. It was found that the Cu $3d$ occupancy in $Mg_{1-x}Cu_xO$ is less than in CuO. The Cu $3d$–O $2p$ bond nature in the investigated solid solutions is more ionic than in CuO.

By comparing the XPS valence band with the Cu Lα and O Kα XES spectra, the relative contributions of the Cu $3d$ and O $2p$ states were established. The type of crystal structure appears to be not an important factor that determines the formation of the Cu $3d$ and O $2p$ electronic distributions, since for $Mg_{1-x}Cu_xO$, the partial Cu $3d$ and O $2p$ states in the Cu–O bonding are similar with those corresponding to CuO.

Chapter 7

Conclusions and outlook

The aim of the present study was to investigate the electronic structure of some materials that have regained a huge interest in the last couple of years due to their very interesting electronic and magnetic properties. At the end of this spectroscopic investigation, the following conclusions can be drawn:

◇ *Manganese perovskites*

The role of the La–substitutions by Sr, Ba (Eu), Ca and Pb was discussed and the influence of the different dopants on the electronic structure has been determined. By comparing the XPS and XES data, the Mn $3d$ and O $2p$ states have been localized in the valence band; for all investigated samples, a strong hybridization of the Mn $3d$ and O $2p$ states was found, in good agreement with band structure calculations.

New XPS results of the single crystals $La_{1-x}Sr_xMnO_3$ ($x < 0.3$) have been presented. For the Sr–doped samples, $x < 0.3$, we have found no changes in the Mn $3s$ splitting, which suggest that the doping holes have mainly O $2p$ character. Very recently, a high interest has appeared in La–site and Mn–site doped compounds. The XPS data of the single crystals $La_{1-x}Ba_xMn_{1-y}Co_yO_3$, reported for the first time in the present study, suggest the divalent character of the Co ions, in agreement with the magnetic results previously obtained for the same samples.

◇ *Chromium chalcogenide spinels*

A special attention was paid to the $Fe_{1-x}Cu_xCr_2S_4$ ($x = 0.0; 0.5$) compounds, not only because they were recently reported as exhibiting CMR effect close to

room temperature, but also in order to investigate the long–standing controversy related to the Cu valence in these systems, which should be clarified now by the results reported for the first time in the present study. For this purpose, single crystals were investigated since, as shown here, the results for polycrystalline materials can lead to wrong spectra and, therefore, to a misinterpretation of the experimental data.

From a careful analysis of the Cu $2p$ and Cu $3s$ spectra, we have concluded that in $Fe_{1-x}Cu_xCr_2S(Se)_4$ ($x = 0.0; 0.5; 1.0$) the Cu ions are in the Cu^{1+} state, in agreement with the Lotgering model [106, 107].

Additional information about the electronic configurations of the constituent ions was obtained from other XPS core level spectra (Cu $2p$, S $2p$, Fe $2p$, Fe $3s$, Cr $2p$ and Cr $3s$). For $FeCr_2S_4$, the values of the Fe $3s$ and Cr $3s$ splittings correspond to the $3d^6$ and $3d^3$ electronic configurations of the Fe and Cr ions, respectively.

Furthermore, making use of the XPS and XES techniques, we have determined the partial contributions of the constituent ions in the valence band. The experimental data were found to be in excellent agreement with *ab-initio* TB–LMTO band structure calculations [95]. For $FeCr_2S_4$, the valence band consists of Fe $3d$, Cr $3d$ and S $3p$ states. The Cr $3d$ states were found to be less localized than the Fe $3d$ states. On going from $FeCr_2S_4$ to $Fe_{0.5}Cu_{0.5}Cr_2S_4$, no significant changes in the Cr $3d$ and Fe $3d$ states distribution were observed. The Cu $3d$ states were identified just below the Cr $3d$ states.

The similar Cr $3s$ splitting for the investigated compounds, $ACr_2S(Se)_4$ (A= Fe, Mn, Zn, Cd, Hg) suggests the same electronic configuration of the Cr ions ($3d^3$), although they have different electronic and magnetic properties.

The well resolved Cr $2p$ splitting in all investigated sulfides and selenides could be an indication of the localized character of the Cr magnetic moments. Its value corresponds to a $3d^3$ electronic configuration of the Cr^{3+} ions. A local magnetic moment of $\sim 3\mu_B$ was determined from the present XPS data, in very good agreement with the previously reported magnetic data.

◇ *Vanadium oxides*

Our attention was mainly focused on the mixed–valence oxides, which have

been less investigated up to now. In order to use them as references, the widely studied compounds: V_2O_3, V_2O_5 and VO_2 were also investigated. New XPS results for V_6O_{13}, V_4O_7 and V_3O_5 in both phases, metallic and insulating, were reported. It was found that only small changes in the valence band spectra of the above systems occur through the metal–insulating transition. These changes are related to the V $3d$ bands, for which slight changes in the shape and width were observed. No detectable changes were found for the O $2p$ bands. The electronic structures for the mixed–valence oxides are characterized by significant V $3d$–O $2p$ hybridization, as concluded from the comparison between the XPS and XES data.

The solid solutions $V_{2-x}Mo_xO_5$ were investigated by X–ray photoelectron and X–ray emission spectroscopy. The core levels analysis revealed that the V^{4+} content increases in the $V_{2-x}Mo_xO_5$ series when x increases. The X–ray emission measurements allowed us to localize the Mo $4d$, V $3d$ and O $2p$ contributions in the valence band. During Mo doping, the density of states just below the Fermi level is enhanced. The V $3d$ and Mo $4d$ states were found to be responsible for the density of states close to the Fermi level. Strong hybridization of the O $2p$, V $3d$ and Mo $4d$ states was experimentally observed and supported by band structure calculations.

◇ *Copper–doped magnesium oxides*

The XPS Cu $2p$ and Cu $3s$ core levels of the solid solutions $Mg_{1-x}Cu_xO$ ($x = 0.1; 0.15; 0.2$) were analysed. From the exchange splitting of the Cu $3s$ states the character of the Cu $3d$–O $2p$ bond in $Mg_{1-x}Cu_xO$ was determined and discussed in relation to the reference compound, CuO [55]. It was found that the Cu $3d$ occupancy in $Mg_{1-x}Cu_xO$ is less than in CuO. The Cu $3d$–O $2p$ bond nature in the investigated solid solutions is more ionic than in CuO.

By comparing the XPS valence band with the XES Cu Lα and O Kα spectra, the relative contributions of the Cu $3d$ and O $2p$ states were established. The type of the crystal structure appears to be not an important factor that determines the formation of the Cu $3d$ and O $2p$ electronic distributions, since for $Mg_{1-x}Cu_xO$ the partial Cu $3d$ and O $2p$ states in the Cu–O bonding are similar with those corresponding to CuO.

Outlook

Further investigation of the studied systems are required, as proposed below:

In the case of Mn–perovskites, several other $La_{1-x}Ba_xMn_{1-y}TM_yO_3$ single-crystals are now available. New XPS measurements and additional XES spectra are necessary in order to obtain a clear picture of their electronic structures.

Single–crystals of $CuCr_2S_4$ are in preparation at the University of Katowice. Although we do not expect a different shape in the Cu $3s$ spectrum of this system, as compared to the investigated $CuCr_2Se_4$, it would be worthwhile to perform new XPS measurements in order to further clarify the Cu valence. To elucidate the Cu electronic configuration for the intermediate doping regime, single crystals of $Fe_{1-x}Cu_xCr_2S_4$ ($0.0 < x < 0.5$ and $0.5 < x < 1.0$) are in preparation.

Due to the very small sizes of the available vanadium oxides the present investigation has been limited. For the further study of the metal–insulator transition large good–quality single crystals are required.

Acknowledgements

In the first place I would like to thank apl. Prof. Dr. Manfred Neumann for guiding me through this work. His help in the interpretation of the experimental results, his insights and discussions have been invaluable. Special thanks for his constant support and encouragement.

I am indebted to Prof. Dr. G. Borstel for giving me the possibility to study at the University of Osnabrück, Faculty of Physics (Graduiertenkolleg).

I am very grateful to Prof. M. Coldea and Prof. E. Burzo for their support since I was student at the 'Babes–Bolyai' University of Cluj–Napoca. I would like to believe that I did not disappoint their expectations. My special thanks to Prof. Coldea for our fruitful and enjoyable collaboration, for the advice and discussions during his visits in Osnabrück.

Much of this work has been made possible thanks to Prof. M. Neumann collaborations with scientists from Institute of Metal Physics, Ekaterinburg (Russia), Silesian University of Katowice (Poland) and Institute of Applied Physics, Chisinau (Moldova).

I thank Prof. E. Z. Kurmaev and his co-workers for our fruitful collaboration and for their hospitality during my visit in Ekaterinburg. Dr. V. M. Cherkashenko is acknowledged for performing the XES measurements for vanadium oxides. Very special thanks to Dr. V. R. Galakhov with whom most of the work presented in Chapters 3 and 6 was performed.

I would like to thank Dr. V. Tsurcan for our collaboration and the discussions we had in order to interpret the experimental results presented in Chapter 4.

Many thanks to the ESCA laboratory members from the University of Katowice for the assistance in performing the low–temperature XPS measurements

of the vanadium oxides and for their hospitality during my visits there. I was very fortunate to meet Prof. Dr. Ewa Talik, who became a dear friend: my very special thanks to you.

Dr. A. V. Postnikov is grateful acknowledged for performing the theoretical calculations for the chromium spinels and vanadium oxides, presented in Chapters 4 and 5.

I want to thank my colleagues: Daniela Hartmann, Sorin Chiuzbăian, Vasile Caciuc, Bernd Schneider, Werner Dudas, Stefan Bartkowski, Markus Bach, Franz Fangmeyer, Karsten Küpper, Bolormaa Sanduijav and also the former colleagues, Dr. Stefan Plogmann, Dr. Helmut Schürmann and Dr. Ingo Karla for the nice time we have spent together.

My special thanks to Sorin for being a good friend. Vasile is acknowledged for reading the manuscript and helping me to solve many Latex problems. Many thanks to Daniela for her kindness and helping me so much, especially at the beginning of my stay in Osnabrück, and to Bernd for reading the manuscript.

Dr. Viorica Simon from the 'Babes–Bolyai' University of Cluj–Napoca is acknowledged for a critical read of the manuscript.

During my stay in Osnabrück I was lucky to meet very kind people. I would like to use this opportunity to thank Mrs. U. Schöler and her family for their support and friendship that meant so much to me.

At last, but not least, I am grateful to Claudiu and my family for their love and for being with me every single moment–although so many hundred kilometers were between us. Without them I wouldn't have the power to pass over difficult moments and, implicitly, this work would not come to an end.

Bibliography

[1] M. Abbate, F. M. F. de Groot, J. C. Fuggle, A. Fujimori, Y. Tokura, Y. Fujishima, O. Strebel, M. Domke, J. van Elp, B. T. Thole, G. A. Sawatzky, and M. Sacchocand N. Tsuda, *Soft X–ray–absorption studies of the location of extra charges induced by substitution in controlled–valence materials*, Phys. Rev. B **44** (1991), no. 11, 5419–5422.

[2] M. Abbate, H. Pen, M. T. Czyzyk, F. M. F. de Groot, J. C. Fuggle, Y. J. Ma, C. T. Chen, F. Sette, A. Fujimori, Y. Ueda, and K. Kosuge, *Soft X–ray absorption of vanadium oxides*, J. Electron Spectrosc. Relat. Phenom. **62** (1993), 185–195.

[3] D. Adler, *Mechanisms for metal–nonmetal transitions in transition–metal oxides and sulfides*, Rev. Mod. Phys **40** (1968), no. 4, 714–736.

[4] F. Aebi, *Phasenuntersuchungen im System Vanadin–Sauerstoff und die Krystallstruktur von* $V_{12}O_{26}$, Helv. Chim. Acta **31** (1948), no. 1, 8–21.

[5] P. W. Anderson, Phys. Rev. **115** (1959), 2.

[6] P. W. Anderson and H. Hasegawa, *Considerations on double–exchange*, Phys. Rev. **100** (1955), no. 2, 675–684.

[7] V. I. Anisimov, A. I. Poteryaev, M. A. Korotin, A. O. Anokhin, and G. Kotliar, J. Phys.: Condens. Matter **9** (1997), 7359.

[8] V. I. Anisimov, J. Zaanen, and O. Andersen, Phys. Rev. B **44** (1991), 943.

[9] V. N. Antonov, V. P. Antropov, B. N. Harmon, A. N. Yaresko, and A. Ya. Perlov, *Fully relativistic spin–polarized LMTO calculations of the magneto–optical Kerr effect of d and f ferromagnetic materials. I. Chromium spinel chalcogenides*, Phys. Rev. B **59** (1999), no. 22, 14552–14560.

[10] H. Asano, J. Hayakawa, and M. Matsui, *Giant magnetoresistance of a two–dimensional ferromagnet* $La_{2-2x}Ca_{1+2x}Mn_2O_7$, Appl. Phys. Lett. **68** (1996), 338–340.

[11] S. Atzkern, S. V. Borisenko, M. Knupfer, M. S. Golden, J. Fink, A. N. Yaresko, V. N. Antonov, M. Klemm, and S. Horn, *Valence–band excitations in* V_2O_5, Phys. Rev. B **61** (2000), no. 19, 12792–12798.

[12] M. N. Baibich, J. M. Broto, A. Fert, Nguyen Van Dau, F. Petroff, P. Etienne, G. Creuzet, A. Friederich, and A. Chazelas, *Giant magnetoresistance of (001)Fe/(001)Cr magnetic superlattices*, Phys. Rev. Lett. **61** (1988), no. 21, 2472–2475.

[13] P. K. Baltzer, P. J. Wojtowicz, M. Robbins, and E. Lopatin, *Exchange interactions in ferromagnetic chromium chalcogenide spinels*, Phys. Rev. **151** (1966), 367.

[14] D. Barreca, A. Rizzi, and E. Tondello, *Vanadium pentoxide thin films by XPS*, Surf. Sci. Spectra **6** (1999), no. 3, 168–176.

[15] C. Battistoni and E. Paparazzo, *X–ray photoelectron spectra of the spinel systems* $CdCr_xIn_{2-x}S_4$ *and* $ZnCr_xAl_{2-x}S_4$, Solid State Communic. **46** (1983), no. 4, 333–336.

[16] P. D. Battle, S. J. Blundell, M. A. Green, W. Hayes, M. Honold, A. K. Klehe, N. S. Laskey, J. E. Millburn, L. Murphy, M. J. Rosseinsky, N. A. Samarin, J. Singleton, N. E. Sluchanko, S. P. Sullivan, and J. F. Vente, *Colossal magnetoresistance in* $Sr_{2-x}Nd_{1+x}Mn_2O_7$ *(*x*=* 0.0*;* 0.1*)*, J. Phys.: Condens. Matter **8** (1996), no. 32, L427–434.

[17] N. B. Bebenin, N. N. Loshkareva, Yu. P. Sukhorukov, A. P. Nossov, R. I. Zainullina, V. G. Vassiliev, B. V. Slobodin, K. M. Demchuk, and V. V. Ustinov, *Charge carriers in* $La_{0.67-x}Y_xBa_{0.33}MnO_3$, Solid State Communic. **106** (1998), no. 6, 357–361.

[18] N. G. Bebenin, R. I. Zainullina, V. V. Mashkatsan, A. M. Burkhanov, and V. V. Ustinov, *The Hall effect in* $La_{0.67}Ba_{0.33}MnO_3$, J. Experim. Theoret. Phys. **86** (1998), no. 3, 534–537.

[19] C. N. Berglund and W. E. Spicer, Phys. Rev. **136 A** (1964), 1030.

[20] A. Bianconi, *Multiplet splitting of final–state configurations in X–ray absorption spectrum of* VO_2*: effect of core–hole screening, electron correlation and metal–insulator transition*, Phys. Rev. B **26** (1982), no. 6, 2741–2747 (and the references therein).

[21] G. Borstel, *Theoretical aspects of photoemission*, Appl. Phys. A **38** (1985), 193–204 (and the references therein).

[22] D. Briggs and M. P. Seah, *Practical Surface Analysis by Auger and X–ray Photoelectron Spectroscopy*, John Wiley & Sons, 1983.

[23] W. Brückner, H. Oppermann, W. Reichelt, J. I. Terukow, F. A. Tschudnowski, and E. Wolf, *Vanadiumoxide: Darstellung, Eigenschaften, Anwendung*, Akademie–Verlag, Berlin, 1983.

[24] C. R. Brundle and A. D. Baker, *Electron Spectroscopy: Theory, Techniques and Applications*, John Wiley & Sons, Bristol, 1979.

[25] D. W. Bullet, *The energy band structure of* V_2O_5*: a simpler theoretical approach*, J. Phys. C: Solid State Phys. **13** (1980), L595–599.

[26] A. Byström, K. A. Wilhelmi, and O. Brotzen, Acta Chem. Scand. **4** (1950), 1119–1130.

[27] C. Castellani, C. R. Natoli, and J. Ranninnger, Phys. Rev. B **18** (1978), 4945.

[28] A. Chainani, M. Mathew, and D. D. Sarma, *Electronic spectroscopic investigation of the semiconductor–metal transition in* $La_{1-x}Sr_xMnO_3$, Phys. Rev. B **47** (1993), no. 23, 15397–15403.

[29] A. Chakrabarti, K. Hermann, R. Druzinic, M. Witko, F. Wagner, and M. Petersen, *Geometric and electronic structure of vanadium pentoxide: a density functional bulk and surface study*, Phys. Rev. B **59** (1999), no. 16, 10583–10589.

[30] J. Y. Chan, S. M. Kauzlarich, P. Klavins, R. N. Shelton, and D. J. Webb, *Colossal negative magnetoresistance in an antiferromagnet*, Phys. Rev. B **57** (1998), no. 14, R8103–8106.

[31] V. M. Cherkashenko, V. V. Shumilov, and G. V. Bazuev, *X–ray emission spectra and the electronic structure of* Y_2VMoO_7 *and* $SrV_{1-x}Mo_xO_3$ *solid solutions*, Russian J. of Inorg. Chem. **39** (1994), no. 7, 1132–1136.

[32] F. A. Chudnovskii, E. I. Terukov, and D. I. Khomskii, *Insulator–metal transition in* V_3O_5, Solid State Communic. **25** (1978), 573.

[33] J. M. D. Coey, M. Viret, and S. von Molnar, *Mixed–valence manganites*, Advances in Physics **48** (1999), no. 2, 167–293.

[34] A. Continenza, S. Massidda, and M. Posternak, *Self–energy corrections in* VO_2 *within a model GW scheme*, Phys. Rev. B **60** (1999), no. 23, 15699–15704.

[35] I. M. Curelaru, E. Suoninen, and E. Minni, *An APS–XPS study of vanadium pentoxide*, J. Chem. Phys. **78** (1983), no. 5, 2262–2267.

[36] B. Dabrowski, K. Rogacki, X. Xiong, P. W. Klamut, R. Dybzinski, J. Shaffer, and J. D. Jorgensen, *Synthesis and properties of the vacancy–free* $La_{1-x}Ba_xMnO_3$, Phys. Rev. B **58** (1998), no. 5, 2716–2723.

[37] S. Dai, Z. W. Li, A. H. Morrish, X. Z. Zhou, J. G. Zhao, and X. M. Xiong, *Colossal magnetoresistance in* $(La_{0.7}Sn_{0.3})_2Mn_2O_7$, Phys. Rev. B **55** (1997), no. 21, 14125–14128.

[38] L. Darcy, P. K. Baltzer, and E. Lopatin, *Magnetic and crystalographic properties of the system $MnCr_2S_4$–$MnInCr_2S_4$*, J. Appl. Phys. **39** (1968), 898–899.

[39] J. H. de Boer and E. J. W. Verway, Proc. Phys. Soc. London **A 49** (1937), 59.

[40] P. G. de Gennes, *Effects of double exchange in magnetic crystals*, Phys. Rev. **118** (1960), no. 1, 141–154.

[41] F. M. F. de Groot, *X–ray absorption of transition metal oxides*, Ph.D. thesis, Catolic University of Nijmegen, 1991.

[42] W. Dekeyser, L. Fiermans, G. Vanderkelen, and J. Vennik, *Electron Emission Spectroscopy*, D. Reidel Publishing Company, Dordrecht–Holland, 1973.

[43] M. Demeter, St. Bartkowski, E. Z. Kurmaev, M. Neumann, V. M. Cherkashenko, V. L. Volkov, and G. C. Zakharova, *Investigation of the mixed–valent system $V_{2-x}Mo_xO_5$ by XPS*, SPIE **3724** (1999), 296–300.

[44] M. Demeter, M. Neumann, A. V. Postnikov, V. M. Cherkashenko, V. R. Galakhov, and E. Z. Kurmaev, *Electronic structure of the mixed–valent system $V_{2-x}Mo_xO_5$*, accepted for publication in Surf. Sci (2001).

[45] V. E. Dolgih, V. M. Cherkashenko, E. Z. Kurmaev, D. A. Goganov, E. K. Ovchinnikov, and Yu. M. Yarmoshenko, *X–ray fluorescent spectrometer with linear position sensitive detector*, Nucl. Instrum. Methods **224** (1984), 117.

[46] S. Doniach and M. Sŭnjić, *Many–electron singularity in X–ray photoemission and X–ray line spectra from metals*, J. Phys. C: Solid St. Phys. **3** (1970), 285–291.

[47] J. B. A. Elemans, B. van Laar, K. R. van der Veen, and B. O. Loopstra, J. Solid State Chem. **3** (1971), 238.

[48] I. S. Elfimov, V. I. Anisimov, and G. A. Sawatzky, *Orbital ordering, Jahn–Teller distorsion and anomalous X–ray scattering in manganates*, Phys. Rev. Lett. **82** (1999), no. 21, 4264–4267.

[49] V. Eyert and K. H. Höck, *Electronic structure of V_2O_5: role of octahedral deformations*, Phys. Rev. B **57** (1998), no. 3, 1316–1319.

[50] C. S. Fadley, S. B. M. Hagstroem, J. M. Hollander, M. P. Klein, and D. A. Shirley, *Chemical effects on core–electron binding energy in iodine and Europium*, J. Chem. Phys. **48** (1968), no. 8, 3779–3794.

[51] C. S. Fadley and D. A. Shirley, *Multiplet splitting of metal–atom electron binding energies*, Phys. Rev. A **2** (1970), no. 4, 1109–1120.

[52] A. Fert and C. Vouille, *Magnetoresistance overview: AMR, GMR, TMR, CMR: in Magnetische Schichtsysteme*, Schriften des Forschungszentrums Jülich, 1999, Band 2.

[53] L. Fiermans, R. Hoogewijs, and J. Vennik, *Electron spectroscopy of transition metal oxide surfaces*, Surf. Sci **47** (1975), 1–40.

[54] D. W. Fischer, *Vanadium $L_{II,III}$ X–ray emission and absorption spectra from metal oxides, nitride, carbide and boride*, J. of Appl. Phys. **40** (1969), no. 10, 4151–4163.

[55] V. R. Galakhov, L. D. Finkelstein, D. A. Zatsepin, E. Z. Kurmaev, A. A. Samokhvalov, S. V. Naumov, G. K. Tatarinova, M. Demeter, St. Bartkowski, M. Neumann, and A. Moewes, *Interaction of Cu 3d and O 2p states in $Mg_{1-x}Cu_xO$ solid solutions with NaCl structure: X–ray photoelectron and X–ray emission study*, Phys. Rev. B **62** (2000), no. 8, 4922–4926.

[56] V. R. Galakhov, A. I. Poteryaev, E. Z. Kurmaev, V. I. Anisimov, St. Bartkowski, M. Neumann, Z. W. Lu, B. M. Klein, and T. R. Zhao, *Valence–band spectra and electronic structure of $CuFeO_2$*, Phys. Rev. B **56** (1997), no. 8, 4584–4591.

[57] V. R. Galakhov, St. Uhlenbrock, St. Bartkowski, A. V. Postnikov, M. Neumann, L. D. Finkelstein, E. Z. Kurmaev, A. A. Samokhvalov, and L. I. Leonyuk, *X–ray photoelectron* $3s$ *spectra of transition metal oxides*, to be published.

[58] K. Ghosh, S. B. Ogale, R. Ramesh, R. L. Greene, T. Venkatesan, K. M. Gapshup, R. S. Bathe, and S. I. Patil, Phys. Rev. B **59** (1999), 533.

[59] P. K. Ghosh, *Introduction to photoelectron spectroscopy*, John Willey & Sons, New York/ Chicester/ Brisbane/ Toronto/ Singapore, 1983.

[60] J. B. Goodenough, *Theory of the role of covalence in the perovskite–type manganites [La,M(II)]*MnO_3, Phys. Rev. **100** (1955), no. 2, 564–573.

[61] ———, *Magnetic properties*, Landolt–Börnstein **II** (1962), no. 9, 187–219.

[62] ———, *Descriptions of outer d electrons in thiospinels*, J. Phys. Chem. Solids **30** (1969), 261–280.

[63] ———, J. Sol. State Commun. **3** (1971), 490.

[64] K. W. Goodman and V. E. Henrich, *Assignment of a photoemission feature in the O 2s–O 2p band gaps of* TiO_2 *and* V_2O_5, Phys. Rev. B **50** (1994), no. 15, 10450–10455.

[65] J. Gutiérez, A. Peña, J. M. Barandiarán, J. L. Pizzaro, L. Lezama, M. Insausti, and T. Rojo, *Structural, magnetic and magnetotransport properties of* $La_{0.7}Pb_{0.3}Mn_{0.9}TM_{0.1}O_3$ *(TM=Fe,Co,Ni)*, J. Phys.: Condens. Matter **12** (2000), no. 50, 10523–10534.

[66] G. H. Gweong, J. G. Park, and S. J. Oh, *Final–state screening effect in the* $3s$ *photoemission spectra of the Mn and Fe insulating compounds*, Phys. Rev. B **48** (1993), no. 11, 7825–7835.

[67] G. Haacke and L. C. Beegle, *Magnetic properties of the spinel system* $Fe_{1-x}Cu_xCr_2S_4$, J. Phys. Chem. Solids **28** (1967), 1699–1704.

[68] N. Hamada, H. Sawada, and K. Terakura, *Electronic band structure of* $La_{1-x}Ba_xMnO_3$, J. Phys. Chem. Solids **56** (1995), no. 12, 1719–1720.

[69] G. L. W. Hart, W. E. Pickett, E. Z. Kurmaev, D. Hartmann, M. Neumann, A. Moewes, D. L. Ederer, R. Endoh, K. Taniguchi, and S. Nagata, *Electronic structure of* $Cu_{1-x}Ni_xRh_2S_4$ *and* $CuRh_2S_4$*: band–structure calculations , X–ray photoemission and fluorescence measurements*, Phys. Rev. B **61** (2000), no. 6, 4230–4237.

[70] S. Hüfner, P. Steiner, M. Weirich, and R. Courths, *The Cu valence in the high* T_c*– superconductors and in monovalent, divalent and trivalent copper oxides determined from XPS core level spectroscopy*, Z. Phys. B **85** (1991), 43–48.

[71] Stefan Hüfner, *Photoelectron spectroscopy*, Springer–Verlag, Berlin Heidelberg, 1995.

[72] K. Hermann, M. Witko, R. Druzinic, A. Chakrabarti, B. Tepper, M. Elsner, A. Gorschlütter, H. Kuhlenbeck, and H. J. Freund, *Properties and identification of oxygen sites at the* V_2O_5 *(*010*) surface: theoretical cluster studies and photoemission experiments*, J. Electron Spectrosc. Relat. Phenom. **98–99** (1999), 245–255.

[73] J. M. Hollas, *High resolution spectroscopy*, Butterworths & Co, London, 1982.

[74] H. Horiuchi, M. Tokonami, N. Moritomo, and K. Nagasawa, *The crystal structure of* V_4O_7, Acta Cryst. B **28B** (1972), 1404–1410.

[75] J. Hubbard, Proc. R. Soc. London **276** (1963), 238.

[76] M. Imada, A. Fujimori, and Y. Tokura, *Metal–insulator transitions*, Rev. Mod. Phys. **70** (1998), no. 4, 1039–1263.

[77] H. A. Jahn, Proc. Roy. Soc. (London) **A 164** (1938), 117.

[78] H. A. Jahn and E. Teller, Proc. Roy. Soc. (London) **A 161** (1937), 220.

[79] S. Jin, T. H. Tiefel, M. McCormack, R. A. Fastnacht, R. Ramesh, and L. H. Chen, *Thousandfold change in resistivity in magnetoresistive La–Ca–Mn–O films*, Science **264** (1994), 413–415.

[80] G. H. Jonker, *Magnetic compounds with perovskite structure IV*, Physica **22** (1956), 707–710.

[81] H. L. Ju, H.-C. Sohn, and K. M. Krishnan, *Evidence for O 2p hole–driven conductivity in* $La_{1-x}Sr_xMnO_3$ *(*$0 < x < 0.7$*) and* $La_{0.3}Sr_{0.7}MnO_z$ *thin films*, Phys. Rev. Lett. **79** (1997), no. 17, 3230–3233.

[82] Ingo Karla, *Various energy scales in rare earth compounds: multimples, band energy gaps and crystal fields in RE nickel antimonides*, Ph.D. thesis, University of Osnabrück/ Université Joseph Fourier of Grenoble, 1999.

[83] J. Kasperkiewicz, J. A. Kovacich, and D. Lichtman, *XPS studies of vanadium and vanadium oxides*, J. Electron Spectrosc. Relat. Phenom. **32** (1983), 123–132.

[84] H. V. Keer and J. M. Honig, Mater. Res. Bull. **12** (1977), 277.

[85] L. Kihlborg, *The crystal structure of* $(Mo_{0.3}V_{0.7})_{0.2}O_5$ *of R–*Nb_2O_5 *type and a comparison with the structures of* V_2O_5 *and* V_2MoO_8, Acta Chem. Scand. **21** (1967), no. 9, 2495–2502.

[86] R. Kleinberger and R. Kouchkovsky, *Etude radiocristalographique à base température du spinelle* $ZnCr_2S_4$, Compt. Rend. **262** (1966), 628–630.

[87] W. Kohn, *Nobel Lecture: Electronic structure of matter–wave functions and density functionals*, Rev. Mod. Phys. **71** (1999), no. 5, 1253–1266.

[88] T. Koopmans, *Über die Zuordnung von Wellenfunktionen und Eigenwerten zu den eizelnen Elektronen einer Atoms*, Physica **1** (1933), 104–113.

[89] M. Kosuge, *The phase diagram and phase transition of the* V_2O_3*–*V_2O_5 *system*, J. Phys. Chem. Solids **28** (1967), 1613.

[90] A. Kowalczyk, A. Slebarski, A. Szajek, J. Baszynski, and A. Winiarski, *X–ray photoemission spectra of $La_{0.7}Sr_{0.3}MnO_3$*, J. Magn. Magn. Mat. **212** (2000), 107–111.

[91] S. P. Kowalczyk, *The electronic structure of $SrTiO_3$ and some simple related oxides (MgO, Al_2O_3, SrO, TiO_2)*, Solid State Communic. **23** (1977), 161–169.

[92] P. Kuiper, J. van Elp, G. A. Sawatzky, A. Fujimori, S. Hosoya, and D. M. de Leeuw, *Unoccupied density of states of $La_{2-x}Sr_xNiO_{4+\delta}$ studied by polarisation–dependent X–ray–absorption spectroscopy and bremsstrahlung isochromat spectroscopy*, Phys. Rev. B **44** (1991), no. 9, 4570–4575.

[93] E. Z. Kurmaev, V. M. Cherkashenko, Yu. M. Yarmoshenko, St. Bartkowski, A. V. Postnikov, M. Neumann, L.-C. Duda, J. H. Guo, J. Nordgren, V. A. Perelyaev, and W. Reichelt, *Electronic structure of VO_2 studied by X–ray photoelectron and X–ray emission spectroscopies*, J. Phys.: Condens. Matter **10** (1998), 4081–4091.

[94] E. Z. Kurmaev, V. V. Fedorenko, S. N. Shamin, A. V. Postnikov, G. Wiech, and Y. Kim, *Small–spot X–ray emission spectroscopy and its application for study of electronic structure and chemical bonding in solids*, Phys. Scr. T **41** (1992), 288–292.

[95] E. Z. Kurmaev, A. V. Postnikov, H. M. Palmer, C. Greaves, St. Bartkowski, V. Tsurkan, M. Demeter, D. Hartmann, M. Neumann, D. A. Zatsepin, V. R. Galakhov, S. N. Shamin, and V. Trofimova, *Electronic structure of $FeCr_2S_4$ and $Fe_{0.5}Cu_{0.5}Cr_2S_4$*, J. Phys. Chem. Solids **12** (2000), 5411–5421.

[96] E. Z. Kurmaev, J. van Ek, D. L. Ederer, L. Zhou, T. A. Callcott, R. C. C. Perera, V. M. Cherkashenko, S. N. Shamin, V. A. Trofimova, St. Bartkowski, M. Neumann, A. Fujimori, and V. P. Moloshag, *Experimental and theoretical investigation of the electronic structure of transition metal sulphides: CuS, $CuFe$ and $FeCuS_2$*, J. Phys.: Condens. Matter **10** (1998), 1687–1697.

[97] Y. Kuwata, S. Suga, S. Imada, A. Sekiyama, S. Ueda, T. Iwasaki, H. Harada, T. Moro, T. Fukawa, K. Ashida, H. Yoshioka, T. Terauchi, J. Sameshima, H. Kuwahara, Y. Moritomo, and Y. Tokura, *Electronic structures of $Nd_{1-x}Sr_xMnO_3$, $La_{1-x}Sr_xMnO_3$ and $La_{1-x}Ca_xMnO_3$ studied by photoemission and inverse photoemission spectroscopy*, J. Electron Spectrosc. Relat. Phenom. **88–91** (1998), 281–285.

[98] H. Kuzmany, *Solid state spectroscopy– an introduction*, Springer–Verlag, Berlin Heidelberg, 1998.

[99] W. Lambrecht, B. Djafari-Rouhani, M. Lannoo, P. Clauws, L. Fiermans, and J. Vennik, *The energy band structure of V_2O_5: II. Analysis of the theoretical results and comparison with experimental data*, J. Phys. C: Solid State Phys. **13** (1980), 2503–2517.

[100] Stefan Lütkehoff, *Untersuchung zur elektronischen Struktur Seltener Erdoxide mittels der Röntgenspektroskopie*, Ph.D. thesis, University of Osnabrück, 1997.

[101] H. W. Lehmann, *Semiconducting properties of ferromagnetic $CdCr_2S_4$*, Phys. Rev. **163** (1967), no. 2, 488–496.

[102] J. Z. Liu, I.C. Zhang, S. Irons, P. Klavins, R. N. Shelton, K. Song, and S. R. Wasserman, *Giant magnetoresistance at 300 K in single crystal of $La_{0.65}(PbCa)_{0.35}MnO_3$*, Appl. Phys. Lett. **66** (1995), no. 23, 3218–3220.

[103] F. K. Lotgering, Philips Res. Rept. **11** (1956), 218.

[104] ———, Philips Res. Rept. **11** (1956), 337.

[105] ———, *Ferromagnetism in spinels: $CuCr_2S_4$ and $CuCr_2Se_4$*, Solid State Communic. **2** (1964), 55–56.

[106] F. K. Lotgering and R. P. van Stapele, *Magnetic and electrical properties of copper containing sulphides and selenides with spinel structure*, Solid State Communic. **5** (1967), 143–146.

[107] F. K. Lotgering, R. P. van Stapele, G. H. A. M. van der Steen, and J. S. van Wieringen, *Magnetic properties, conductivity and ionic ordering in* $Fe_{1-x}Cu_xCr_2S_4$, J. Phys. Chem. Solids **30** (1969), 799–804.

[108] Z. W. Lu, B. M. Klein, E. Z. Kurmaev, V. M. Cherkashenko, V. R. Galakhov, S. N. Shamin, Yu. M. Yarmoshenko, V. A. Trofimova, St. Uhlenbrock, M. Neumann, T. Furubayashi, T. Hagino, and S. Nagata, *Electronic structure of* CuV_2S_4, Phys. Rev. B **53** (1996), no. 15, 9626–9633.

[109] Hans Lueth, *Surfaces and interfaces of solid materials*, Springer, Berlin, 1993.

[110] P. W. Lytle, R. B. Greegor, and I. D. Raistrick, *Determination of structure and valence in vanadium bronze by X–ray absorption spectroscopy*, J. de Physique Colloque **C8** (1986), no. 47, 719–723.

[111] P. Mahadevan, N. Shanthi, and D. D. Sarma, *Estimates of electronic interaction parameters for* $LaMO_3$ *compounds (M=Ti–Ni) from ab initio approaches*, Phys. Rev. B **54** (1996), no. 16, 11199–11206.

[112] ESCA: Technical Manual, 5600 *technique*, Perklin–Elmer, 1991.

[113] J. Matsuno, T. Mizokawa, A. Fujimori, D. A. Zatsepin, V. R. Galakhov, E. Z. Kurmaev, Y. Kato, and S. Nagata, *Photoemission study of the metal–insulator transition in* $CuIr_2S_4$, Phys. Rev. B **55** (1997), no. 24, R15979–15982.

[114] D. N. McIlroy, C. Waldfried, J. Zhang, J. W. Choi, F. Foong, S. H. Liou, and P. A. Dowben, *Comparison of the temperature–dependent electronic structure of the perovskites* $La_{0.65}A_{0.35}MnO_3$ *(A=Ca, Ba)*, Phys. Rev. B **54** (1996), no. 24, 17438–17451.

[115] J. Mendialdua, R. Casanova, and Y. Barbaux, *XPS studies of* V_2O_5, V_6O_{13}, VO_2 *and* V_2O_3, J. Electron Spectrosc. Relat. Phenom. **71** (1994), 249–261.

[116] N. Menyuk, K. Dwight, and A. Wold, *Magnetic properties of* $MnCr_2S_4$, J. Appl. Phys. **36** (1965), no. 3, 1088–1089.

[117] A. J. Millis, P. B. Littlewood, and B. I. Shraiman, *Double exchange alone does not explain the resistivity of* $La_{1-x}Sr_xMnO_3$, Phys. Rev. Lett. **74** (1995), no. 25, 5144–5147.

[118] A. J. Millis, B. I. Shraiman, and R. Müller, *Dynamic Jahn–Teller effect and colossal magnetoresistance in* $La_{1-x}Sr_xMnO_3$, Phys. Rev. Lett. **77** (1996), no. 1, 175–178.

[119] T. Mizokawa, D. I. Khomskii, and G. A. Sawatzky, *Interplay between orbital ordering and lattice distorsions in* $LaMnO_3$, YVO_3 *and* $YTiO_3$, Phys. Rev. B **60** (1999), no. 10, 7309–7313.

[120] J. S. Moodera, L. R. Kinder, T. M. Wong, and R. Meservey, *Large magnetoresistance at room temperature in ferromagnetic thin film tunnel jonctions*, Phys. Rev. Lett. **74** (1995), no. 16, 3273–3276.

[121] Y. Moritomo, A. Asamitsu, H. Kuwahara, and Y. Tokura, *Giant magnetoresistance of manganese oxide with a layered perovskite structure*, Nature **380** (1996), 141–144.

[122] N. F. Mott, Proc. R. Soc. London **A 49** (1949), 416.

[123] _____, *Metal–Insulator Transition*, Taylor and Francis, London, 1974.

[124] Y. Murakami, J. P. Hill, D. Gibbs, M. Blume, I. Koyama, M. Tanaka, H. Kawata, T. Arima, Y. Tokura, K. Hirota, and Y. Endoh, *Resonant X–ray resonant scattering from orbital ordering in* $LaMnO_3$, Phys. Rev. Lett. **81** (1998), no. 3, 582–585.

[125] I. Nacatani, H. Nose, and K. Masumoto, *Magnetic properties of* $CuCr_2Se_4$ *single crystals*, J. Phys. Chem. Solids **39** (1978), 743–749.

[126] M. Nogues, M. Mejai, and L. Goldstein, *Phase relationships and magnetic phase diagram in the system* $Mn_{1-x}Cu_xCr_2S_4$, J. Phys. Chem. Solids **40** (1979), 375–379.

[127] T. Oda, M. Shirai, N. Suzuki, and K. Motizuki, *Electronic band structure of sulphide spinels CuM_2S_4 (M=Co, Rh, Ir)*, J. Phys.: Condens. Matter **7** (1995), 4433–4446.

[128] H. N. Ok, K. S. Baek, H. S. Lee, and C. S. Kim, *Mössbauer study of $Cu_{0.5}Fe_{0.5}Cr_2S_4$*, Phys. Rev. B **41** (1990), no. 1, 62–64.

[129] K. Okada and A. Kotani, *Interatomic and intra–atomic configuration interactions in core–level X–ray photoemission spectra of late transition metal compounds*, J. Phys. Soc. Jpn. **61** (1992), no. 12, 4619–4637.

[130] H. Palmer and C. Greaves, *Structural, magnetic and electronic properties of $Fe_{0.5}Cu_{0.5}Cr_2S_4$*, J. Mater. Chem. **9** (1999), no. 3, 637–640.

[131] J. H. Park, C. T. Chen, S. W. Cheong, W. Bao, G. Meigs, V. Chakarian, and Y. U. Idzerda, *Electronic aspects of the ferromagnetic transition in manganese perovskites*, Phys. Rev. Lett. **76** (1996), no. 22, 4215–4218.

[132] J. H. Park, S. W. Cheong, and C. T. Chen, *Double–exchange ferromagnetism in $La(Mn_{1-x}Co_x)O_3$*, Phys. Rev. B **55** (1997), no. 17, 11072–11075.

[133] J. H. Park, L. H. Tjeng, A. Tanaka, J. W. Allen, C. T. Chen, P. Metcalf, J. M. Honig, F. M. F. de Groot, and G. A. Sawatzky, *Spin and orbital occupation and phase transitions in V_2O_3*, Phys. Rev. B **61** (2000), no. 17, 11506–11509.

[134] M. S. Park, S. K. Kwon, S. J. Youn, and B. I. Min, *Half–metallic structures of giant magnetoresistive spinels: $Fe_{1-x}Cu_xCr_2S_4$ (x= 0.0, 0.5, 1.0)*, Phys. Rev. B **59** (1999), no. 15, 10018–10023.

[135] W. E. Pickett and D. J. Singh, *Electronic structure and half–metallic transport in the $La_{1-x}Ca_xMnO_3$ system*, Phys. Rev. B **53** (1996), no. 3, 1146–1159.

[136] S. Plogmann, T. Schlathölter, J. Braun, M. Neumann, Yu. M. Yarmoshenko, M.V.Yablonskikh, E.I. Shreder, E. Z. Kurmaev, A. Wrona,

and A. Slebarski, *Local moments in Mn–based Heusler alloys and their electronic structures*, Phys. Rev. B **60** (1999), no. 9, 6428–6438.

[137] Stefan Plogmann, *Untersuchung der elektronischen und magnetischen Eigenschaften manganhaltiger Heusler Legierungen mittels Photoelektronen– und Röntgenspektroskopie*, Ph.D. thesis, University of Osnabrück, 1999.

[138] E. W. Plummer and W. Eberhardt, *Angle–resolved photoemission*, Adv. in Chem. Phys. **49** (1982), 533–649.

[139] Z. Popovic and S. Satpathy, *Cooperative Jahn–Teller coupling in the manganites*, Phys. Rev. Lett. **814** (2000), no. 7, 1603–1606.

[140] S. Pouget, M. Alba, N. Fanjat, and M. Nogues, Physica B **180–181** (1992), 244.

[141] A. P. Ramirez, *Colossal magnetoresistance*, J. Phys.: Condens. Matter **9** (1997)), no. 39, 8171–8199 and the references therein.

[142] A. P. Ramirez, R. J. Cava, and J. Krajewski, *Colossal magnetoresistance in Cr–based chalcogenide spinels*, Nature **386** (1997), 156–159.

[143] T. M. Rice, *Spectroscopy of Mott insulators and correlated materials*, edited by A. Fujimori and Y. Tokura, Springer, Berlin, 1995, pag. 221.

[144] F. Rivadulla, M. A. López-Quintela, L. E. Hueso, P. sande, J. Rivas, and R. D. Sánchez, *Effect of Mn–site doping on the transport properties of the colossal amgnetoresistance compound* $La_{2/3}Ca_{1/3}Mn_{1-x}A_xO_3$ *(A=Co,Cr;* $x < 0.1$*)*, Phys. Rev. B **62** (2000), no. 9, 5678–5684.

[145] M. Romand, M. Roubin, and J. P. Deloume, *ESCA studies of some copper and silver selenides*, J. Elect. Spectrosc. Relat. Phenom. **13** (1978), 229–242.

[146] T. Saitoh, A. E. Bocquet, T. Mizokawa, H. Namatame, A. Fujimori, M. Abbate, Y. Takeda, and M. Takano, *Electronic structure of* $La_{1-x}Sr_xMnO_3$

studied by photoemission and X–ray absorbtion spectroscopy, Phys. Rev. B **51** (1995), no. 20, 13942–13951.

[147] T. Saitoh, A. E. Bocquet, T. Mizokawa, H. Namatame, A. Fujimori, Y. Takeda, and M. Takano, *Strontium–doped lanthanum manganese oxides studied by XPS*, Surf. Sci. Spectra **6** (1999), no. 4, 292–301.

[148] T. Saitoh, T. Mizokawa, A. Fujimori, M. Abbate, Y. Takeda, and M. Takano, *Electronic structure and temperature–induced paramagnetism in $LaCoO_3$*, Phys. Rev. B **55** (1997), no. 7, 4257–4266.

[149] T. Saitoh, A. Sekiyama, K. Kobayashi, T. Mizokawa, A. Fujimori, D. D. Sarma, Y. Takeda, and M. Takano, *Electronic spectroscopic investigation of the semiconductor–metal transition in $La_{1-x}Sr_xMnO_3$*, Phys. Rev. B **56** (1997), no. 14, 8836–8840.

[150] D. D. Sarma, N. Shanthi, S. R. Barman, N. Hamada, H. Sawada, and K. Terakura, *Band theory for ground–state properties and excitation spectra of perovskite $LaMO_3$ (M=Mn, Fe, Co, Ni)*, Phys. Rev. Lett. **75** (1995), no. 6, 1126–1129.

[151] D. D. Sarma, N. Shanthi, S. R. Krishnakumar, T. Saitoh, T. Mizokawa, A. Sekiyama, K. Kobayashi, A. Fujimori, E. Weschke, R. Meier, G. Kaindl, Y. Takeda, and M. Takano, *Temperature–dependent photoemission spectral weight in $La_{0.6}Sr_{0.4}MnO_3$*, Phys. Rev. B **53** (1996), no. 11, 6873–6876.

[152] D. D. Sarma, D. Topwal, and A. Chainani, *Electron spectroscopic data of $La_{1-x}Sr_xMnO_3$ and $La_{1-x}Sr_xCoO_3$*, Surf. Sci. Spectra **6** (1999), no. 4, 274–291.

[153] S. Satpathy, Z. S. Popovic, and F. R. Vukajlovic, *Electronic structure of the perovskite oxides: $La_{1-x}Ca_xMnO_3$*, Phys. Rev. Lett. **76** (1996), no. 6, 960–963.

[154] G. A. Sawatzky and D. Post, *X–ray photoelectron and Auger spectroscopy study of some vanadium oxides*, Phys. Rev. B **20** (1979), no. 4, 1546–1555.

[155] Y. Shimakawa, Y. Kubo, and T. Manako, *Giant magnetoresistance in $Tl_2Mn_2O_7$ with the pyrochlore structure*, Nature **379** (1996), 53–55.

[156] S. Shin, M. Fujisawa, H. Ishii, Y. Harada, M. Watanabe, M. M. Grush, T. A. Callcott, R. C. C. Perera, E. Z. Kurmaev, A. Moewes, R. Winarski, S. Stadler, and D. L. Ederer, *Soft X–ray emission spectroscopy of early transition metal compounds*, J. Electron Spectrosc. Relat. Phenom. **92** (1998), 197–205.

[157] S. Shin, S. Suga, M. Taniguchi, M. Fujisawa, H. Kanzaki, A. Fujimori, H. Daimon, Y. Ueda, K. Kosuge, and S. Kachi, *Vacuum–ultraviolet reflectance and photoemission study of the metal–insulator phase transitions in VO_2, V_6O_{13} and V_2O_3*, Phys. Rev. B **41** (1990), no. 8, 4993–5009.

[158] S. Shin, Y. Tezuka, T. Ishii, and Y. Ueda, *Electronic structure of light transition metal compounds studied by photoemission*, Solid State Communic. **87** (1993), no. 11, 1051–1054.

[159] G. Shiranev, D. E. Cox, and S. J. Pickart, *Magnetic structures in $FeCr_2S_4$ and $FeCr_2O_4$*, J. Appl. Phys. **35** (1964), no. 3, 954–955.

[160] D. A. Shirley, *High–resolution X–ray photoemission spectrum of the valence band of gold*, Phys. Rev. B **5** (1972), no. 12, 4709–4714.

[161] ———, *Hyperfine interactions and ESCA data*, Phys. Scripta **11** (1975), 117–120 (and the references therein).

[162] K. Siegbahn, C. Nordling, R. Fahlman, R. Nordberg, K. Hamrin, J. Hedman, G. Johansson, S. E. Karlsson, I. Lindgren, and B. Lindberg, *ESCA, Atomic, Molecular and Solid State Structure Studies by Means of Electron Spectroscopy*, Nova Acta Regiae Soc. Sci., Upsaliensis **20** (1967), no. Ser. IV.

[163] K. E. Smith and V. E. Henrich, *Bulk band dispersion in Ti_2O_3 and V_2O_3*, Phys. Rev. B **38** (1988), no. 9, 5965–5975.

[164] ———, *Photoemission study of composition– and temperature–induced metal–insulator transitions in Cr–doped V_2O_3*, Phys. Rev. B **50** (1994), no. 3, 1382–1390.

[165] V. N. Smolyaninova, X. C. Xie, F. C. Zhang, M. Rajeswari, R. L. Greene, and S. Das Sarma, *Metal–insulator transition in colossal magnetoresistance materials*, Phys. Rev. B **62** (2000), no. 5, 3010–3013.

[166] I. Solovyev, N. Hamada, and K. Terakura, *Crucial role of the lattice distorsion in the magnetism of $LaMnO_3$*, Phys. Rev. Lett. **76** (1996), no. 25, 4825.

[167] W. E. Spicer, *Photoemissive, photoconductive and optical absorbtion studies of alkali–antimony compounds*, Phys. Rev. **112** (1958), no. 1, 114–122.

[168] P. Steiner, V. Kinsinger, I. Sander, B. Siegwart, S. Hűfner, C. Politis, R. Hoppe, and H. P. Műller, *Electronic structure of $(LaSr)_2CuO_4$ and $(NdCe)_2CuO_4$*, Z. Phys. B **67** (1987), 497–502.

[169] B. Grzybowska Swierkosz and J. Haber (Eds.), *Vanadia catalysts for processes of oxidation of aromatic hydrocarbons PWN*, Polish Scientific Publishers, Warsaw, 1984.

[170] Y. Tokura and Y. Tomioka, *Colossal magnetoresistive manganites*, J. Magn. Magn. Mat. **200** (1999), 1–23 (and the references therein).

[171] Y. Tokura, A. Urushibara, Y. Moritomo, T. Arima, A. Asamitsu, G. Kido, and N. Furukawa, *Giant magnetotransport phenomena in filling–controlled Kondo lattice system: $La_{1-x}Sr_xMnO_3$*, J. of Phys. Soc. Jpn **63** (1994), no. 11, 3931–3935.

[172] Y. Tomioka, A. Asamitsu, H. Kuwahara, Y. Moritomo, and Y. Tokura, *Magnetic–field induced metal–insulator phenomena in $Pr_{1-x}Ca_xMnO_3$ with controlled charge–ordering instability*, Phys. Rev. B **53** (1996), no. 4, R1689–1692.

[173] S. Tougaard, *Inelastic background correction and quantitative surface analysis*, J. Elelctron Spectrosc. Relat. Phenom. **52** (1990), 243–271.

[174] S. Tougaard and P. Sigmund, *Influence of elastic and inelastic scattering on energy spectra of electrons emitted from solids*, Phys. Rev. B **25** (1982), no. 7, 4452–4466.

[175] I. O. Troyanchuk, D. D. Khalyavin, E. F. Shapovalova, N. V. Kasper, and S. A. Guretskii, *Magnetic and transport properties of some insulating manganites*, Phys. Rev. B **58** (1998), no. 5, 2422–2425.

[176] I. O. Troyanchuk, L. S. Lobanovsky, D. D. Khalyavin, S. N. Pastushonok, and H. Szymczak, *Magnetic and transport properties of Co–doped manganites with perovskite structure*, J. Magn. Magn. Mat. **210** (2000), 63–72.

[177] N. Tsuda, K. Nasu, A. Yanase, and K. Siratori, *Electronic conduction in oxides*, Springer, New York, 1990.

[178] V. Tsurkan, M. Demeter, B. Schneider, D. Hartmann, and M. Neumann, *Exchange splitting of the Cr, Fe and Mn* $3s$ *XPS spectra in some ternary magnetic semiconductor sulphides*, Solid State Communic. **114** (2000), 149–154.

[179] V. Tsurkan, St. Plogmann, M. Demeter, D. Hartmann, and M. Neumann, *Splitting of the Cr* $2p$ *ions states in some ternary sulphides and selenides*, Eur. Phys. J. B **15** (2000), 401–403.

[180] T. A. Tyson, Q. Qian, C. C. Kao, J. P. Rueff, F. M. F. de Groot, M. Croft, S. W. Cheong, M. Greenblatt, and M. A. Subramanian, *Valence state of Mn in Ca–doped* $LaMnO_3$ *studied by high–resolution Mn* $K\beta$ *emission spectroscopy*, Phys. Rev. B **60** (1999), no. 7, 4665–4674.

[181] St. Uhlenbrock, *Untersuchungen zur Elektronischen Struktur einfacher Übergangsmetall–Oxide–unter besonderer Berücksichtigung des Nickel Oxids*, Ph.D. thesis, University of Osnabrück, 1994.

[182] A. Urushibara, Y. Moritomo, T. Arima, A. Asamitsu, G. Kido, and Y. Tokura, *Insulator–metal transition and giant magnetoresistance in* $La_{1-x}Sr_xMnO_3$, Phys. Rev. B **51** (1995), no. 20, 14103–14109.

[183] G. van der Laan, C. Westra, C. Haas, and G. A. Sawatzky, *Sattelite structure in photoelectron and Auger spectra of copper dihalides*, Phys. Rev. B **23** (1981), no. 9, 4369–4380.

[184] J. H. van Vleck, Phys. Rev. **45** (1934), 405.

[185] N. Y. Vasanthacharya and S. Vasudevan, *High temperature phase transition in* V_3O_5, Indian J. of Pure and Appl. Phys. **18** (1979), 71–73.

[186] R. von Helmolt, J. Wecker, B. Holzapfel, L. Schultz, and K. Samwer, *Giant negative magnetoresistance in perovskite–like* $La_{2/3}Ba_{1/3}MnO_x$ *ferromagnetic films*, Phys. Rev. Lett. **71** (1993), no. 14, 2331–2333.

[187] Carlo Waldfried, D. N. McIlroy, S. H. Liou, R. Sabiryanov, S. S. Jaswal, and P. A. Dowben, *The observation of a surface resonance state in the valence band structure of the perovskite* $La_{0.65}Ba_{0.35}MnO_3$, J. Phys.: Condens. Matter **9** (1997), 1031–1038.

[188] Z. H. Wang, J. W. Cai, B. G. Shen, X. Chen, and W. S. Zhan, *Exchange interaction, spin cluster and transport behaviour in perovskites* $La_{0.67}Sr_{0.33}Mn_{1-x}Ni_xO_3$ *(*$x < 0.2$*)*, J. Phys.: Condens. Matter **12** (2000), no. 5, 601–610.

[189] Ph. Wernet, *Magnetischer dichroismus in der Cr* $2p$*–photoionization*, Ph.D. thesis, University of Hamburg, 2000.

[190] Ph. Wernet, J. Schulz, B. Sonntag, K. Godehusen, P. Zimmermann, M. Martins, C. Bethke, and F. U. Hillebrecht, *Core–valence interactions in the linear dichroism of Cr* $2p$ *photoelectron spectra*, Phys. Rev. B **62** (2000), no. 21, 14331–14335.

[191] Ph. Wernet, B. Sonntag, M. Martins, P. Glatzel, B. Obst, and P. Zimmermann, *Multiplet splitting and valence shell recoupling in the core–level* $2p$

photoelectron spectrum of atomic Mn and Mn compounds, private communication.

[192] O. $\widetilde{S}$ipr, A. $\widetilde{S}$imunek, S. Bocharov, Th. Kirchner, and G. Dräger, *Geometric and electronic structure effects in polarized V K–edge absorption near–edge structure spectra of* V_2O_5, Phys. Rev. B **60** (1999), no. 20, 14115–14127.

[193] K. A. Wilhelmi, K. Waltersson, and L. Kihlborg, *A refinement of the crystal structure of* V_6O_{13}, Acta Chem. Scand. **25** (1971), no. 7, 2675–2675.

[194] A. Winiarski, I. Okonska-Kozlowska, J. Heimann, and M. Neumann, *Investigation of* $Cu_xGa_yCr_zSe_4$ *single crystals*, J. Alloys Comp. **232** (1996), 63–66.

[195] E. O. Wollan and W. C. Koehler, *Neutron diffraction study of the magnetic properties of the series of perovskite type compounds* $La_{1-x}(Ca)_xMnO_3$, Phys. Rev. **100** (1955), no. 2, 545–563.

[196] Z. Yang, Ling Ye, and Xide Xie, *Electronic and magnetic properties of the perovskite oxides:* $LaMn_{1-x}Co_xO_3$, Phys. Rev. B **59** (1999), no. 10, 7051–7057.

[197] Yu. M. Yarmoshenko, M. I. Katsnelson, E. I. Shreder, E. Z. Kurmaev, A. Slebarski, St. Plogmann, T. Schlathölter, J. Braun, and M. Neumann, *Observation of magnetic splitting in XPS MnL–spectra of* Co_2MnSn *and* Pd_2MnSn *Heusler alloys*, Eur. Phys. J. B **2** (1998), 1–3, (and the references therein).

[198] S. J. Youn and B. I. Min, *Effects of doping and magnetic field on the half–metallic electronic structures of* $La_{1-x}Ba_xMnO_3$, Phys. Rev. B **56** (1997), no. 19, 12046–12049.

[199] S. L. Yuan, Y. Jiang, G. Li, J. Q. Li, Y. P. Yang, X. Y. Zeng, P. Tang, and Z. Huang, *Semiconductor–metal transition and magnetoresistance in* $La_{(1+x)/3}Ba_{(2-x)/3}Cu_{1-x}Mn_xO_3$ *(*$0.7 < x < 1$*)*, Phys. Rev. B **61** (2000), no. 5, 3211–3214.

[200] J. Zaanen, G. A. Sawatzky, and J. W. Allen, *Band gaps and electronic structure of transition–metal compounds*, Phys. Rev. Lett. **55** (1985), no. 4, 418–421.

[201] J. Zaanen, C. Westra, and G. A. Sawatzky, *Determination of the electronic structure of transition–metal compounds: 2p X–ray photoemission spectroscopy of nickel dihalides*, Phys. Rev. B **33** (1986), no. 12, 8060–8073.

[202] G. Zampieri, F. Prado, A. Caneiro, J. Briatico, M. T. Causa, M. Tovar, B. Alascio, M. Abbate, and E. Morikawa, *Electronic structure of $CaMnO_x$ with $2.66 < x < 3.00$ studied with photoemission and X–ray absorption spectroscopy*, Phys. Rev. B **58** (1998), no. 7, 3755–3761.

[203] D. A. Zatsepin, V. R. Galakhov, M. A. Korotin, V. V. Fedorenko, E. Z. Kurmaev, St. Bartkowski, and M. Neumann, *Valence states of copper ions and electronic structure of $LiCu_2O_2$*, Phys. Rev. B **57** (1998), no. 8, 4377–4381.

[204] C. Zener, *Interaction between the d–shells in the transition metals. II. Ferromagnetic compounds of manganese with perovskite structure*, Phys. Rev. **82** (1951), no. 3, 403–405.

[205] J. Zhang, D. N. McIlroy, P. A. Dowben, S. H. Liou, R. F. Sabirianov, and S. S. Jaswal, *The valence–band structure of $La_{1-x}Ca_xMnO_3$*, Solid State Communic. **97** (1996), no. 39, 39–44.

[206] Lei Zheng, X. Xu, Li Pi, and Y. Zhang, *Observation of electronic phase separation in $La_{0.825}Sr_{0.175}Mn_{1-x}Cu_xO_3$*, Phys. Rev. B **62** (2000), no. 2, 1193–1196.

[207] T. M. Zimkina and V. A. Fomichev, *Ultra–soft X–ray spectroscopy*, Leningrad University, 1971.

[208] R. Zimmermann, *Experimentelle Untersuchungen zur elektronischen Struktur von 3d–Übergangmetalloxiden, ihre Beschreibung im Rahmen des Clustermodells und Vergleich mit Bandstrukturrechnungen*, Ph.D. thesis, Saabruecken University, 1996.

[209] R. Zimmermann, R. Claessen, F. Reinert, P. Steiner, and S. Hüfner, *Strong hybridization in vanadium oxides: evidence from photoemission and absorbtion spectroscopy*, J. Phys.: Condens. Matter **10** (1998), 5697–5716 (and the references therein).

[210] R. Zimmermann, P. Steiner, R. Claessen, F. Reinert, S. Hüfner, P. Blaha, and P. Dufek, *Electronic repulsion of 3d transition metal oxides: on–site Coulomb repulsion versus covalency*, J. Phys.: Condens. Matter **11** (1999), 1657–1682.

Curriculum Vitae

I was borned in Aiud, Romania on July 1, 1972. At the end of my studies at the Faculty of Physics (1990 – 1995), Babes–Bolyai University of Cluj–Napoca, Romania, I obtained the Licence Diplom. Since November 1997 I have worked in the group Photoelectron Spectroscopy of apl. Prof. M. Neumann.

List of publications

- M. Demeter, St. Bartkowski, E. Z. Kurmaev, M. Neumann, V. L. Volkov, V. M. Cherkashenko and G. C. Zakharova, *Investigation of the mixed-valent system* $V_{2-x}Mo_xO_5$ *by XPS*, SPIE **3724**, 296 – 300 (1999)

- M. Coldea, M. Neumann, D. Todoran, M. Demeter, R. Tetean, V. Pop, *X-ray Photoelectron Spectroscopy and Magnetism of* $GdNi_{5-x}Al_x$, Studia Univ. Babes–Bolyai, Ser. Physika XLIV **2**, 35 (1999)

- M. Demeter, M. Neumann and W. Reichelt, *Mixed-valence vanadium oxides studied by XPS*, Surf. Sci. **454-456**, 41, (2000)

- V. Tsurkan, D. Samusi, E. Burzo, V. Pop, M. Neumann, M. Demeter, M. Baran, R. Szymczak and H. Szymczak, *Magnetic properties of* $FeCr_2S_4$*: Cu, In semiconductors*–Interface Controlled Materials **12**, 5897 – 5904, 2000

- V. Tsurkan, M. Demeter, B. Schneider, D. Hartmann and M. Neumann, *Exchange splitting of the Cr, Fe and Mn* $3s$ *XPS spectra in some ternary magnetic semiconductor sulphides*, Solid St. Commun. **114**, 149, (2000)

- V. Tsurkan, St. Plogmann, M. Demeter, D. Hartmann and M. Neumann, *Splitting of the Cr* $2p$ *ions states in some ternary sulphides and selenides*, Eur. Phys. J. B **15**, 401, (2000)

- E. Z. Kurmaev, A. V. Postnikov, H. M. Palmer, C. Greaves, St. Bartkowski, V. Tsurkan, M. Demeter, D. Hartmann, M. Neumann, D. A Zatsepin, V. R. Galakhov, S. N. Shamin and V. Trofimova, *Electronic structure of* $FeCr_2S_4$ *and* $Fe_{0.5}Cu_{0.5}Cr_2S_4$, J. Phys.: Condens. Matter **12**, 5411, (2000)

- V. R. Galakhov, L. D. Finkelstein, D. A. Zatsepin, E. Z. Kurmaev, S. V. Naumov, A. A. Samokhvalov, G. K. Tatarinova, M. Demeter, St. Bartkowski, M. Neumann and A. Moewes, *Cu* $3d$ *impurity states in* $Mg_{1-x}Cu_xO$*–solid solutions: X–ray photoelectron and X–ray emission study*, Phys. Rev. B **62**, 4922 – 4926 (2000)

- M. Demeter, V. Cherkashenko, A. V. Postnikov, V. R. Galakhov, E. Z. Kurmaev and M. Neumann, *Electronic structure of the mixed–valence system* $V_{2-x}Mo_xO_5$, accepted for publication in Surf. Sci.

- V. Tsurkan, M. Demeter, St. Plogmann and M. Neumann, *X–Ray Photoelectron Spectroscopic Studies of Some Ternary Magnetic Chalcogenide Semiconductors*, accepted for publication in Jpn. J. of Appl. Phys.

- M. Demeter, V. Galakhov, N. I. Labachevskaya, E. Z. Kurmaev and M. Neumann, *Electronic study of the La–Mn–O system by XPS and XES*, Acta Polonica A, **98**, no.5, 587 – 591, 2000

- S. G. Chiuzbăian, M. Coldea, M. Neumann, D. Todoran, M. Demeter, R. Tetean and V. Pop, *Magnetic and electronic properties of* $GdNi_{5-x}Al_x$ *intermetallic compounds*, , Acta Polonica A, **98**, no.5, 629 – 632, 2000

- M. Coldea, M. Neumann, M. Demeter, V. Pop, *Mixed-valence state of Ce ions in* $CeNi_2Al_3$, J. of Alloys and Compounds (in press)

- M. Coldea, M. Neumann, M. Demeter, T. Farcas, S. Chiuzbăian, *XPS studies on powdered* $CeNi_5$ *oxidized in air*, accepted for publication in Materials Letters

- V. R. Galakhov, M. Demeter, St. Bartkowski, M. Neumann, N. A. Ovechkina, E. Z. Kurmaev, N. I. Lobachevskaya, Ya. M. Mukowskii and D. L. Ederer, *Mn* $3s$ *exchange splitting in mixed–valence manganites*, to be submitted

- E. Z. Kurmaev, I. I. Lyakhovskaya, J. Kortus, N. Miyata, M. Demeter, M. Neumann, M. Yanagihara, M. Watanabe, T. Muranaka, J. Akimitsu, *Electronic structure of* MgB_2*: X-ray emission and absorption spectra*, submitted to Phys. Rev. Lett.